CsI calorimeter for the J-PARC KOTO experiment

A DISSERTATION PRESENTED IN PARTIAL FULFILLMENT OF THE REQUIREMENTS
FOR THE DEGREE OF DOCTOR OF SCIENCE

Department of Physics, Graduate School of Science
Osaka University

by

Eito IWAI

April, 2012

Abstract

The KOTO experiment was designed and is being prepared at J-PARC (Japan Proton Accelerator Research Complex), to observe the rare decay of long lived neutral kaons, $K_L \to \pi^0 \nu \bar{\nu}$, with the sensitivity of the Standard Model prediction. An electromagnetic calorimeter for the KOTO experiment was upgraded to have a finer granularity and waveform readout capability. We measured the performance of the calorimeter, and reproduced the obtained performance based on the first principle. We also developed a new analysis method to discriminate incident angles by using shower shape information obtained with the finer granularity. By applying the new method, one of the backgrounds, the $K_L \to \gamma\gamma$ decay in the beam halo, was estimated to be suppressed by a factor of 50, and the total number of background events was estimated to be reduced to less than the number of signal events predicted by the Standard Model.

Acknowledgment

This thesis could not be achieved without enormous support from many people. I would like to express my appreciation to them on this occasion.

First and foremost, I would like to express my deepest gratitude to my supervisor, Prof. Taku Yamanaka, for giving me a great opportunity for the research in high energy physics. He always showed me how to think critically about unknown things and how to disentangle their intricate knots. His strict attitude in research and his inexhaustible ideas often impressed me deeply. I cannot express all of my warmest appreciation enough for giving me a lot of support and advice.

I would like to extend my gratitude to all of the KOTO collaborators. I am deeply thankful to M. Tecchio, M. Bogdan and D. McFarland. I have worked on the DAQ system for the KOTO experiment. We discussed many DAQ things and worked together to develop the DAQ system. My gratitude goes to N. Sasao, J. Comfort, T. Inagaki, S. Suzuki, M. Campbell, Y.W. Wah, T. Komatsubara, G.Y. Lim, T. Nomura, Y. Tajima, H. Nanjo and H. Watanabe, for giving me invaluable support and advice on analysis. In particular, Y.W. Wah and M. Cambell kindly took care of me during my stay in US. I am also thankful to M. Togawa and Y. Ri. They are a few years senior to me, and gave me a lot of helpful advice as good elder brothers not only about physics but also human life. I owe great thanks to T. Shimogawa, R. Ogata and Y.C. Tung for their kindness and friendship. Because we are the elder students in the KOTO group, we often chatted frankly, and reported our circumstances and status to each other. My thanks go to K. Sato, K. Shiomi and J.W. Lee for their kindness and friendship. I really enjoyed discussing physics and analysis with them. I would like to express my appreciation to T. Masuda, Y. Sugiyama, Y. Nakaya and Y. Yanagida for their great contributions to the beam test.

I am also grateful to T. Ishikawa and H. Yamazaki, who are the manager of the Research Center for Electron Photons, for their support. They helped us kindly during the beam test even early in the morning and late at night.

I would like to thank all of the members of the Yamanaka-Taku group at Osaka University. I owe special thanks to M. Hirose and W. Okamura for their kindness and friendship. I really enjoyed chat with them about their studies, hobbies and Mac/Apple. I am also deeply thankful to the secretaries of the group, A. Kamei and M. Kawaguchi, for their help.

My special thanks go to M. Yamaga, T. Hara, K. Sakashita, T. Sumida and H. Miyake, who taught me from basic knowledge to technical things while in my master's degree. Most of what I can do now in high energy physics is undoubtedly based on the acquirements given by them.

Finally, I would like to thank my parents, Kaoru and Naomi Iwai, and my dear girlfriend, Rie. Thanks to their continual support and encouragement, I can concentrate on my own studies in peace.

Eito Iwai
Osaka, Japan.
April 2012

Contents

1 Introduction 1

1.1 $K_L \to \pi^0 \nu \bar{\nu}$ decay . . . 1

1.2 KOTO experiment at J-PARC . . . 3

1.2.1 Experimental method . . . 3

1.2.2 Background sources . . . 5

1.3 Detector upgrades . . . 5

1.3.1 Upgrade of electromagnetic calorimeter . . . 5

1.3.2 Upgrade of readout system . . . 6

1.4 Purpose and outline of this thesis . . . 7

2 Apparatus of the KOTO experiment 8

2.1 Beam line . . . 8

2.2 KOTO detector . . . 8

2.2.1 Electromagnetic calorimeter . . . 11

2.2.2 Data acquisition system and readout . . . 12

2.2.3 Other veto counters . . . 13

3 Performance evaluation of the CsI calorimeter 18

3.1 Experiment . . . 18

3.1.1 e^+ beam . . . 18

3.1.2 Scintillating fiber position detector . . . 19

3.1.3 CsI calorimeter . . . 21

3.1.4 Data acquisition system . . . 21

3.1.5 Run . . . 24

3.2 Pulse shape analysis . . . 25

3.2.1 Error on each point . . . 25

3.2.2 Fitting . . . 26

3.3 Energy calibration . . . 29

3.3.1 Gain correction . . . 29

3.3.2 Calibration with cosmic rays . . . 33

3.3.3 Non-linearity . . . 33

3.4 Calibration with e^+ beam . . . 35

3.4.1 χ^2 based calibration method . . . 35

3.4.2 Method to estimate the precision of the calibration constants . . . 36

3.4.3 Extension for treating non-linearity . . . 39

3.4.4 Confirmation with data . . . 40

3.5 Energy resolution . . . 46

3.6 Timing resolution . . . 48
3.7 Summary of this chapter . . . 51

4 Performance of the waveform readout 53
4.1 Outline of this chapter . . . 53
4.2 Measurement . . . 53
4.2.1 Timing resolution . . . 54
4.2.2 Typical waveform . . . 56
4.2.3 Timing PDF . . . 56
4.3 Performance estimation . . . 60
4.3.1 Pulse shape simulation procedure . . . 60
4.3.2 Data comparison . . . 61
4.4 Parameters for CsI crystals . . . 61
4.4.1 Properties of single photoelectrons . . . 62
4.4.2 Absolute light yield . . . 64
4.5 Comparison and Evaluation . . . 64
4.6 Summary of this chapter . . . 67

5 New analysis method for the upgraded calorimeter 68
5.1 Incident position reconstruction . . . 68
5.2 Incident angle discrimination . . . 70
5.3 Incident direction discrimination . . . 75
5.4 Double pulse separation . . . 80
5.5 Summary of this chapter . . . 82

6 Sensitivity of the KOTO experiment 83
6.1 Background sources . . . 83
6.2 Possible backgrounds eliminated by incident angle discrimination . . . 83
6.2.1 $K_L \to \gamma\gamma$ backgrounds . . . 83
6.2.2 $\eta \to \gamma\gamma$ at CV backgrounds . . . 87
6.3 Other backgrounds . . . 88
6.4 Accidental loss . . . 91
6.5 Expected sensitivity . . . 91

7 Discussion 93
7.1 Further improvement of the timing resolution . . . 93
7.2 Further improvement on the sensitivity . . . 94
7.3 Uncertainty on evaluating the number of $K_L \to \gamma\gamma$ background events . . . 95
7.3.1 Uncertainty of the shower shape PDF . . . 95
7.3.2 Uncertainty of the rate of halo K_Ls . . . 97

8 Conclusion 100

A Functions for pulse shape fitting 101

List of Figures

1.1 A Feynman diagram of the $K_L \to \pi^0 \nu \bar{\nu}$ decay. 2

1.2 A conceptual view of the KOTO experiment. 4

1.3 A schematic view of the π^0 reconstruction. 4

1.4 Schematic views of backgrounds caused by beam halo particles: a) $\eta(\to \gamma\gamma)$ or π^0 produced by the interaction between detector materials and halo neutrons, b) $K_L \to \gamma\gamma$ decay of the halo kaon. 5

1.5 Schematic views of the improvement of the granularity of the calorimeter. The figures show the activities with 7 cm (left) and 2.5 cm (right) square crystals for the same events, in which 300 MeV photons hit the calorimeter with the 20° polar angle and 45° azimuthal angles. The squares in each figure correspond to crystals, and the color shows the deposit energy in each crystal in MeV. 6

1.6 A conceptual view of our waveform readout with a Bessel filter. Figure on the left shows a signal from CsI crystal recorded by an oscilloscope. The black dots show an example of a 125 MHz sampling. Figure on the right shows a recorded pulse shape by FADC with the filter. 7

2.1 A schematic view of the neutral beam line. A common target in the proton beam line and the neutral beam line set on a same axis, and the neutral beam line is located 16° from the primary proton beam line in a horizontal plane. The beam line consists of a pair of collimators, a sweeping magnet, and a γ absorber, and it is 21 m long. The KOTO detector is placed just downstream of the second collimator. 9

2.2 The estimated neutron profiles in horizontal(left) and vertical(right) axes[12]. The red histogram shows the result with the final design, black histogram shows the result before the final optimization. 9

2.3 The K_L momentum spectra at the exit of the beamline, 21 m downstream from the target[13]. Dots show the data, and histograms show the simulation results obtained with FLUKA(solid line), GEANT3(dots) and GEANT4(dashed line). . 10

2.4 A side view of the KOTO detector. The decay volume at the middle of the detector is surrounded by hermetic particle detectors. There is a calorimeter at the downstream of the decay volume. The other detectors are used for vetoing extra particles. 10

2.5 A front view of the CsI calorimeter for the KOTO experiment. It consists of 2240 "small" crystals and 476 "large" crystals. The calorimeter is 50 cm long in depth. 11

2.6 An overview of the DAQ system for the KOTO experiment. Signals from all the detectors are read out by Flash ADC boards. A MACTRIS board generates triggers based on the digitized signals from FADCs with L1 trigger boards. The corresponding data for a trigger is sent to an event building system through L2 trigger boards after some event selections. 12
2.7 A photograph of the FADC board (right) and the circuit diagram of the Bessel filter (left). The FADC board was developed at the University of Chicago. It has 16 analog input channels. Input signal is passed to the Bessel filter, and the output from the filter is recored by 125 MHz FADC. 13
2.8 A schematic view of detectors in the upstream section. The FB and CC02 are placed upstream of the decay volume. 14
2.9 A schematic view of CC02. The CC02 is segmented into multiple crystals along both the longitudinal and perpendicular directions, to measure the flux and energy spectrum of halo neutrons. 14
2.10 A schematic view of detectors in the middle section. The MB surrounds the side of the decay volume. 15
2.11 A schematic view of CV. It consists of two layers. The CV is placed in front of the CsI calorimeter. 16
2.12 A schematic view of detectors in the downstream section. The CsI calorimeter is placed downstream of the decay volume. The CC03 and LCV are placed along the beam hole of the calorimeter. The OEV surrounds the calorimeter to fill gaps between the calorimeter and the support structure. 16
2.13 A schematic view of BHPV module. The module consists of a lead plate, a stack of aerogel tiles, a mirror, a Winston cone, and a PMT. 17

3.1 A photograph of the beam test apparatus. The beam test apparatus consisted of a e^+ beam, a scintillating fiber position detector and a CsI array. The CsI array was mounted on a turntable on the X-stage. The X-stage was placed in a dry room. 19
3.2 A schematic top view of the e^+ beam line[14]. The beam line consists of a 20 μm thick Au foil as a target, a pair of Pb collimators, and a dipole magnet labeled $\mathcal{R}$TAGX in this figure. The strength of the magnetic field of the dipole magnet was 1.2 T at a maximum. The e^+ beam size was defined by the hole with the diameter of 20 mm in the second collimator. Photographs are the Au foil and the first Pb collimator, the dipole magnet, and the second Pb collimator. 20
3.3 A photograph of the scintillating fiber position detector and the CsI array. The position detector was placed just in front of the CsI crystals (black elements with white labels). It consisted of two layers for x&y views, and each layer consisted of 48 scintillating fibers. 20
3.4 The CsI calorimeter used for the beam test and the dark box on the turntable. The cover of the dark box is not shown in this figure. 22
3.5 Temperature(top) and humidity(bottom) in the dry room and the dark box. The dots in the top figure show the temperature at the upstream(black) and downstream(red) surface of the CsI array, around the PMTs/CW-bases(blue) and in the dry room(magenta). The black dots in the bottom figure show the relative humidity in the dry room. 22

3.6 A schematic view of the LED flasher system to monitor the gain of each PMT. The LED output was monitored with a PIN photodiode. The light from the LED was distributed to each crystal through a quartz fiber. 23

3.7 The location of the trigger counters for cosmic rays. Figure on the left(right) shows the side(front) view of the setup. 23

3.8 An overview of the DAQ system for the beam test. 24

3.9 Correlation between the fitted pulse height and the reduced χ^2 of the fitting. Pulse shapes were fitted with the Asymmetric Gaussian shown in Equation 3.1. An error on each sampling point was set at the amount of the ground noise. The red line shows a fitting function of the correlation just for a study. 25

3.10 The pulse shapes of one channel for different pulse height ranges. The pulse heights are normalized to 1. The pulse shape in the tail region varies with the pulse height. 26

3.11 The pulse shapes of different channels for one pulse height range. Pulse shapes are different between channels at their tail parts, in particular. A few channels have totally different tail shapes. 27

3.12 The distribution of the timing difference between two selected crystals for around 5 MeV(left) and 100 MeV(right). When fitting the pulse shapes, the fitting parameters except pulse height and timing were fixed for the black histogram, and floated for the red histogram. 27

3.13 The correlation between the fitted pulse height and the reduced χ^2 of the template based fitting. The dashed brown lines show the boundaries of the pulse height ranges for the templates. 28

3.14 The relative output of the PIN photodiode for the LED light pulses used for PMT gain monitoring. The LED output was monitored by the PIN photodiode to be used at the KOTO experiment. We started our main data taking at 4/13 11:00 AM, and the LED output was stable within 0.5% after then. 29

3.15 The relative ratio of the PMT output to the PIN photodiode output for the LED light pulses. 30

3.16 The pulse height distributions of cosmic ray events taken in two separate days with(right) and without(left) the PMT gain correction. The gain of this PMT was unstable according to the LED gain monitoring system. 30

3.17 Typical gain histories of PMTs in the middle(top) and near outside(bottom) of the array monitored with the LED. The black dots show the relative ratios of the outputs of the PMTs to the PIN photodiode for the LED light pulses for each period, and the red dots show the averaged values over stable periods to be used for the gain correction. The outputs of most of the PMTs were stable within a few % during the data taking. 31

3.18 The widths of the energy distributions of all the beam data for each day. The black(red) dots correspond to the widths without(with) the gain correction. Energies were calibrated with cosmic ray events taken on the last day, 4/17. Assuming the gain drifts along the time, the gain correction should be more effective for the earlier dates. Most of the widths became narrower with the PMT gain correction. 32

3.19 The differences of the most probable values of the pulse height distributions of cosmic ray events in separate two days normalized by the statistical error for each channel. The black(red) histogram shows the distribution without(with) the PMT gain correction. Although it is still within the statistical errors, the gain correction moved both the mean and width of the distribution closer to the ideal values, 0 and 1, respectively. . . . 32
3.20 Correlation between the maximum pulse height in all the crystals and the total energy for events in the (800 MeV 0°) data. Black dots represent the mean total energies for different pulse height ranges. . . . 33
3.21 The maximum pulse height dependence of the total energy for various beam energies. The vertical scale of the smallest height range for 300 MeV data was adjusted to 1, and the vertical scale for the larger beam energy was adjusted to the smaller beam energy. . . . 33
3.22 The setup to measure the non-linearity with a function generator (bottom). There are three amplifiers on the passage of signals before digitization. . . . 34
3.23 Correlation between the observed pulse height and the relative output. The relative output was the ratio of the observed charge to the height of the function generator output. A non-linearity is also observed. . . . 34
3.24 Performance check of the χ^2 based calibration method. We varied the deposit energies in each channel with a fixed ratio within ±8 %, and corrected those energies to minimize the χ^2 in Equation 3.3. The black histogram shows Monte-Carlo true distribution of the reconstructed total energy, the red histogram shows the distribution with varied energies, and the blue histogram shows the distribution with energies calibrated by the method. . . . 36
3.25 Correlation between the estimated precision by Equation 3.10 and the difference between calculated and true energy scales. . . . 38
3.26 An example of applying selection of the correction factors based on the estimated precision by Equation 3.10 on calibration. The vertical(horizontal) axes show the geometrical ID of crystals in $x(y)$, and z-axes show the difference between calculated and true energy scales. Figure on the left(right) shows the obtained result without(with) selection of the correction factors. We applied the correction factors based on the beam data for the crystals whose estimated precision is less than 2 %. . . . 38
3.27 Examples of correction factor for each pulse height range obtained with the extended method. The black dots shows calculated correction factors for different pulse height ranges, and the blue line shows the true pulse height dependence. Figure on the left(right) shows the case which the constants are independent(dependent) of the pulse height. The obtained values for larger pulse height ranges tend to be slightly larger than the true values. . . . 40
3.28 Correlation between a deposit energy in each crystal and the total deposit energy of the event. The black dots show the mean total energy for deposit energies in crystals. Total energy has some dependence when a crystal contains most of the beam energy. . . . 41
3.29 Correlation between a deposit energy in each crystal and the total deposit energy of the event for a) 600MeV and b) 460MeV data. c) Those dependences are similar if we normalize the deposit energy of each crystal by the beam energy. . . . 41

3.30 Obtained correction factor versus pulse height range, with(right) and without(left) the "smearing correction". The black dots show correction factors for different pulse height ranges and the blue line shows the true pulse height dependence. Figures on the top(bottom) show the case which the constants are independent(dependent) of the pulse height. The smearing correction works in large pulse height ranges. 42

3.31 The difference between the calculated correction factors and Monte-Carlo true values for various pulse height ranges. The black(red) line shows the difference without(with) the smearing correction for a) all the pulse height ranges, and b) large pulse height ranges (> 6000). 42

3.32 The distributions of total energy deposit for (460 MeV, 30°) e^+s. The black histogram was made with constants obtained with cosmic rays, and the red histogram was made with constants obtained with the χ^2-based method. 43

3.33 The distributions of total energy deposit for (800 MeV, 0°) e^+s. The black histogram was made with constants obtained with cosmic rays, and the red(blue) histogram was made with constants obtained with the χ^2-based method without(with) the smearing correction. 43

3.34 The energy distribution for (800 MeV, 0°) e^+s. Correction factors only for the pulse heights $< 7000 - 8000$ were determined by the calibration with beam data, and correction factors for the pulse heights $> 7000 - 8000$ were extrapolated by the function (Equation 3.13). To check the validity of the extrapolation by the function, the events in this plot were required to have the maximum pulse height larger than 6500 counts. The black histogram was made with constants obtained with cosmic rays, the red histogram was made with constants obtained with the χ^2-based method with the smearing correction, and the blue histogram was made with constants obtained with the inter-/extra-polation function made from the constants for the smaller pulse height ranges. 44

3.35 The hit position dependences of the mean total energy for (600 MeV, 0 °) data with(right) and without(left) the correction for the non-linearity. 45

3.36 The temperature dependence of the total energy for (800 MeV, 40°) data. The fitted slope was -7.1 ± 0.6 MeV/°C, and it corresponds to -0.93 ± 0.08 %/°C. . . 45

3.37 The ratio of the pulse height to the sum of heights is shown as a function of the pulse height. 47

3.38 The distributions of deposit energy based on the pulse height(blue) and the sum of heights(red) for (460 MeV, 30°) data. The black line shows the distribution obtained with the constants by cosmic rays and the sum of heights based calculation just for the comparison. 47

3.39 The obtained energy resolutions for various energies and incident angles. Incident position was not limited for the figure on the left, and limited by the scintillating fibers for the figure on the right. The black dashed lines are obtained with the calibration with cosmic rays, the red dashed lines are the function at KTeV experiment[16] (though they only used more than 3 GeV photons), the blue dashed lines show the designed value of the KOTO experiment. 48

3.40 The obtained energy resolutions were parameterized with Equation 3.18. The black dots and line show the obtained energy resolutions and the fitting function for the incident angle of 0°, respectively. The data point for (800 MeV, 0°), shown as a black circle, was excluded from the fitting to suppress the effect of the non-linearity. The red dots and line are for the incident angle of 30°, which suffered less from the non-linearity, for comparison. The χ^2 and the fitting parameters in this figure are for the 0° data. 49

3.41 The timing resolution was calculated for each incident position region relative to the evaluating crystal, to avoid the time spread by shower development. 0) hit on the crystal, n) distance from the crystal $< 8n$ mm ($n \geq 1$). 50

3.42 The obtained timing resolutions as a function of deposit energy in a crystal. The color of the dots indicate the hit position regions shown in Fig. 3.41. 50

3.43 The distance from the perpendicular bisector of the neighboring two crystals to the incident position was required to be less than 2 mm, to suppress the time spread caused by shower development. 51

3.44 The obtained timing resolutions as a function of deposit energy in a crystal. The black dots show the results obtained with using the external scintillator, and the red dots show the results obtained with the neighboring two crystals. The position dependent values of the former result were combined into one for each energy range. 52

3.45 The obtained timing resolutions were parameterized with Equation 3.20(red line) and 3.21(blue line). The black dots show the result of data combined with using the external scintillator and the neighboring crystal method, as a function of the deposit energy. 52

4.1 A setup used to measure the timing resolution for different numbers of photo-electrons. S1 and S2 were plastic scintillators to trigger cosmic rays. S3 was a lead/scintillator sandwich counter of interest. A variable neutral density filter was placed between S3 and a PMT for S3 to reduce the number of photons from S3. 54

4.2 The PMT gain was measured by counting the number of photoelectrons. Figure on the left shows the ADC distribution of the well-reduced LED signal with the applied voltage of 2000 V to the PMT. By calculating the charge of a single photoelectron, we can determine the PMT gain. Figure on the right shows the measured gain for different applied voltages. The measured typical gain was 1.6×10^7 at 2000 V. 55

4.3 The distributions of timing differences: $t_2 - t_1$(left) and $t_3 - \frac{1}{2}(t_1 + t_2)$(right). On the right plots, the distance between the 2 peaks is 8 ns. This was caused by 1 clock time shift between the three channels, S3 and S1/S2, in the 125MHz FADC. 55

4.4 The measured timing resolution of a plastic scintillator as a function of the number of photoelectrons. This result will be compared to the values obtained by the new method to generate pulses described in the coming subsection. 56

4.5 The S3 ADC distribution of the ”single photoelectron dominant samples”. The red dots show the TDC overflow data in which no photoelectrons were observed, and the black histogram shows whole data. The zero photoelectron data was recorded once every 100 events. The single photoelectrons clearly show up in region (2). 57

4.6 A waveform of the single photoelectron recorded with the 125 MHz FADC. The typical waveform of single photoelectron was parameterized with lower order Asymmetric Gaussian (Equation 3.17). The red line shows the fitted function. . . 57

4.7 The distribution of a(left) and σ_0(right) in Equation 3.17 for single photoelectron pulses through the Bessel filter. 57

4.8 Figure on the left(right) shows the ADC(TDC) distribution of the data with a higher rate. Left) The black histogram shows all the recorded events and the red dots show events with no photoelectrons observed (TDC overflow). The zero photoelectron data was pre-scaled to 1/10 during data taking. Events between the blue broken lines were used as single photoelectron samples. Right) The timing distribution was also parameterized with lower order Asymmetric Gaussian (Equation 3.17). The red line shows the fitted function. The events later than 150 ns were outside of the ADC gate. 58

4.9 An example of deformation by timing resolution. Blue line shows the input PDF, black histogram shows the PDF smeared by a 2 ns timing resolution, red line shows the fitting result of the histogram. The fitted function was slightly wider than the input PDF. 59

4.10 The parameter shifts by timing resolution estimated by a toy Monte-Carlo simulation for typical width, σ_0(left), and asymmetry parameter, a(right). Horizontal axes show the smearing resolution and vertical axes show the fitted parameters. Blue arrows show the MC input parameters, red lines show the measured parameters. 59

4.11 The simulation procedure of the pulse shape generation. 60

4.12 A waveform generated by the simulation procedure described in the text. 60

4.13 The energy distribution for data and Monte-Carlo. The black histogram shows data, and the blue histogram shows Monte-Carlo. The distribution of Monte-Carlo was horizontally scaled to adjust the peak position to data, and the red line is a fitted function used to adjust the horizontal scale. 61

4.14 The measured timing resolution (black dots) and the estimated timing resolution (red dots) of the plastic scintillator for various numbers of photoelectrons. 62

4.15 A waveform of a single photoelectron. The typical waveform of single photoelectron was also parameterized with Asymmetric Gaussian with a lower order (Equation 3.17). The red line shows the fitted function. 62

4.16 The distribution of a(left) and σ_0(right) in Equation 3.17 for single photoelectron pulses after the Bessel filter tuned for the CsI crystals. 63

4.17 The timing distribution of single photoelectrons from a CsI crystal. The timing distribution was parameterized with Asymmetric Gaussian with a higher order (Equation 3.1). The red line shows the fitted function. 63

4.18 The observed charge distribution of a CsI crystal obtained with cosmic rays with(left) and without(right) the variable neutral density filter. The filter was set to generate single photoelectron dominant samples and measure the charge of single photoelectron pulses. 64

4.19 The correlation between the relative light yields and the measured absolute light yields of CsI crystals. 65

4.20 The timing resolution as a function of the deposit energy in a CsI crystal. The black solid line with dots shows the estimated timing resolution, the black dashed lines show the ones with 10 % smaller/larger light yield corresponding to the error of the measured relative light yields. The red dots show the result of data combined with using the external scintillator and the neighboring crystal method in Fig. 3.45. 65

4.21 The distributions of the shape parameters in Equation 3.17, σ_0(left) and a(right), for all the crystals. The red dashed lines show the value observed with the generated pulses. 66

4.22 The total energy distributions of data and Monte-Carlo with the generated pulse shapes. The integrals of both histograms were normalized to 1. 66

4.23 The distributions of the ratio of σ to the most probable value of the deposit energy distribution with cosmic ray events for Monte-Carlo(top) and data(bottom). The red(black) lines show the distribution obtained with the Monte-Carlo with(without) generated pulses, and the blue lines show the distribution obtained with data. The difference of widths between data and Monte-Carlo is caused by the difference of statistics between them. 67

5.1 The correlation between the incident position and the reconstructed position obtained with the energy-weighted mean (Equation 5.1), obtained with Monte-Carlo simulation. Each black dot shows the mean value of the reconstructed position for each incident position range. The blue line shows the case where the both positions match. The figure was obtained with 25 mm square crystals. 69

5.2 The correlation between the fractions of energy deposit in 0.25 mm-wide slices and their distances from the incident positions. The black line shows the mean energy fraction. 70

5.3 The mean fraction of energy in a 25 mm-wide band is shown as a function of the distance between the center of the band and the incident position. The black, red and blue lines show the fraction for the incident angle of 10°, 20°, and 30°, respectively. 70

5.4 A schematic view of the dynamical generation of templates as a function of the distance between the center of the band and the incident position. The black line shows the mean energy fraction in a 25 mm-wide band as a function of the distance. A 25mm-wide bar shows the mean energy fraction of the column/row at each position. The green bar is the row of interest. Figure on the left shows a template generated for the case where the distance from the center of the row to the incident position was 25 mm. Figure on the right shows another template generated for the distance of 12.5 mm. 71

5.5 An example of shower shape fitting. The bin width corresponds to the width of a crystal. The black histogram shows the energy fraction of a single photon in each row. The red line shows the fitted template. 71

5.6 The comparison of the position resolution between the energy-weighted mean method (black) and the new fitting-based method (red) for e^+s with Monte-Carlo simulation. The RMS value of the distribution of distance between the reconstructed position and Monte-Carlo true value, was used as a position resolution in this plot. 72

5.7 The distribution of the distance between the reconstructed position, and the hit position measured with scintillating fibers. The black dots show data and the red histogram shows Monte-Carlo simulation. 72
5.8 The position resolutions for various incident angles. The black (red) dots show data (Monte-Carlo). The distribution of the distance between the reconstructed position and the hit position measured with scintillating fibers was fitted with Asymmetric Gaussian (Equation 3.17), and its σ_0 was used as the position resolution. 72
5.9 Examples of PDFs of energy fraction for 650 MeV photons at (a) 0 mm, and (b) 50 mm from the energy-weighted mean position. The black/red/blue lines show the PDFs for the incident angles of 0°/20°/40°, respectively. 73
5.10 (a) The likelihood ratio distribution for Monte-Carlo samples of photons with the incident angle of 10°(black) and 30°(red). (b) The ratio of the survival probabilities between 10° to 30° samples that events pass a cut on the Likelihood ratio, as a function of the survival probability of the 10° samples. 74
5.11 The likelihood ratio distributions for the incident angle of 0° samples. The likelihoods for the assumptions of 0° and 20° incident angles were compared. The black dots show data and the red histogram shows Monte-Carlo with materials along the beam line including a collimator and air. The red dashed histogram shows the distribution obtained with Monte-Carlo without materials in the beam line. The likelihood ratio distribution was deformed by the interactions between beam and materials in the beam line. 74
5.12 The position dependence of pulse shapes obtained with cosmic rays. The horizontal axes show the distance from the upstream surface of a CsI crystal. The shape parameters (a) typical width, σ_0, and (b) asymmetry parameter, a, depend on the muon hit position. 75
5.13 A schematic view of the "shower maximum". The black line shows the fraction of energy deposit along the direction of photons as a function of the distance from the incident position. The "shower maximum" is defined as the energy-weighted mean position along the direction of the incident photons. 77
5.14 The correlation between the energy deposit and the relative value of the shape parameter, σ_0, in one crystal from the beam test data. The black dot shows the mean value of each energy range. The expected precision for different energy ranges was estimated by the width of the distribution of the shape parameter for each energy range. 77
5.15 The estimated precision of the obtained shape parameters as a function of energy: Left) typical width and Right) asymmetry parameter. 78
5.16 The distributions of the reduced χ^2 of the shape parameters. The black(red) histogram shows the signal(backward π^0 background). 78
5.17 The distributions of the likelihood ratio of the shape parameters. The black(red) histogram shows the signal(backward π^0 background). 79
5.18 An example of merged pulses made from the beam test data. The blue and pink waveforms are from different events in a FADC channel. The black waveform shows the merged pulse. 80
5.19 The correlation between the fitted pulse height and the reduced χ^2 of the fitting when we fit the pulse shapes of single pulses as a single pulse. The red line shows the energy dependent cut on the χ^2 value. 81

5.20 An example of the pulse shape rejected as multiple pulses. The reduced χ^2 value was 143.2 and it was much larger than the cut value, 29.2. The time difference of the original two pulses was 26 ns. 81

5.21 The estimated deposit energy distribution in a single channel during a spill based on a Monte-Carlo simulation. 82

5.22 The estimated inefficiency of the calorimeter due to the overlapped pulse (black dots) and other factors (red line). 82

6.1 A schematic view of the $K_L \rightarrow \gamma\gamma$ decay reconstruction from two photons. 84

6.2 The distributions of the differences between the reconstructed decay x-vertex(a)/z-vertex(b) and the Monte-Carlo true values of the $K_L \rightarrow \gamma\gamma$ decay. The black histogram shows the distribution with the assumption that the two photons come from the center of energy of the two photon system in xy-plane. The red histogram shows the distribution with the correction that the transverse momentum of the two photon system becomes zero. 85

6.3 The distributions of the differences between the reconstructed incident x-position and the Monte-Carlo true value for $K_L \rightarrow \gamma\gamma$ decay in the beam halo. The black histogram was obtained with the $K_L \rightarrow \pi^0\nu\bar{\nu}$ decay assumption. The red(blue) histogram was obtained with the $K_L \rightarrow \gamma\gamma$ decay assumption with COE(fitting) based method to reconstruct incident position. The positive sign was chosen to be in the direction of photons. 85

6.4 The correlation between the reconstructed z-vertex and the transverse momentum, P_T, of the assumed π^0 for $K_L \rightarrow \pi^0\nu\bar{\nu}$ (a) and $K_L \rightarrow \gamma\gamma$ (b). All the cuts except the new incident angle cut were applied. The black square in each plot shows a signal box. 86

6.5 The likelihood ratio distribution for $K_L \rightarrow \pi^0\nu\bar{\nu}$ (black) and $K_L \rightarrow \gamma\gamma$ (red). The areas of the histograms were normalized to 1. 86

6.6 The correlation between energy and the partial signal likelihood, L_{ij}^{signal} in Equation 6.1, of photons on the x/y axis for $K_L \rightarrow \pi^0\nu\bar{\nu}$ signal and $\eta \rightarrow \gamma\gamma$ background events. 87

6.7 Examples of the response functions of veto detectors, commonly used in the KOTO collaboration: a) The detection inefficiency of MB for photons for various incident angles as a function of the incident energy, and b) The detection inefficiency of CV for charged particles as a function of the incident momentum. 88

6.8 The distributions of reconstructed energy (left) and difference between the reconstructed/smeared position and Monte-Carlo true value (right). The black dots show the result obtained with the full simulation, and the red histogram shows the result obtained with the response function of the calorimeter in the fast simulation. 89

7.1 A schematic view of the constant fraction method. The black dots show the recorded pulse shape, the red line shows the template based fitted function, and the blue line shows the linear function to define the timing based on the constant fraction method. The red(blue) dashed lines show the pulse height and the timing at the peak(constant fraction). 93

7.2 The timing resolution of various methods as a function of deposit energy. The black(red) dots show the timing resolution obtained with data with fitted peak timing(CFM). The black(red) line shows the timing resolution obtained with the pulse shape simulation with fitted peak timing(CFM). 94
7.3 An example of the pulse shapes for which we failed to define the timing with CFM. The black dots show the recorded pulse shape, the red line shows the template based fitted function, and the blue line shows the linear function for CFM. The red dashed line shows the fitted pulse height and the fitted timing. The blue dashed line shows a half of the pulse peak height. The peak pulse height corresponds to about 1 MeV. 95
7.4 The rejection power of the new incident angle cut against the $K_L \to \gamma\gamma$ background as a function of the efficiency of the cut for the $K_L \to \pi^0\nu\bar{\nu}$ decay. 96
7.5 The estimated signal to background ratio, S/N, as a function of the efficiency of the cut for the $K_L \to \pi^0\nu\bar{\nu}$ decay. The black(red) dots show the result with the upgraded MB before(after) the optimization. 96
7.6 The position resolution as a function of the incident angle with the fitting method (solid lines) and the energy-weighted mean method (dashed line) for crystal sizes: 25mm(black), 50mm(red) and 75mm(blue). The RMS value of the distribution of distance between the reconstructed position and Monte-Carlo true value, was used as a position resolution in this plot. 97
7.7 The position resolution with the fitting based method as a function of the true incident angle. The round dots show the results obtained with the templates for the true incident angles plus 0°(black), 2.5°(red), 5°(blue), 7.5°(magenta), 10°(green) and 12.5°(light-blue). The orange squares show the position resolution obtained with beam test data. The distribution of the distance between the reconstructed position and the hit position measured with scintillating fibers was fitted with Asymmetric Gaussian (Equation 3.17), and its σ_0 was used as the position resolution in this plot. 98
7.8 The difference of the calculated polar angles of photons between with the $K_L \to \pi^0\nu\bar{\nu}$ assumption and with the $K_L \to \gamma\gamma$ assumption, obtained with the Monte-Carlo simulation with all the cuts except for the incident angle discrimination applied. The black(red) line shows the result for the $K_L \to \pi^0\nu\bar{\nu}(K_L \to \gamma\gamma)$ decay. Of the two photons, the larger difference was filled in this plot. 98
7.9 The neutron profiles in x-plane estimated with Geant3(black) and FLUKA(red)[17]. The integrals of both histograms were normalized to 1. 99

A.1 The reduced χ^2 of the fitting is shown as a function of the fitted pulse height. The dots show the result obtained with Asymmetric Gaussian (black), Crystal Ball function (red), Equation A.2 (blue) and Equation A.4 (magenta), respectively. The height dependences obtained with those functions except Asymmetric Gaussian were parameterized with the function (Equation A.6), and the solid lines show the fitted functions. 102
A.2 The reduced χ^2 of the fitting is shown as a function of the fitted pulse height. The black(red) dots show the reduced χ^2 obtained with Asymmetric Gaussian (templates). Parameters of the Asymmetric Gaussian except for the pulse height and timing were fixed on fitting. 103

List of Tables

6.1 The background estimation methods. Due to the limitation of the Monte-Carlo statistics, the number of background events were estimated in the following three ways. A full simulation means the ordinal detector simulation with full shower generation, and a fast simulation is based on the detector response function evaluated in advance. 89

6.2 The expected number of signal and background events in the KOTO experiment. The numbers in the table are normalized to 1.85×10^{14} K_Ls at the exit of beam line assuming 2×10^{14} protons on target per spill and 12 month long beam time. The method column indicates the Monte-Carlo simulation procedure shown in Table 6.1 : 1=full , 2=calorimeter:full+veto:fast, and 3=fast. The numbers with parentheses were obtained by assuming the same efficiency as signal for the incident angle cut. 90

Chapter 1

Introduction

The KOTO experiment is an experiment dedicated to observe the rare decay of long-lived neutral kaons, $K_L \to \pi^0 \nu\bar{\nu}$. We start with the introduction about the $K_L \to \pi^0 \nu\bar{\nu}$ decay and the KOTO experiment. We will then move on to the purpose and the outline of this thesis.

We have successfully achieved to build the Standard Model (SM) in particle physics. The Standard Model can represent almost all the processes. It can even describe CP violation in the weak interaction naturally. The Standard Model, however, cannot describe all the phenomena. For example, the CP violation is one of the requirements to make the matter-dominant universe[1], but the amount of the CP violation explained by the Standard Model is not large enough to make the matter-dominant universe. It also cannot explain the galaxy rotation curve, which requires some additional mass called "dark matter". We thus believe there is a new physics beyond the Standard Model; we should examine the Standard Model, and search for the new physics. The $K_L \to \pi^0 \nu\bar{\nu}$ decay is a good probe for such purposes.

1.1 $K_L \to \pi^0 \nu\bar{\nu}$ decay

Figure 1.1 shows a Feynman diagram of the $K_L \to \pi^0 \nu\bar{\nu}$ decay. The decay process is mediated by the second order diagrams of the electroweak interactions with the conversions within three generations in the quark sector: $s \to t \to d$. In the Standard Model, the Lagrangian of the charged current in the weak interaction is given by:

$$L_{CC} = \frac{g}{\sqrt{2}}[\bar{u}_i V_{ij} d_j W^- + \bar{d}_j V_{ij}^* u_i W^+] , \tag{1.1}$$

where $u_i = (u, c, t)$ are left-handed up-type quarks, $d_i = (d, s, b)$ are left-handed down-type quarks, and $W^\pm$ are the weak bosons. The V_{ij} is the 3×3 unitary Cabibbo-Kobayashi-Maskawa (CKM) matrix which connects the up-type quarks with the down type quarks:

$$V = \begin{pmatrix} V_{ud} & V_{us} & V_{ub} \\ V_{cd} & V_{cs} & V_{cb} \\ V_{td} & V_{ts} & V_{tb} \end{pmatrix} . \tag{1.2}$$

Wolfenstein parameterized the matrix through an expansion in powers of $\lambda = |V_{us}| = 0.22$[2]:

$$V \sim \begin{pmatrix} 1-\lambda^2/2 & \lambda & A\lambda^3(\rho - i\eta) \\ -\lambda & 1-\lambda^2/2 & A\lambda^2 \\ A\lambda^3(1-\rho-i\eta) & -A\lambda^2 & 1 \end{pmatrix} , \tag{1.3}$$

where η is a real number coefficient which represents an imaginary part of the CKM parameters. The long lived neutral kaon, K_L, is approximately represented by a superposition of the K^0 and $\overline{K^0}$:

$$|K_L\rangle \sim \frac{1}{\sqrt{2}}(|K^0\rangle - |\overline{K^0}\rangle) . \tag{1.4}$$

The amplitude of the $K_L \to \pi^0 \nu\bar{\nu}$ decay can then be expressed as:

$$\begin{aligned} A(K_L \to \pi^0 \nu\bar{\nu}) &\sim \frac{1}{\sqrt{2}}(A(K^0 \to \pi^0 \nu\bar{\nu}) - A(\overline{K^0} \to \pi^0 \nu\bar{\nu})) \\ &\propto V_{td}^* V_{ts} - (V_{td}^* V_{ts})^* \\ &\propto 2i\eta . \end{aligned} \tag{1.5}$$

The branching ratio of the $K_L \to \pi^0 \nu\bar{\nu}$ decay is thus proportional to η^2, and the decay is induced directly by the CP violation in the weak interaction.

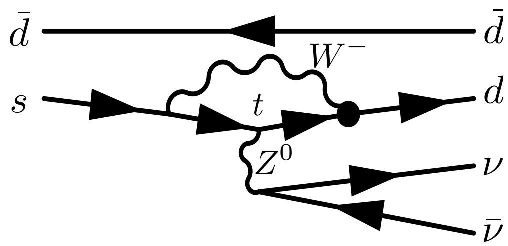

Figure 1.1: A Feynman diagram of the $K_L \to \pi^0 \nu\bar{\nu}$ decay.

The branching ratio of the $K_L \to \pi^0 \nu\bar{\nu}$ decay is represented in the Standard Model as [3]:

$$Br(K_L \to \pi^0 \nu\bar{\nu}) = 6.87 \times 10^{-4} \times Br(K^+ \to \pi^0 e^+ \nu) \times A^4 \lambda^8 \eta^2 X^2(x_t) , \tag{1.6}$$

where x_t is the square of the ratio of the top quark to the W boson masses, $x_t = m_t^2/m_W^2$, and $X(x_t)$ is the Inami-Lim loop function with higher order QCD corrections[4]. We can calculate the branching ratio with an exceptional precision, because the contributions from the long distance interaction are negligibly small, and the hadronic matrix elements are extracted directly from experimental measurements of the branching ratio of the decay: $K^+ \to \pi^0 e^+ \nu$. The theoretical uncertainty in the branching ratio of the decay is only 1-2 % [5]. Based on the Standard Model calculation with the measured CKM parameters, the branching ratio of the $K_L \to \pi^0 \nu\bar{\nu}$ decay is predicted to be[6]:

$$Br(K_L \to \pi^0 \nu\bar{\nu}) = (2.43 \pm 0.39) \times 10^{-11} . \tag{1.7}$$

The uncertainty is dominated by the currently measured CKM parameters. If we measure the branching ratio, we can thus determine η directly with a good precision.

As shown in Fig. 1.1, the $K_L \to \pi^0 \nu\bar{\nu}$ decay occurs via loop diagrams. If a non-SM particle propagates in the loop, the branching ratio of the $K_L \to \pi^0 \nu\bar{\nu}$ decay may be different from the Standard Model prediction. Because the decay directly violates the CP symmetry, the deviation of the branching ratio from the Standard Model prediction also implies new sources of the CP violation. One of major models of new physics beyond the Standard Model is Minimal Supersymmetric Standard Model (MSSM), which is the minimal extension to the Standard Model, including supersymmetry (SUSY). The general MSSM can have new CP violation sources, and can enhance the branching ratio of the $K_L \to \pi^0 \nu\bar{\nu}$ decay to a few times 10^{-10}[7]. It is about 10 times larger than the SM prediction.

A decay mode, $B_0 \to J/\psi K_S$, can also determine the CP violation phase with a small uncertainty in B meson system. The CP violation arises from $B_0 - \overline{B_0}$ mixing and it is called indirect CP violation. In the general MSSM, the amount of CP violation in $K_L \to \pi^0 \nu\bar{\nu}$ decay can be different from the one in the indirect CP violation.

In the Minimal Flavor Violation (MFV) hypothesis, there are no additional CP violation phases, and the flavor mixing can be explained only by the CKM matrix in the Standard Model. Deviations of the branching ratio from the SM prediction, thus, is small (∼20 %) in MFV models[8, 9]. Because there are no additional CP violation phases, the amount of CP violation in $K_L \to \pi^0 \nu\bar{\nu}$ decay should be the same as the one in the indirect CP violation.

By measuring the branching ratio of the $K_L \to \pi^0 \nu\bar{\nu}$ decay and comparing the size of the CP violation with the SM and other experimental results, we can distinguish and constrain many theories. To measure the branching ratio of the $K_L \to \pi^0 \nu\bar{\nu}$ decay, the KOTO experiment was designed and is being prepared at J-PARC.

1.2 KOTO experiment at J-PARC

In order to reach the sensitivity of the SM prediction, we adopted a step-by-step approach. The E391a experiment at KEK-PS was performed as a pilot experiment for the KOTO experiment. We successfully established a basic experimental method, and obtained the upper limit[10, 11]:

$$Br(K_L \to \pi^0 \nu\bar{\nu}) < 2.6 \times 10^{-8} \quad (90\ \%\ \text{C.L.})\ . \tag{1.8}$$

By comparing the upper limit to the SM prediction (Equation 1.7), we have to improve the experimental sensitivity by 3 orders of magnitude. Because the result of the E391a experiment was limited by the number of K_L's available, we planed the KOTO experiment to use a high intensity proton beam of J-PARC. In the following subsections, we describe the experimental method of the KOTO experiment, and its background sources.

1.2.1 Experimental method

Figure 1.2 shows a conceptual view of the experiment. A decay volume for K_L is surrounded by particle detectors. The signature of a $K_L \to \pi^0 \nu\bar{\nu}$ decay is that there are two photons from a π^0 decay and no other visible particles in the final state. An electromagnetic calorimeter is placed downstream of the decay volume to detect the two photons. All the K_L decay modes except $K_L \to \pi^0 \nu\bar{\nu}$ and $K_L \to \gamma\gamma$ have at least two charged particles, or two or more extra photons in the final state. These decays can be rejected by detecting additional particles by the surrounding detectors for vetoing them. The $K_L \to \gamma\gamma$ decays can be rejected by requiring a finite transverse momentum for the two photon system. In case of the $K_L \to \pi^0 \nu\bar{\nu}$ decay, the two photon system has a finite transverse momentum, because the undetected two neutrinos take some momentum away.

We reconstruct the $K_L \to \pi^0 \nu\bar{\nu}$ decay from two photons in the calorimeter with the assumption that the two photons come from a π^0 decay on the z-axis. Figure 1.3 shows a schematic

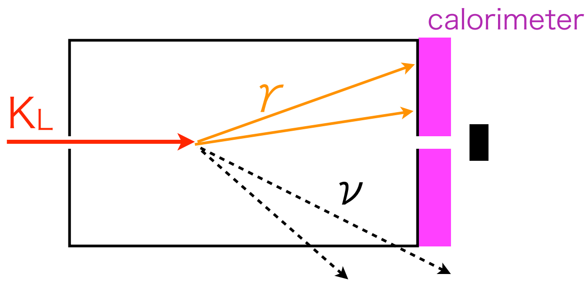

Figure 1.2: A conceptual view of the KOTO experiment.

view of the π^0 reconstruction. Once we find two photons in the calorimeter, the invariant mass of the two photons is represented by:

$$m_{\pi^0}^2 = 2E_1E_2(1 - \cos\theta_{12}) , \tag{1.9}$$

where m_{π^0} is the π^0 mass, E_i is energy of the i-th photon, and θ_{12} is the angle between the momenta of the two photons. The $\cos\theta_{12}$ is derivered from:

$$\begin{aligned}(\boldsymbol{r}_1 - \boldsymbol{r}_0) \cdot (\boldsymbol{r}_2 - \boldsymbol{r}_0) &= x_1x_2 + y_1y_2 + (z_1 - Z_{\mathrm{vtx}})(z_2 - Z_{\mathrm{vtx}}) \\ &= |\boldsymbol{r}_1 - \boldsymbol{r}_0||\boldsymbol{r}_2 - \boldsymbol{r}_0| \cos\theta_{12} ,\end{aligned} \tag{1.10}$$

where $\boldsymbol{r}_i = (x_i, y_i, z_i)$ is the incident position of the i-th photon in the calorimeter, and $\boldsymbol{r}_0 = (0, 0, Z_{\mathrm{vtx}})$ is the decay vertex of the π^0. The decay vertex position, Z_{vtx}, is calculated using these equations.

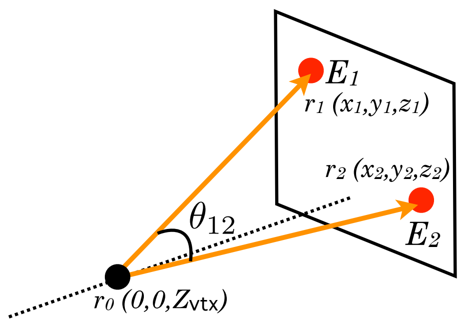

Figure 1.3: A schematic view of the π^0 reconstruction.

1.2.2 Background sources

We reconstruct the $K_L \to \pi^0\nu\bar{\nu}$ decay with the assumption that the two photons come from a π^0 decay on the z-axis. If the two photons are not from a π^0 decay, or if the two photons are not coming from the z-axis, we mis-calculate the decay vertex position, $Z_{\rm vtx}$, and such an event might be a background source. An $\eta(\to\gamma\gamma)$ or π^0 produced by the interaction between detector materials and neutrons in the beam halo (halo neutron), and $K_L \to \gamma\gamma$ decay in the beam halo (halo kaon) are such cases as shown in Fig. 1.4.

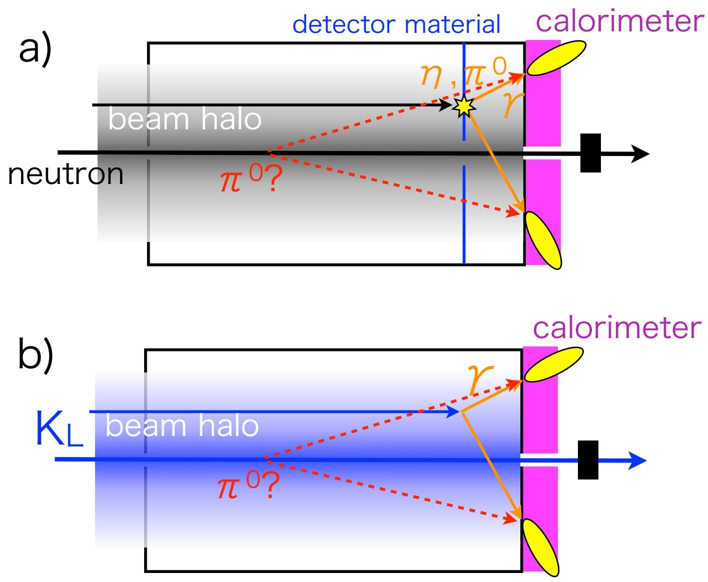

Figure 1.4: Schematic views of backgrounds caused by beam halo particles: a) $\eta(\to\gamma\gamma)$ or π^0 produced by the interaction between detector materials and halo neutrons, b) $K_L \to \gamma\gamma$ decay of the halo kaon.

Other backgrounds from K_L decays are caused by missing extra particles for some reasons. The major reason is simply the detection inefficiency of the detectors. Another reason that only applies to photons is to reconstruct two nearby photons in the calorimeter as one photon. This is called "fused cluster".

1.3 Detector upgrades

We give a brief description about the detector upgrades of the KOTO experiment. We are reusing the E391a detector with a number of upgrades. In those upgrades, this thesis will describe a study about the upgrades of a calorimeter and readout system. Details of the upgrades and other apparatus will be described in the next chapter.

1.3.1 Upgrade of electromagnetic calorimeter

The calorimeter for the E391a experiment consisted of 7 cm square CsI crystals. We replaced the crystals with smaller crystals to improve granularity and get more shower shape information of photons, as shown in Fig. 1.5. With the more information, we can reconstruct the incident position and angle more accurately, and identify shower shapes more precisely.

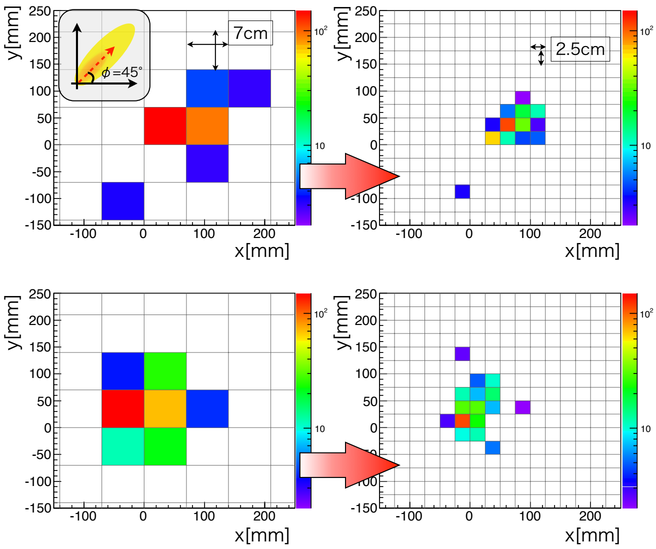

Figure 1.5: Schematic views of the improvement of the granularity of the calorimeter. The figures show the activities with 7 cm (left) and 2.5 cm (right) square crystals for the same events, in which 300 MeV photons hit the calorimeter with the 20° polar angle and 45° azimuthal angles. The squares in each figure correspond to crystals, and the color shows the deposit energy in each crystal in MeV.

Because the observable values from the calorimeter are the only information for signal-like events, performance of the calorimeter is crucial to discriminate signals from backgrounds. As described in Section 1.2.2, the reconstructed decay vertex position for backgrounds caused by halo kaons and neutrons are different from the real position. As shown in Fig. 1.4, this makes the incident angle of photons derived from the mis-reconstructed vertex different from the true incident angle. By improving incident angle resolution, we can suppress such backgrounds. Backgrounds caused by the fused cluster are also suppressed by the upgrade, because the shower shape of the fused cluster is different from the shape of a single photon.

1.3.2 Upgrade of readout system

Figure 1.6 shows a conceptual view of our waveform readout. If we simply read a signal from a CsI crystal with a 125 MHz FADC, only 1 or 2 samples can be taken on the rising edge and we cannot measure its timing precisely. If we put a Bessel filter before the digitization, signals are widened and several samples are recorded on their rising edges. The width of the widened pulse shape is about 27 ns in σ. By using the filter, we can measure their energy and timing more precisely.

The energy and timing resolutions obtained with the waveform readout might be different from the resolution obtained with normal ADC and TDC. Because it is our first time to use the Bessel filter for such an application, it is important to study and understand the performance obtained with the waveform readout.

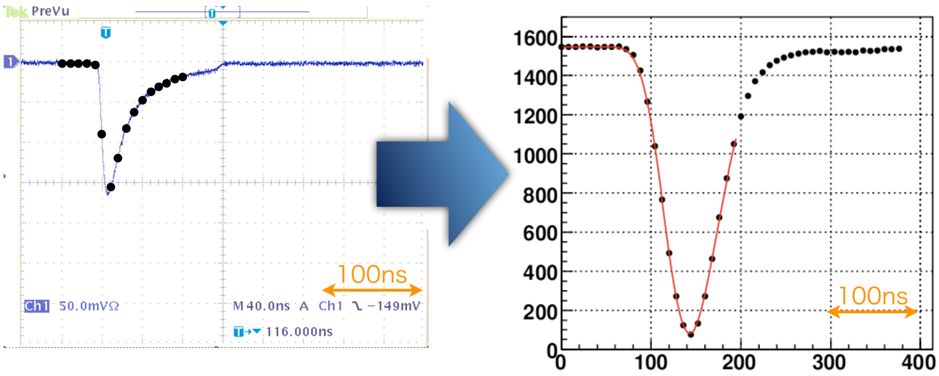

Figure 1.6: A conceptual view of our waveform readout with a Bessel filter. Figure on the left shows a signal from CsI crystal recorded by an oscilloscope. The black dots show an example of a 125 MHz sampling. Figure on the right shows a recorded pulse shape by FADC with the filter.

1.4 Purpose and outline of this thesis

Purposes of this thesis are the following:

1. Reveal and understand the performance of the upgraded calorimeter obtained with the waveform readout.

2. Fully utilize the upgraded calorimeter for suppressing backgrounds.

3. Estimate the realistic number of signal and background events, and evaluate the sensitivity of the KOTO experiment.

The $K_L \to \gamma\gamma$ decay, in particular, was not considered as a background source in the proposal of the KOTO experiment. Because the $K_L \to \gamma\gamma$ decay has no extra photons in the final state except two photons in the calorimeter, the decay in the beam halo can be a serious background source and only rejected by the calorimeter. We developed a new method to suppress the $K_L \to \gamma\gamma$ background, and estimated the number of the background events.

The outline of this thesis is the following. We first describe the apparatus of the KOTO experiment in Chapter 2. Next, we describe a beam test that we held to evaluate the performance of the calorimeter in Chapter 3. In Chapter 4, we then describe a study about the estimation method of the performance obtained with the waveform readout, and compare the estimation with the results obtained with data in the beam test. Next, we describe some new analysis methods for the upgraded calorimeter in Chapter 5. We estimate the expected number of signal and background events based on the new studies, and reestimate the sensitivity of the KOTO experiment in Chapter 6. We describe discussions on the improvement on the timing resolution and the experimental sensitivity in Chapter 7. At the end, we will conclude this thesis in Chapter 8.

Chapter 2

Apparatus of the KOTO experiment

In this chapter, we describe the apparatus of the KOTO experiment at J-PARC.

Protons in the J-PARC synchrotron are accelerated up to the kinetic energy of 30 GeV, and extracted to the experimental area for 0.7 seconds in every 3.3 seconds. The period during the extraction is usually called "spill". The K_L particles are generated by primary protons striking a target, and the K_L particles are transported through a neutral beam line to the KOTO detector.

Section 2.1 describes the neutral beam line. Section 2.2 explains the detector system of the KOTO experiment.

2.1 Beam line

Figure 2.1 shows an overview of the beam line. A common target is placed in the proton beam line and consists of five Ni disks with the total thickness of 53.9 mm. The target and the neutral beam line set on a same axis, and the neutral beam line is located 16° from the primary proton beam line in a horizontal plane. The beam line consists of a pair of collimators, a sweeping magnet, and a γ absorber, and it is 21 m long. The first collimator is 400 cm long, and the second collimator is 500 cm long. They are made of iron, except for the 50 cm long region at the upstream end, which are made of tungsten. The magnet is placed between the two collimators to sweep out charged particles, and its magnetic field is 2 Tesla with the current of 2.2 kA. The γ absorber is made of 7 cm long lead.

Figure 2.2 shows estimated neutron profiles[12]. As described in Section 1.2.2, the beam halo is one of the background sources. The halo neutron flux is suppressed by 5 orders of magnitude than the core neutron flux, which corresponds to 10 times improvement from the E391a. It helps to suppress backgrounds.

Figure 2.3 shows data and Monte-Carlo K_L momentum spectra at the exit of the beam line, which is 21 m downstream from the target[13]. Because the spectra vary between different Monte-Carlo packages, we use the measured spectrum in this thesis. Based on the measurement, the estimated number of K_L at the exit of the beam line is 1.94×10^7 per spill with 2×10^{14} protons on target.

2.2 KOTO detector

Figure 2.4 shows a detector overview of the KOTO experiment. As described in Section 1.2.1, the decay volume is surrounded by hermetic particle detectors. The downstream side is covered with

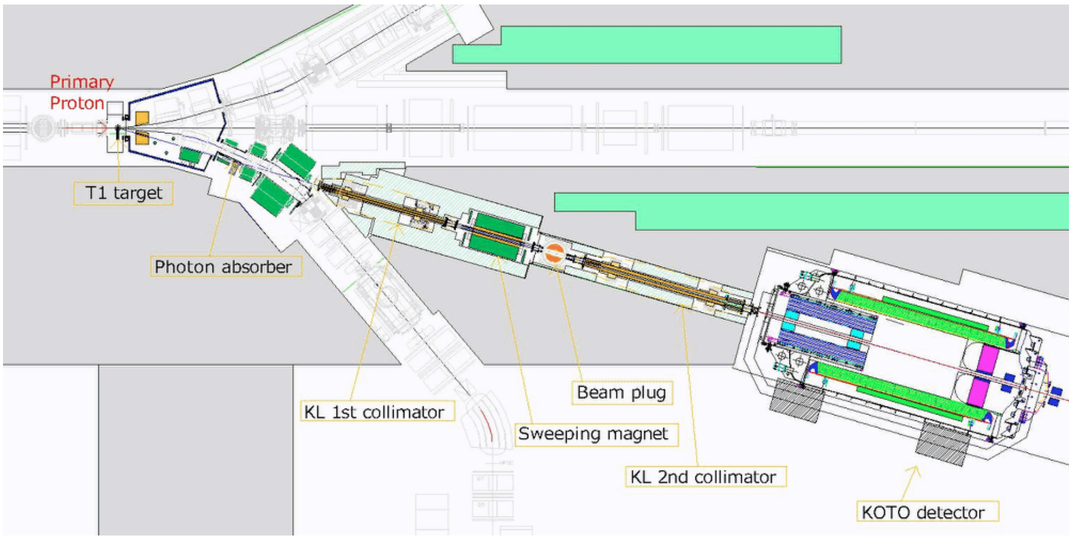

Figure 2.1: A schematic view of the neutral beam line. A common target in the proton beam line and the neutral beam line set on a same axis, and the neutral beam line is located 16° from the primary proton beam line in a horizontal plane. The beam line consists of a pair of collimators, a sweeping magnet, and a γ absorber, and it is 21 m long. The KOTO detector is placed just downstream of the second collimator.

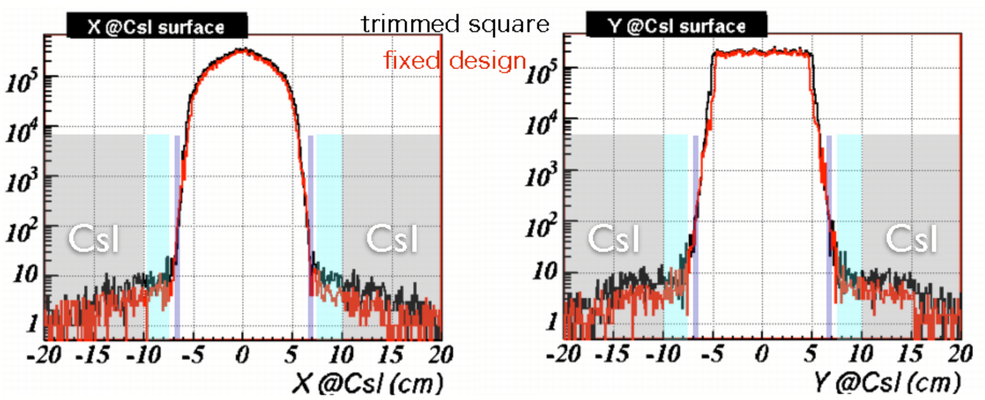

Figure 2.2: The estimated neutron profiles in horizontal(left) and vertical(right) axes[12]. The red histogram shows the result with the final design, black histogram shows the result before the final optimization.

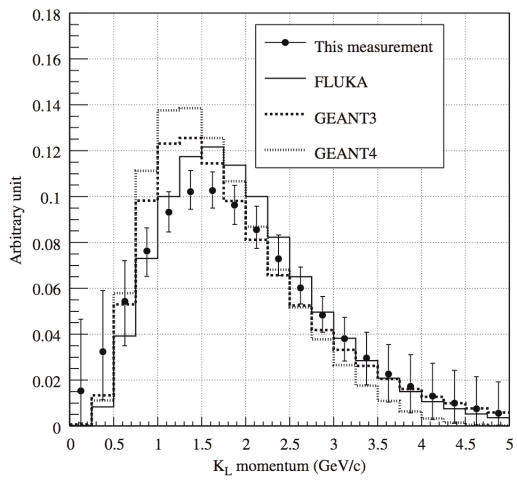

Figure 2.3: The K_L momentum spectra at the exit of the beamline, 21 m downstream from the target[13]. Dots show the data, and histograms show the simulation results obtained with FLUKA(solid line), GEANT3(dots) and GEANT4(dashed line).

an electromagnetic calorimeter to measure the energies and incident positions of two photons from a π^0. All other detectors are used for vetoing extra particles.

In the following subsections, we give a description about the electromagnetic calorimeter, data acquisition system and other veto counters.

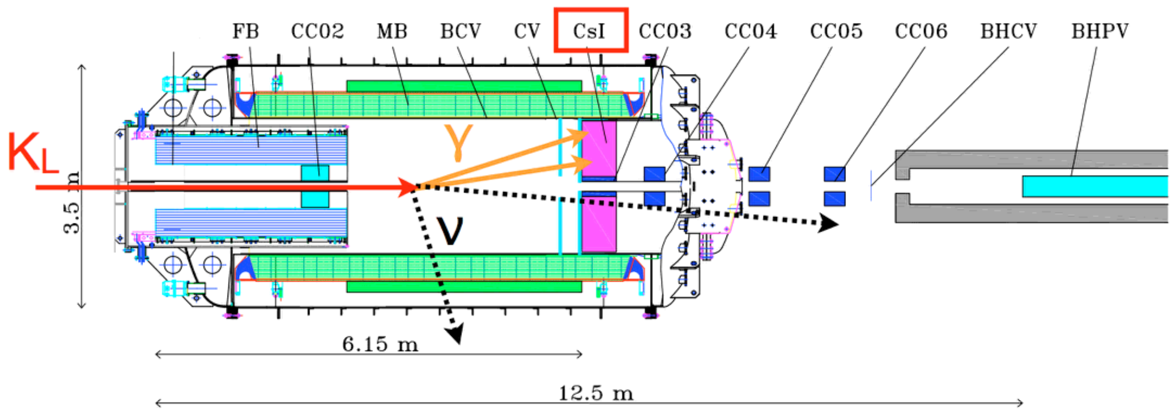

Figure 2.4: A side view of the KOTO detector. The decay volume at the middle of the detector is surrounded by hermetic particle detectors. There is a calorimeter at the downstream of the decay volume. The other detectors are used for vetoing extra particles.

2.2.1 Electromagnetic calorimeter

As described in Section 1.3.1, the electromagnetic calorimeter for the KOTO experiment was upgraded. There were two major purposes of the calorimeter upgrade. One of them was to improve granularity in order to get more shower shape information of photons. It helps to distinguish the fused clusters generated by two nearby photons. The other purpose was to increase the thickness of the calorimeter. It helps to reduce the shower leakage in order to improve the energy measurement. It also helps to reduce the photon detection inefficiency caused by photons punching through the calorimeter.

Figure 2.5 shows a front view of the CsI calorimeter for the KOTO experiment. To satisfy the above purposes, 496 pieces of the E391a crystals with the dimension of $7 \times 7 \times 30$ cm^3 were replaced by 2240 crystals with the dimension of $2.5 \times 2.5 \times 50$ cm^3 (”small” type) and 476 crystals with the dimension of $5 \times 5 \times 50$ cm^3 (”large” type). Those are pure CsI crystals used at the Fermilab KTeV experiment.

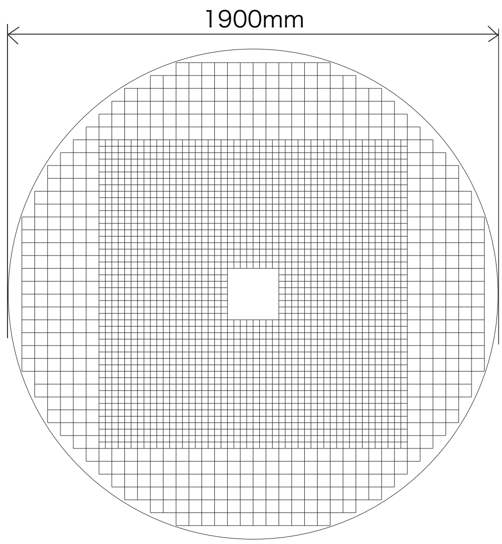

Figure 2.5: A front view of the CsI calorimeter for the KOTO experiment. It consists of 2240 ”small” crystals and 476 ”large” crystals. The calorimeter is 50 cm long in depth.

Each crystal is wrapped with a 13 μm thick Aluminized mylar. Each small(large) crystal is viewed from the downstream by a 3/4(1.5) inch Hamamatsu R5364(R5330) PMT through a 4.6 mm thick silicone cookie and UV transmitting filter. Since these crystals and PMTs will be operated in vacuum, the heat generated by their HV bleeder should be suppressed. We developed a custom Cockcroft-Walton base (CW base) to supply HV to PMTs with a smaller heat generation (60 mW in the CW circuit[1]).

The gain of each PMT is monitored by a laser calibration system. A 355 nm wavelength laser is emitted to 9-Methylcarbazole liquid scintillator. The pulse shape from the scintillator is similar to the pulse shape of the CsI crystal. The light yield from the scintillator is monitored by a PIN photo diode. The light from the scintillator is also distributed to the downstream surface of all the crystals through quartz fibers. By tracking the PMT output of the liquid scintillator light normalized by the PIN photo diode output, we can monitor the gain of each PMT.

[1] 90 mW at preamplifier in the CW base

2.2.2 Data acquisition system and readout

The estimated decay rate of K_L in the KOTO detector is about 3 MHz with the full intensity, 2×10^{14} protons on target per spill. To take data effectively with the high intensity beam at J-PARC, the data acquisition (DAQ) system should also be upgraded. Figure 2.6 shows an overview of the DAQ system. Signals from all the detectors are digitized by Flash ADC (FADC) boards, and the digitized waveform data is stored in the boards temporally for 4 μs. Each FADC board receives 16 analog inputs, calculates local sum of them and sends the sum to one of Level1(L1) trigger boards every 8 ns. A master control board of this DAQ system called MACTRIS communicates with the L1 trigger boards, generates L1 triggers based on those sum, and sends them to the FANOUT boards. The FANOUT boards fan-out the triggers and also clock signals to each FADC board. When a FADC board receives a trigger, the board sends corresponding waveform data to a so called Level2(L2) trigger board. The L2 trigger board has dual memories on it, and keeps storing data sent from the FADC boards during a spill after some event selections. The stored data is sent to an event building system during the next spill.

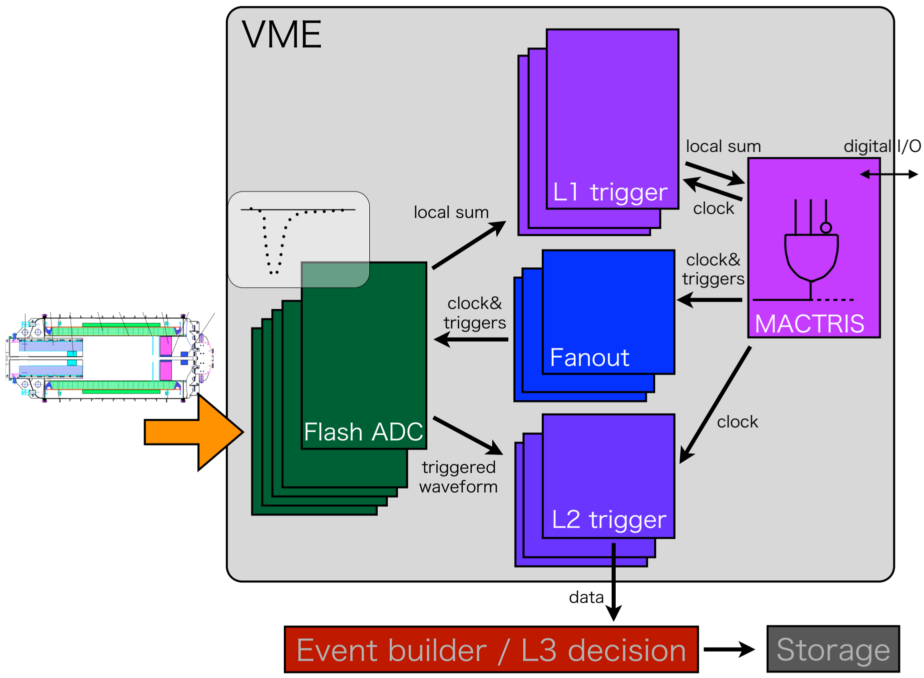

Figure 2.6: An overview of the DAQ system for the KOTO experiment. Signals from all the detectors are read out by Flash ADC boards. A MACTRIS board generates triggers based on the digitized signals from FADCs with L1 trigger boards. The corresponding data for a trigger is sent to an event building system through L2 trigger boards after some event selections.

The estimated L1 trigger rate is 200 kHz. With the upgraded DAQ system, we can take data without any dead time. It is suitable to take data under the high intensity beam. Furthermore data are stored in a pipeline (digital delay) during the trigger generation. This eliminates delay cables, and prevents the signal from blunting. It is a big advantage for detecting small pulses in veto counters.

As described in Section 1.3.2, we decided to record waveform with FADC. The FADC was required to have 14 bit dynamic range for the calorimeter, and the total number of channels is about 3800. To achieve the required specification at a reasonable cost, we decided to put the Bessel filter before digitization, and record the output with 125 MHz FADCs.

Figure 2.7 shows a photograph of the FADC board and the circuit diagram of the Bessel filter. The FADC board was developed at the University of Chicago. On the front-panel, it has 16 analog input channels, digital I/O to receive clock signals and triggers, and 2 pairs of optical links to send data to L1 and L2 trigger boards. There are 10-pole Bessel filters between the connectors for analog inputs and FADC chips. The digitized waveforms are processed by an FPGA[2] chip on it.

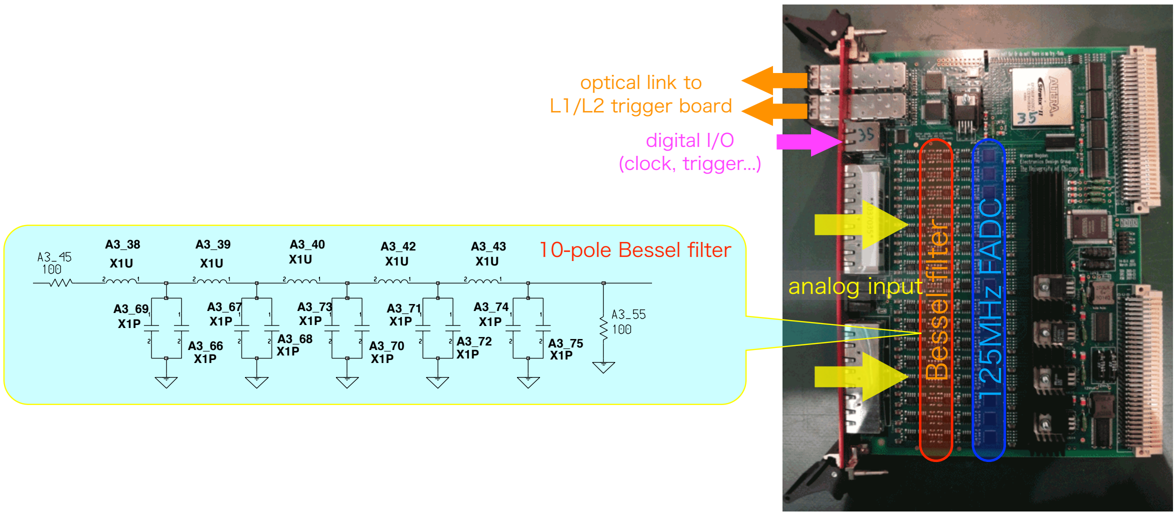

Figure 2.7: A photograph of the FADC board (right) and the circuit diagram of the Bessel filter (left). The FADC board was developed at the University of Chicago. It has 16 analog input channels. Input signal is passed to the Bessel filter, and the output from the filter is recored by 125 MHz FADC.

2.2.3 Other veto counters

The KOTO experiment has the following veto counters as shown in Fig. 2.4.

Figure 2.8 shows a schematic view of detectors in the upstream section. There are Front Barrel (FB) and Collar Counter 02 (CC02) to suppress K_L decays that occur upstream of the decay volume. The FB consists of 16 modules that are made of 59 layers of alternating lead and plastic scintillator plates (16 X_0 thick and 2.75 m long). The CC02 is made of pure CsI crystals as shown in Fig. 2.9, and it is placed at the entrance of the main decay volume, surrounding the neutral beam. The CC02 is prepared not only to detect photons from K_L decays, but also to measure the flux and energy spectrum of halo neutrons.

Figure 2.10 shows a schematic view of detectors in the middle section. Main Barrel (MB) surrounds the side of the decay volume. The MB consists of 32 modules, and each module consists of an existing module for the E391a experiment and an additional module for upgrade.

[2] Field-Programmable Gate Array (FPGA) is an integrated circuit which we can configure after manufacture with a Hardware Description Language just like softwares.

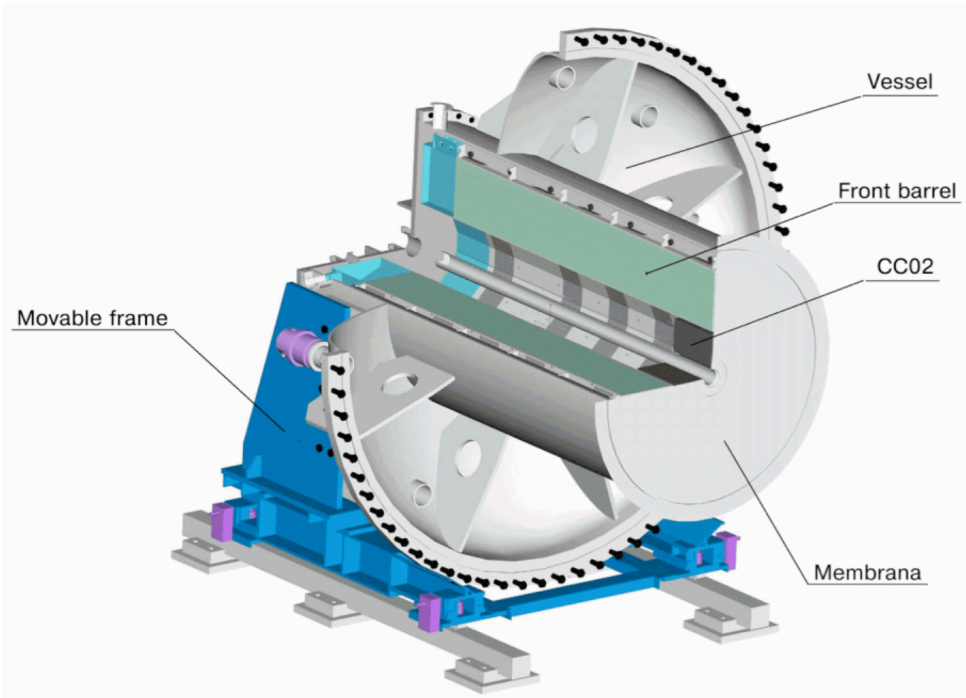

Figure 2.8: A schematic view of detectors in the upstream section. The FB and CC02 are placed upstream of the decay volume.

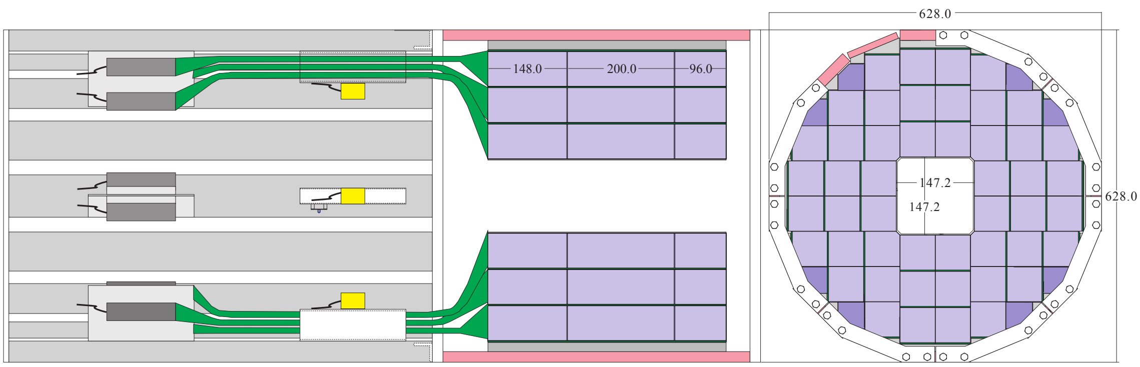

Figure 2.9: A schematic view of CC02. The CC02 is segmented into multiple crystals along both the longitudinal and perpendicular directions, to measure the flux and energy spectrum of halo neutrons.

The module for E391a is a lead and plastic scintillator sandwich calorimeter. The thickness of each scintillator plate is 5 mm. The lead plates for the inner 15 layers are 1 mm thick each, and the outer 29 layers are 2 mm thick. The total thickness of the existing modules is 14 X_0, and the length is 5.5 m. We plan to add 5 X_0 thick modules inside the existing modules. In the most inner part of the Main Barrel, a pair of 5 mm thick plastic scintillators are placed to identify charged particles.

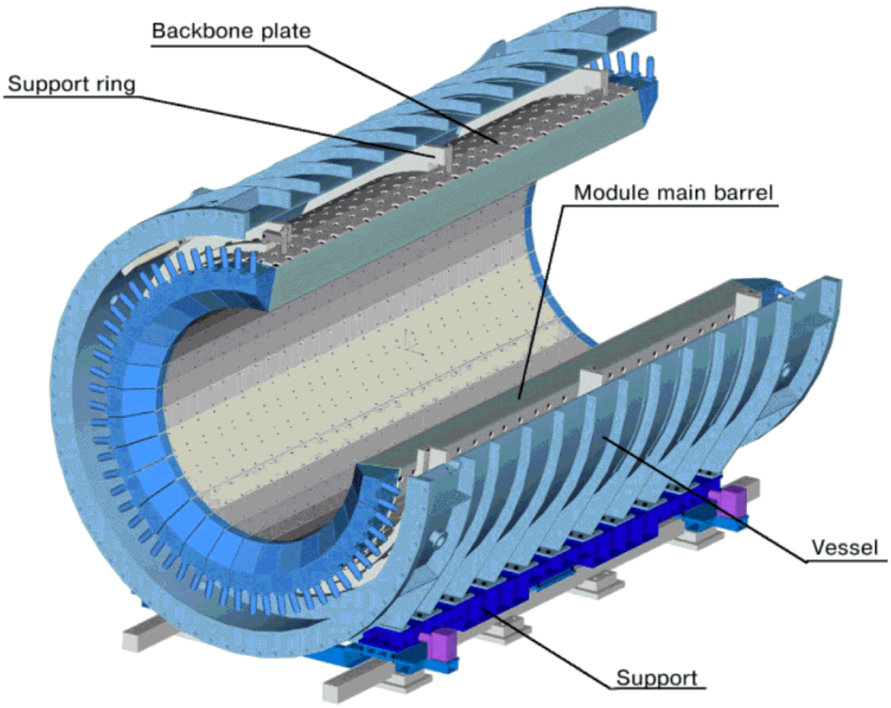

Figure 2.10: A schematic view of detectors in the middle section. The MB surrounds the side of the decay volume.

Figure 2.11 shows a schematic view of Charged Veto (CV). The CV is placed in front of the CsI calorimeter to detect charged particles hitting the calorimeter. It consists of two layers. One of them is placed on the upstream surface of the calorimeter, and the other is placed 25 cm upstream of the calorimeter. Each layer consists of 3 mm thick plastic scintillators.

Figure 2.12 shows a schematic view of detectors in the downstream section. The CC03 and Liner CV (LCV) are placed along the beam hole of the calorimeter. The CC03 is made of pure CsI crystals to detect photons. The LCV is made of 3 mm thick plastic scintillators to detect charged particles. Outer Edge Veto (OEV) surrounds the calorimeter to fill gaps between the calorimeter and the support structure. It consists of alternating lead and plastic scintillator plates.

Downstream counters, CC04-CC06, surround the neutral beam to detect photons passing along the beam. Those will be made of pure CsI crystals.

Beam Hole CV (BHCV) is set at 4 m downstream of the CsI calorimeter, and consists of 3 mm thick plastic scintillators to detect charged particles in the beam core.

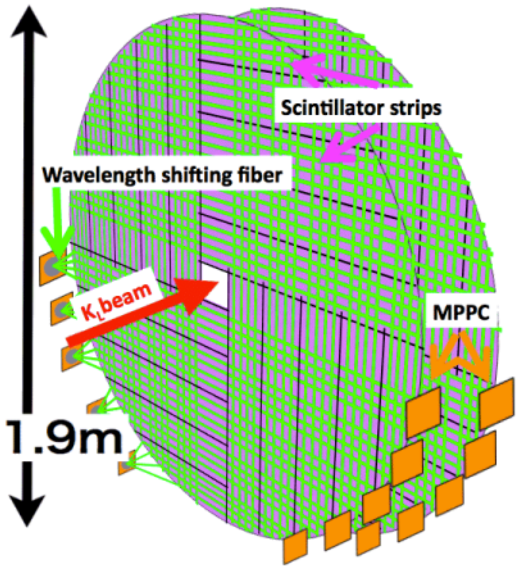

Figure 2.11: A schematic view of CV. It consists of two layers. The CV is placed in front of the CsI calorimeter.

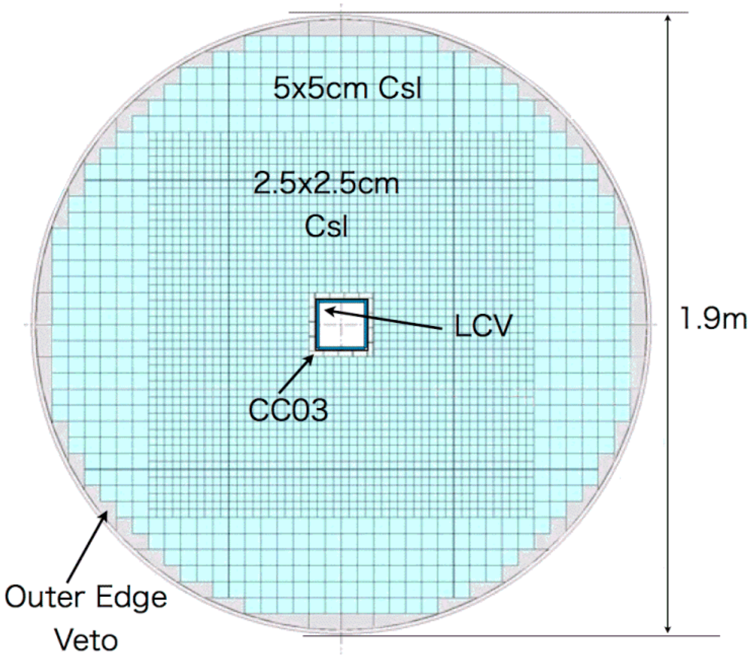

Figure 2.12: A schematic view of detectors in the downstream section. The CsI calorimeter is placed downstream of the decay volume. The CC03 and LCV are placed along the beam hole of the calorimeter. The OEV surrounds the calorimeter to fill gaps between the calorimeter and the support structure.

Beam Hole Photon Veto (BHPV) is placed at the downstream end of our detector system, and starts at 6.3 m downstream of the calorimeter. To suppress shower components going back to other veto counters, BHPV is placed in a radiation shield. The BHPV consists of 25 Cerenkov counter modules shown in Fig. 2.13. Each module is composed of a lead plate, a stack of aerogel tiles, a mirror, a Winston cone, and a PMT. The lead plate converts photons to electrons and positrons, and the aerogel tiles emit Cerenkov light with the electrons and positrons. The mirror and the Winston cone guide the Cerenkov light to the PMT. By using Cerenkov light, BHPV is not sensitive to heavy particles in the beam core.

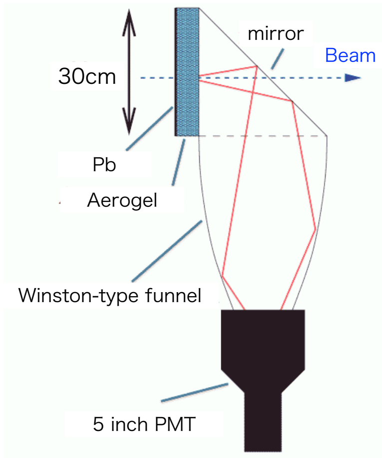

Figure 2.13: A schematic view of BHPV module. The module consists of a lead plate, a stack of aerogel tiles, a mirror, a Winston cone, and a PMT.

Chapter 3

Performance evaluation of the CsI calorimeter

We held a beam test at the Research Center for Electron Photon Science (LNS at that time) in the Tohoku University, to reveal the basic performance of the CsI calorimeter: energy resolution, timing resolution and position resolution. We measured those resolutions for different beam energies and different incident angles.

In the following sections, Section 3.1 first describes the apparatus of the beam test. Next, Section 3.2 describes a study of the pulse shape analysis. Section 3.3 describes the basic energy calibration, and Section 3.4 describes the energy calibration with beam. Section 3.5 and 3.6 describe energy and timing resolutions, respectively. At the end, Section 3.7 describes the summary of this chapter.

3.1 Experiment

Figure 3.1 shows a photograph of the beam test apparatus. The beam test apparatus consisted of a e^+ beam, a scintillating fiber position detector and a CsI array. The position detector was placed just upstream of the CsI array to define the incident positions of incoming e^+s. The CsI array and the position detector are mounted on a table to change the incident angle and position of the e^+s. A dry room was prepared to keep the CsI crystals dry.

We define the coordinate system as the following. The positive z-axis points in the beam direction, the positive y-axis points up, and the x-axis is defined to satisfy the relation of the right-hand system: $\boldsymbol{x} = \boldsymbol{y} \times \boldsymbol{z}$.

We will explain the e^+ beam, the scintillating fiber position detector, the CsI calorimeter, the data acquisition system and the run conditions in the following subsections.

3.1.1 e^+ beam

The LNS had a circular accelerator, and it provided e^-s with energies up to 1.2 GeV. By inserting thin carbon fibers in the beam line, photons were generated by Bremsstrahlung. The photons were transported to the laboratory where we held the beam test. The photons hit a 20 μm thick Au foil converter, and generated $e^\pm$s. Figure 3.2 shows the e^+ beam line in the laboratory[14]. The size of the $e^\pm$ beam was defined by a Pb collimator located downstream of the foil. A dipole magnet was located just downstream of the collimator to select e^+s and to

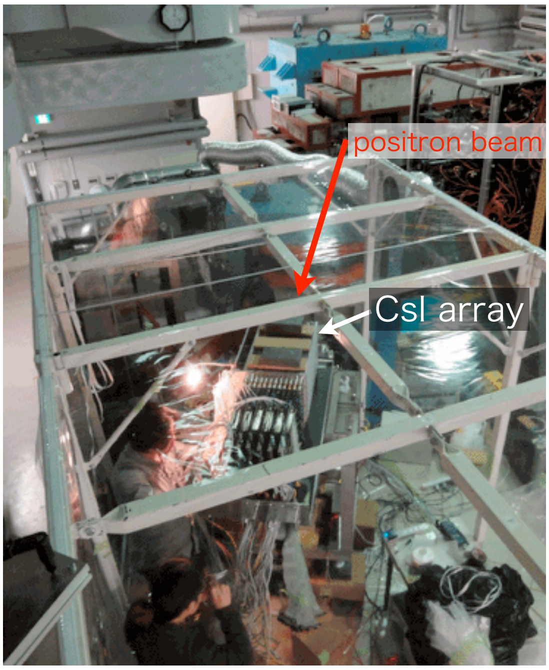

Figure 3.1: A photograph of the beam test apparatus. The beam test apparatus consisted of a e^+ beam, a scintillating fiber position detector and a CsI array. The CsI array was mounted on a turntable on the X-stage. The X-stage was placed in a dry room.

analyze their momenta. The e^+s with a selected momentum were transported to the second Pb collimator through a vacuum pipe placed at 30° in a horizontal plane with respect to the initial photons. The collimated e^+s passed through the air to the experimental area. The experimental area was located about 5 m downstream of the second collimator.

The repetition cycle of the e^+ beam was 14 seconds and the duty factor was 50 %. The beam intensity was about 1.3 kHz during the beam test. The highest e^+ beam energy available was 840 MeV. The beam energy range was similar to the energy range of photons expected at the KOTO experiment. The beam profile was about 20 mm wide in σ in x and y directions.

3.1.2 Scintillating fiber position detector

A detector made of scintillating fibers was placed in front of the CsI crystals in order to measure the incident position of each e^+. Figure 3.3 is a photograph of the position detector. It consisted of two layers for x&y views, and each layer consisted of 48 scintillating fibers. The cross section of each fiber was 1 mm square. The overlapped area of the two layers was 48 mm square. The light from the fibers was detected by Hamamatsu H8711-10 multi-anode PMTs.

The typical light yield was 6-8 photoelectrons per Minimum Ionization Particle (MIP). Signals from the fibers were discriminated at a threshold of 1-2 photoelectrons to measure the timing of the hit.

The position resolution of the CsI calorimeter will be evaluated with this position detector in Section 5.1.

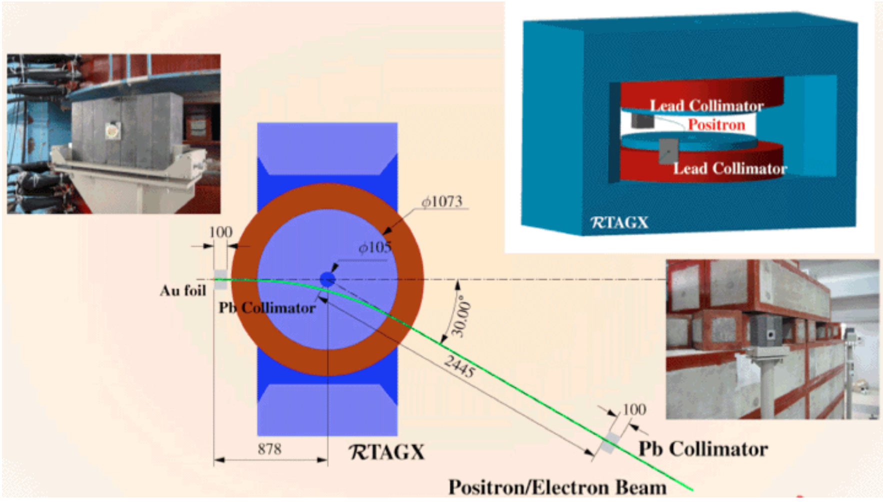

Figure 3.2: A schematic top view of the e^+ beam line[14]. The beam line consists of a 20 μm thick Au foil as a target, a pair of Pb collimators, and a dipole magnet labeled $\mathcal{R}$TAGX in this figure. The strength of the magnetic field of the dipole magnet was 1.2 T at a maximum. The e^+ beam size was defined by the hole with the diameter of 20 mm in the second collimator. Photographs are the Au foil and the first Pb collimator, the dipole magnet, and the second Pb collimator.

Figure 3.3: A photograph of the scintillating fiber position detector and the CsI array. The position detector was placed just in front of the CsI crystals (black elements with white labels). It consisted of two layers for x&y views, and each layer consisted of 48 scintillating fibers.

3.1.3 CsI calorimeter

We stacked 12 × 12 small crystals to build a calorimeter with the size of 30 cm × 30 cm in xy-plane and 50 cm long. The size was determined to contain full electromagnetic showers from e^+s. Each crystal was viewed by a R5364 PMT with a CW-base through a 4.6 mm thick silicone cookie and a UV transmitting filter. Signals from each crystal were recorded by the 125 MHz FADC, and 48 sampling points were recorded for every trigger. All these components are the ones that are used at the KOTO experiment described in Section 2.2.1.

The CsI array and the PMTs were placed in a dark box to keep them in dark and in a stable temperature, as shown in Fig. 3.4. To change the incident angle and position of e^+ beam, the box was fixed on a turntable, and the turntable was mounted on an X-stage. Because the light output of a CsI crystal depends on its temperature, and the surface of a CsI crystal is easily damaged by humidity, temperature and humidity in the dry room were controlled. The temperature and humidity in the box and the dry room were monitored as shown in Fig. 3.5. The temperature at the the upstream surface of the CsI crystal was stable within 1 °C during the data taking. It was important because most of the light from the e^+ showers were emitted near the upstream surface of the CsI crystal. The relative humidity in the dry room was mostly kept below 20 %.

The gain of each PMT was also monitored by an LED flasher system. Figure 3.6 shows a schematic view of the LED flasher gain monitoring system. Basic idea of the system is the same as the laser calibration system for the KOTO experiment. An LED which emits a light of 375 nm in wavelength was fixed at one end of a small tube. On the other end of the tube, a PIN photodiode and 144 quartz fibers were placed. The LED flashed at 1 Hz, and its output was monitored with the PIN photodiode. The other end of each fiber was attached on the downstream surface of a crystal to distribute the light from the LED. By tracking the PMT mean output normalized by the PIN photodiode output periodically, we monitored the gain of each PMT. The LED output was stable within 1 %. The details on the PMT gain correction will be described in Section 3.3.1.

We also prepared trigger counters to take cosmic ray events for the energy calibration. Figure 3.7 shows the the location of the trigger counters. The counters consist of four plastic scintillators with the size of $35 \times 1 \times 6$ cm^3 each. We attached two PMTs on left and right-hand sides of each scintillator. Two of the four scintillators were placed 157 mm above the top surface of the CsI array, and the rest of the two scintillators were placed 248 mm below the bottom surface of the CsI array. Both scintillators were placed about 125 mm downstream of the upstream surface of the CsI array.

3.1.4 Data acquisition system

We took data in a similar way as the KOTO experiment. Figure 3.8 shows an overview of the DAQ system for the beam test. Signals from each PMT were recorded by the 125MHz FADC boards and stored temporally for 4 μs. The FADC board recording outputs of the central 16 crystals calculated the local sum of the 16 channels and sent the sum to a L1 trigger board every 8 ns via an optical fiber. The L1 trigger board compared the sum with a given threshold and made a trigger signal. When the CAMAC system for the position detector was busy, the system sent a busy signal to the L1 trigger board and the trigger signal was blocked by the busy signal. If not, the trigger signal was sent to the fanout board via VME 9U backplane. The trigger and a 125MHz clock signals were distributed to each FADC board. When a FADC board received a trigger, the board sent the corresponding waveform data to a L2 trigger/readout board via

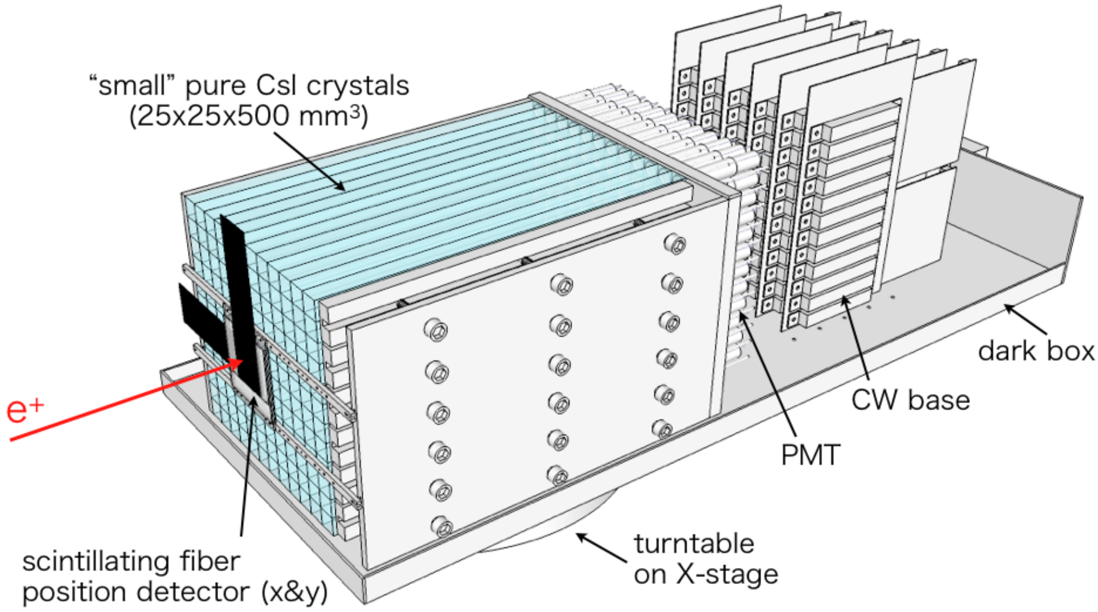

Figure 3.4: The CsI calorimeter used for the beam test and the dark box on the turntable. The cover of the dark box is not shown in this figure.

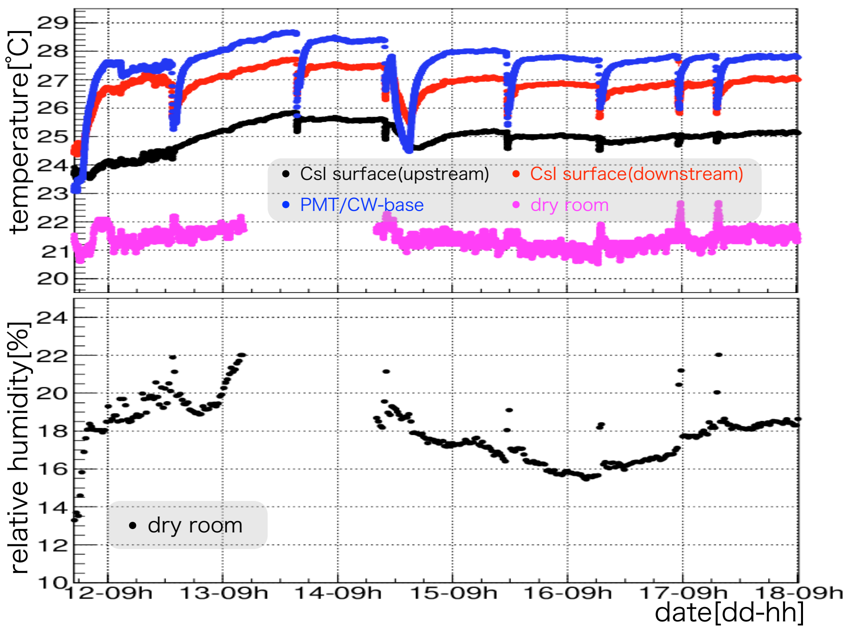

Figure 3.5: Temperature(top) and humidity(bottom) in the dry room and the dark box. The dots in the top figure show the temperature at the upstream(black) and downstream(red) surface of the CsI array, around the PMTs/CW-bases(blue) and in the dry room(magenta). The black dots in the bottom figure show the relative humidity in the dry room.

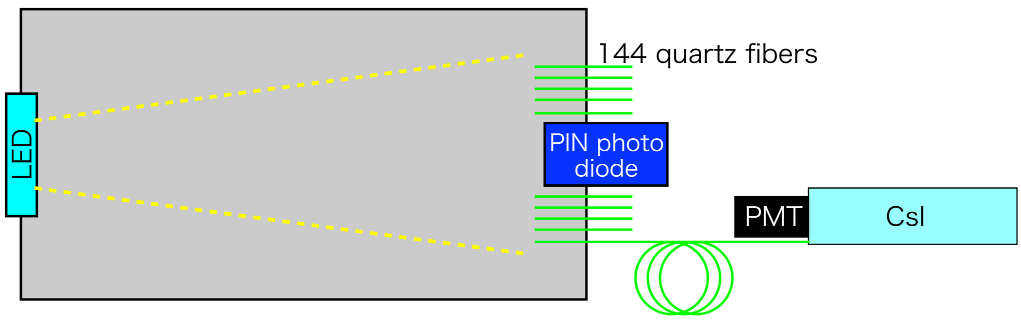

Figure 3.6: A schematic view of the LED flasher system to monitor the gain of each PMT. The LED output was monitored with a PIN photodiode. The light from the LED was distributed to each crystal through a quartz fiber.

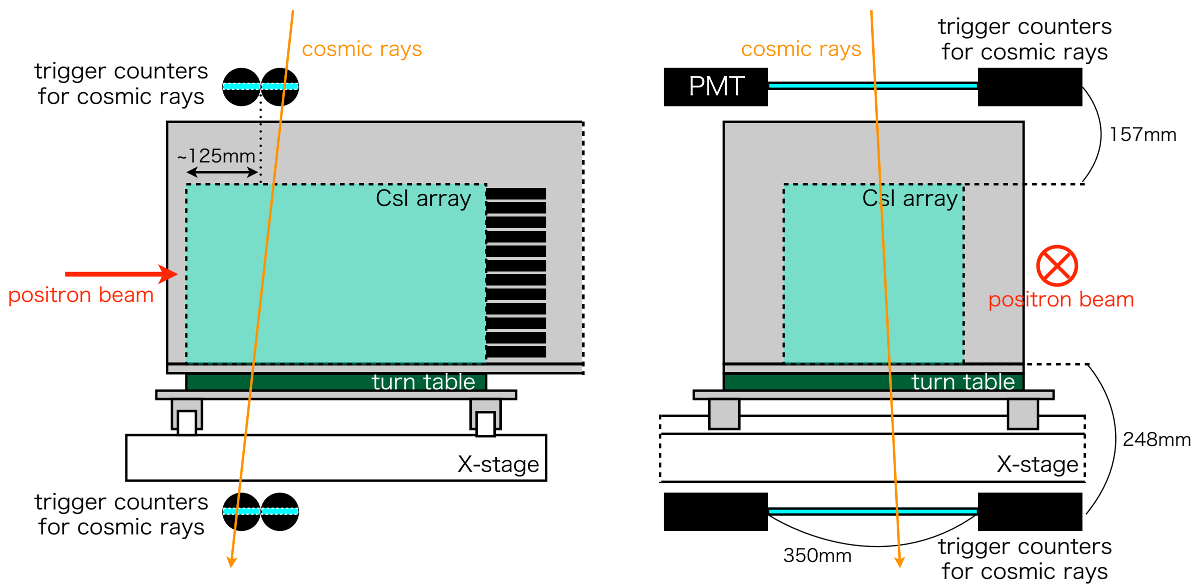

Figure 3.7: The location of the trigger counters for cosmic rays. Figure on the left(right) shows the side(front) view of the setup.

an optical fiber. At the beam test, the L2 board was read out via VME backplane without any selections.

The energy threshold for the trigger was about 45 MeV, and the DAQ rate was 300-500 Hz limited by the synchronization between the VME and CAMAC system, and the speed of event-by-event-readout.

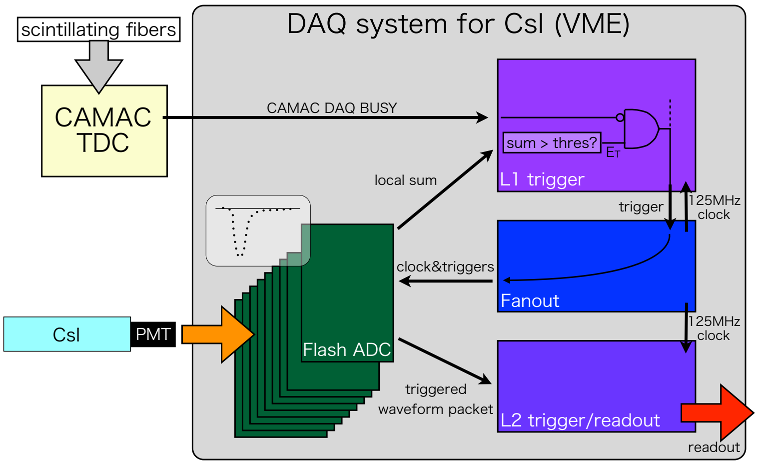

Figure 3.8: An overview of the DAQ system for the beam test.

3.1.5 Run

We took data for various combinations of energies and incident angles. The e^+ energy was set at $\{100, 200, 300, 460, 600, 800\}$ MeV, and the incident angle was set at $\{0°, 10°, 15°, 20°, 30°, 40°\}$. We will write a combination of the energy and incident angle as (800 MeV, 40°). We took 30k events for each run, and made 10 runs for each (E, θ). The position of the CsI array on the X-stage was adjusted for every combinations to contain the full shower. The position of the scintillating fiber detector was also adjusted to detect the incident positions of e^+s.

We also had two kinds of special runs. One of them was a special run for measuring the timing resolution. A light-rich scintillator was placed upstream of the CsI array to define the timing of each event. We attached two PMTs on left- and right-hand sides of the scintillator. Signals from the PMTs were recorded by a 500MHz FADC developed for the KOTO experiment. The 500MHz FADC used a common 125MHz clock which was synchronized to other 125MHz FADCs. We set the e^+ incident angle at 0° and took 30k events for each energy. The obtained timing resolution will be described in Section 3.6.

The other special run was for energy calibration with beam. In the normal runs, almost all the deposit energy was contained in the central crystals in the CsI array. If we only use such data for energy calibration, the obtained calibration constants might be biased. To suppress biassing, we changed the beam incident position along the x-axis. In this special run, crystals next to the both sides of the central crystals contained more energy. We took data at (600 MeV, 0°) for this special calibration run. The energy calibration with beam data will be described in Section 3.4.

We also took some cosmic ray data for energy calibration during night. The LED events for the gain monitoring were recorded while taking beam and cosmic ray data.

3.2 Pulse shape analysis

The waveform readout, and the usage of the Bessel filter were new attempts for us to take data. We thus first studied the pulse shape itself.

In the following subsections, we describe an error on each sampling point, and how to fit the pulse shapes.

3.2.1 Error on each point

We studied an error on each sampling point. We first assumed that an error on each sampling point is represented by the amount of ground noise alone. To evaluate the validity of this assumption, we fit the pulse shape with an "Asymmetric Gaussian":

$$\begin{aligned} A(t) &= |A| \text{ Gaussian}(t, \mu, \sigma) \\ \textit{where} \quad \sigma(t) &= a\ (t-\mu)^4 + b\ (t-\mu)^3 + c\ (t-\mu)^2 + d\ (t-\mu) + \sigma_0\ . \end{aligned} \tag{3.1}$$

We fitted the pulses in range -150 ns $< t - t_{\text{peak}} <$ 45 ns, where t_{peak} is the peak timing. Details of the fitting procedure are described in the next subsection. Figure 3.9 shows the correlation between the fitted pulse height and the reduced χ^2 of the fitting. The mean χ^2 value for the pulse heights below 4000 counts is centered at 1, showing that the assumed error is appropriate. The behavior of the χ^2 for the pulse heights larger than 4000 counts will be explained in Section 3.3.3.

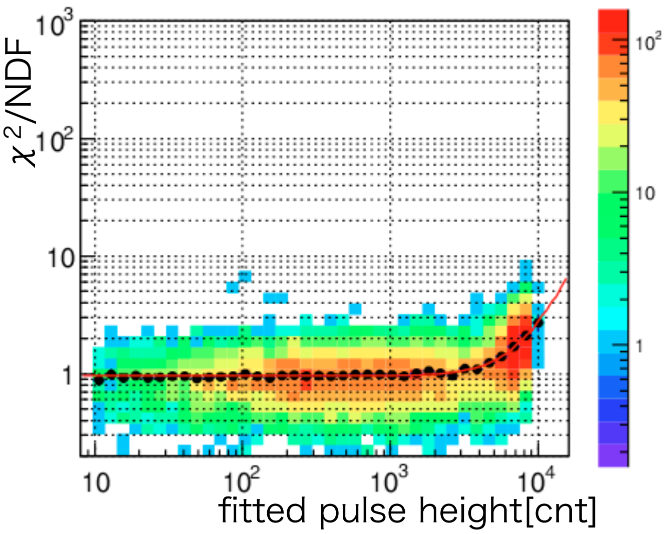

Figure 3.9: Correlation between the fitted pulse height and the reduced χ^2 of the fitting. Pulse shapes were fitted with the Asymmetric Gaussian shown in Equation 3.1. An error on each sampling point was set at the amount of the ground noise. The red line shows a fitting function of the correlation just for a study.

3.2.2 Fitting

We fitted pulse shapes to reconstruct energy and timing of incoming e^+s. There were following two requirements for the fitting.

1. The pulse shape can slightly depend on its pulse height, and also depend on its readout channel.

2. The shape to be used for fitting should be fixed to the shape depending on its pulse height and its readout channel.

We set the first requirement, because we found that the pulse shape slightly depends on the pulse height. Figure 3.10 shows the normalized pulse shapes for different pulse height ranges. The pulse shape in the tail region varies with the pulse height. We also found that pulse shapes depend on channels as shown in Fig. 3.11. Pulse shapes are different between channels at their tail parts, in particular, even for the same pulse height range. A few channels have totally different tail shapes.

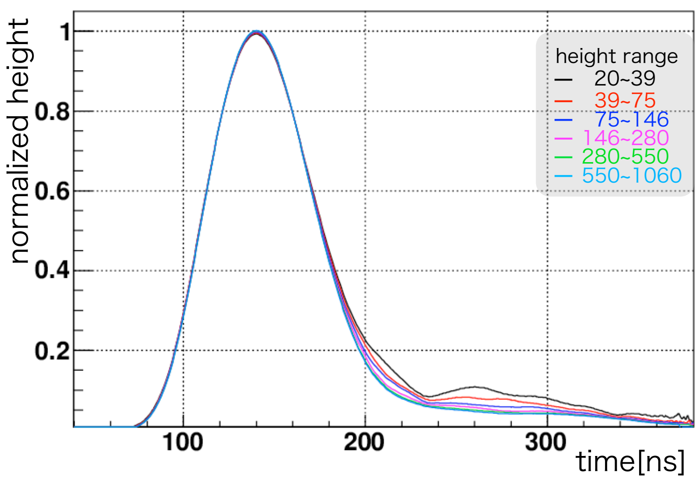

Figure 3.10: The pulse shapes of one channel for different pulse height ranges. The pulse heights are normalized to 1. The pulse shape in the tail region varies with the pulse height.

We set the second requirement, because we found that we can achieve a better performance by fixing the shape parameters. Figure 3.12 shows the timing difference between two selected crystals. The pulse shapes were fitted by using the Asymmetric Gaussian shown in Equation 3.1. We achieved a better timing resolution on fitting the pulse shapes with fixed shape parameters (except pulse height and timing).

We tried various functions[1] to fit the pulse shapes. It was, however, difficult to parameterize pulse shapes properly for every channel and wide pulse height ranges. At the end, we decided to use templates of pulse shapes to fit them.

The templates were made from pulse shapes in real data, and they were prepared for each channel and multiple pulse height ranges. They reproduce pulse shapes in detail even at the tail part and are suitable to be used for fitting. The good reproduction in the tail region also

[1] Appendix A

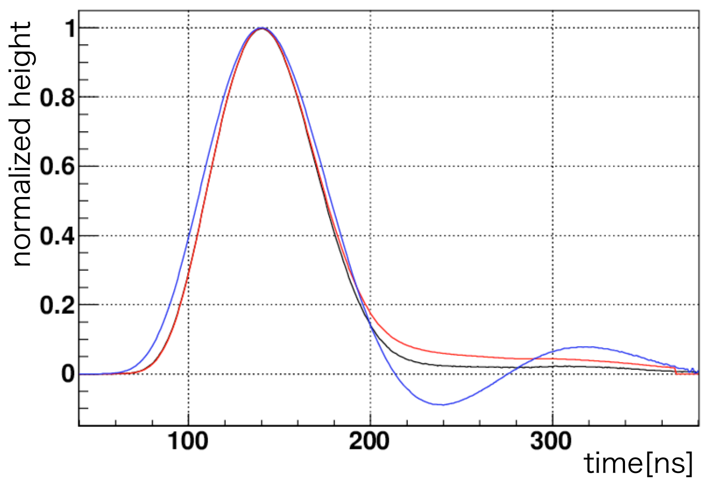

Figure 3.11: The pulse shapes of different channels for one pulse height range. Pulse shapes are different between channels at their tail parts, in particular. A few channels have totally different tail shapes.

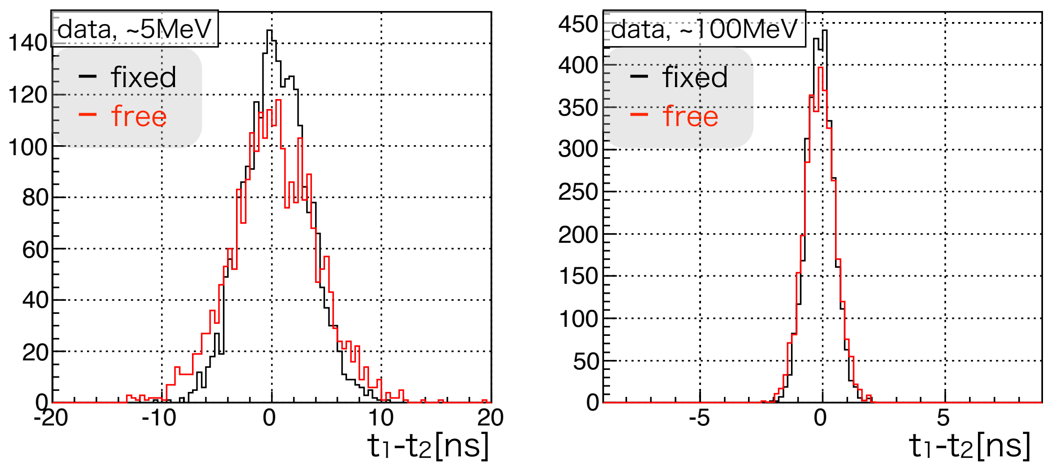

Figure 3.12: The distribution of the timing difference between two selected crystals for around 5 MeV(left) and 100 MeV(right). When fitting the pulse shapes, the fitting parameters except pulse height and timing were fixed for the black histogram, and floated for the red histogram.

helps to separate overlapped pulses. The performance of overlapped pulse separation will be discussed in Section 5.4.

The templates were made in the following way.

1. Fit the Asymmetric Gaussian to pulse shapes.
2. Normalize the pulse shape by the fitted pulse height, and shift the pulse shape in time to align the peak timing.
3. Average the normalized pulse shapes for every channel and every pulse height range.

The pulse height range was divided logarithmically into 10 sections {20, 39, 75, 146, ..., 4000, 6500, 10000}. Because the time difference from the peak timing to the closest sampling point after the peak is uniform within 8 ns (125 MHz), we can know the mean height for a finer span than 8 ns. The typical shape was sampled for every ns. The pulse shape between the sampled points was interpolated with a spline curve. The span, 1 ns, is fine enough compared to the width of pulses. Figure 3.10 and 3.11 show exmaples of the templates. Figure 3.13 shows the correlation between the fitted pulse height and the reduced χ^2 of the fitting with the templates. The pulse height range is fine enough to resolve the pulse height dependence of the pulse shape. The behavior of the reduced χ^2 for the pulse heights larger than 4000 counts will be also explained in Section 3.3.3.

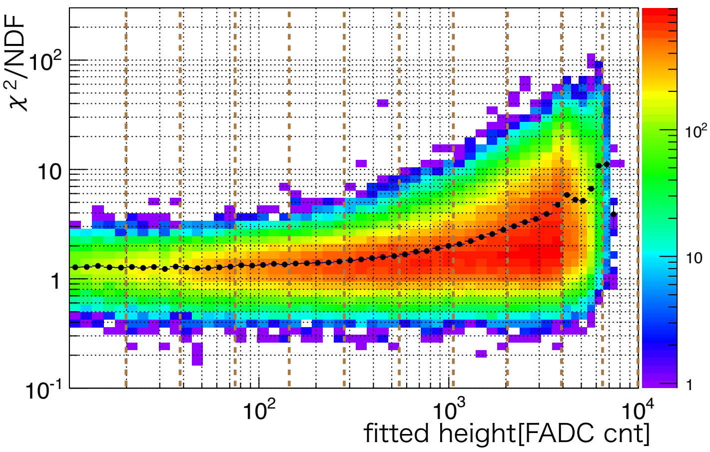

Figure 3.13: The correlation between the fitted pulse height and the reduced χ^2 of the template based fitting. The dashed brown lines show the boundaries of the pulse height ranges for the templates.

Here, we will describe the fitting procedure in detail. First, the pedestal was determined for every event by averaging the first 6 sampling points. If the time difference between the peak timing and the 6th sampling point was less than 58 ns, the last 6 of the 48 sampling points were used to decide the pedestal. Next, a rough pulse height and timing of the pulse were decided by scanning all the sampling points. If the pulse height was greater than 10 FADC counts ($\sim$ 0.5 MeV), the corresponding template was prepared for fitting based on the channel ID and the roughly decided pulse height. The pulse shape was fitted between -150 ns and 45 ns relative to the roughly decided peak timing. The pulse shape was fitted again using the fitted pulse height and timing to select another template and fitting range.

3.3 Energy calibration

In this section, we will describe the energy calibration procedure. In the following subsections, we will explain a correction for PMT gain drifts, an energy calibration with cosmic rays, and the energy non-linearity found in the beam test data.

3.3.1 Gain correction

We first corrected the PMT gains for their drifts during the run. As described in Section 3.1.3, we prepared the LED flasher system to monitor the drifts of PMT gains. The light output of the LED was monitored with a PIN photodiode. The same PIN diode is used for the laser calibration system for the KOTO experiment, and characteristics of the PIN diode had been studied. The PIN photodiode is a photosensor which can measure light outputs without an internal amplification. Because there is no gain fluctuation of the PIN photodiode, we can measure the LED light output reliably with the PIN photodiode. By tracking the ratio of the PMT mean output to the PIN photodiode output for the LED light pulses periodically, we can monitor and correct the gain of each PMT. The LED light output was stable within 0.5% during the data taking as shown in Fig. 3.14.

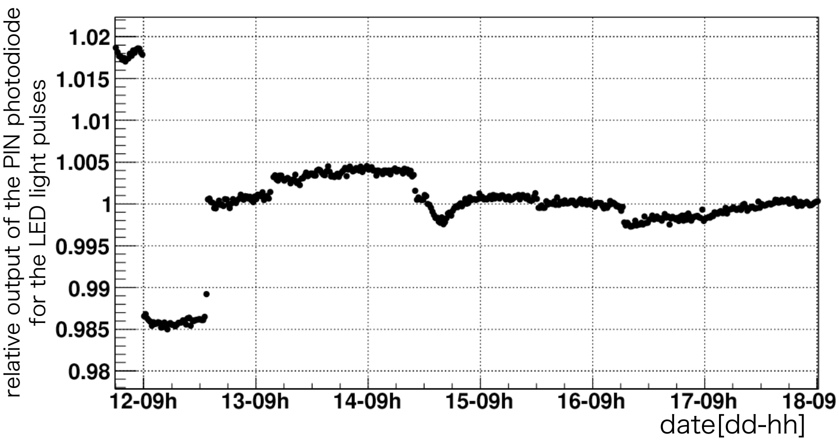

Figure 3.14: The relative output of the PIN photodiode for the LED light pulses used for PMT gain monitoring. The LED output was monitored by the PIN photodiode to be used at the KOTO experiment. We started our main data taking at 4/13 11:00 AM, and the LED output was stable within 0.5% after then.

We first checked the validity of using the LED flasher system for correcting the gains, with one PMT whose gain was unstable. Figure 3.15 shows the relative ratio of the PMT output to the PIN photodiode output for the LED light pulses. The ratio fluctuated up to $\sim$ 50 % along the time. Because the LED light output was stable (and normalized), the fluctuation was caused by the drift of the PMT gain. We divided the data taking time into multiple periods, and corrected the PMT gain for each period using the LED output. Figure 3.16 shows the pulse height distributions of cosmic ray events in two separated days with and without the PMT gain correction. With the PMT gain correction, the two pulse height distributions in different days became consistent with each other. This shows that the PMT gain correction works at least for $\sim$10-20 % deviations.

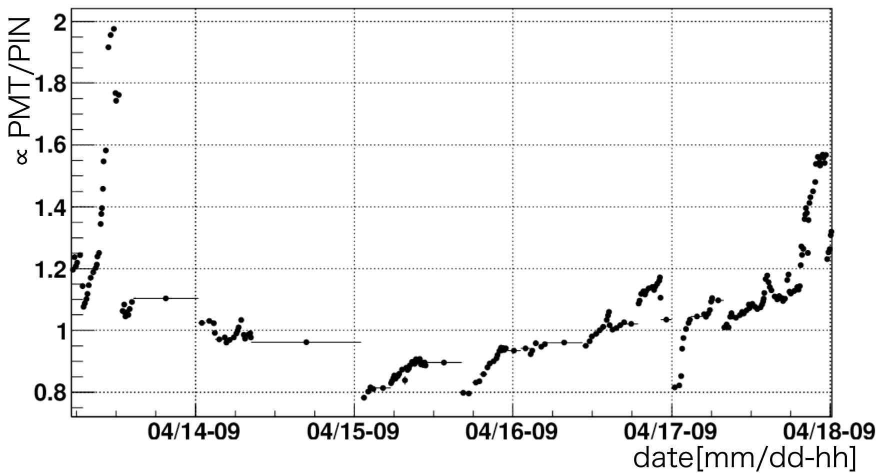

Figure 3.15: The relative ratio of the PMT output to the PIN photodiode output for the LED light pulses.

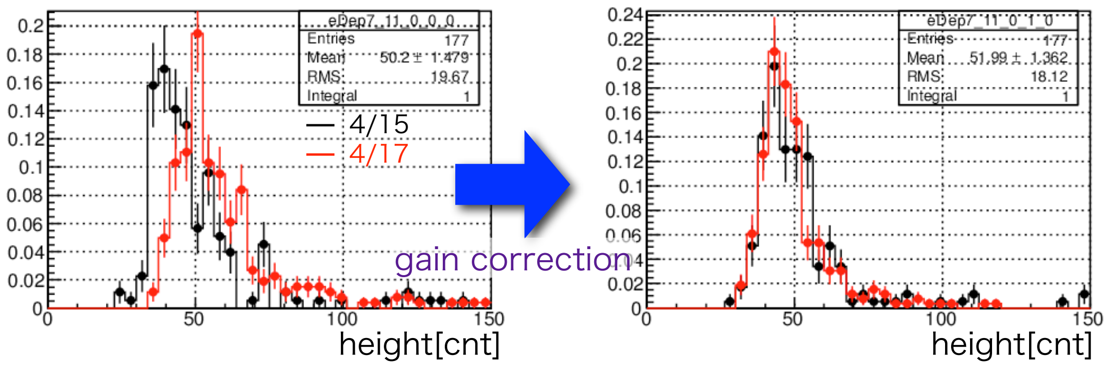

Figure 3.16: The pulse height distributions of cosmic ray events taken in two separate days with(right) and without(left) the PMT gain correction. The gain of this PMT was unstable according to the LED gain monitoring system.

The ratios of the outputs of the rest of the PMTs to the PIN photodiode output for the LED light pulses were much stable within a few %. Figure 3.17 show the relative ratios of the outputs of certain PMTs to the PIN photodiode for the LED light pulses. To check whether it is still valid to correct gains for such smaller deviations with the LED flasher system, we evaluated the PMT gain correction in the following two ways.

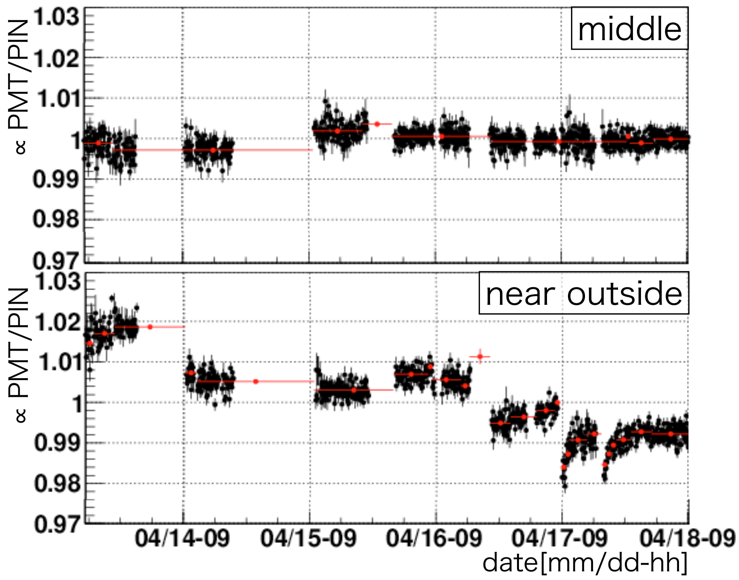

Figure 3.17: Typical gain histories of PMTs in the middle(top) and near outside(bottom) of the array monitored with the LED. The black dots show the relative ratios of the outputs of the PMTs to the PIN photodiode for the LED light pulses for each period, and the red dots show the averaged values over stable periods to be used for the gain correction. The outputs of most of the PMTs were stable within a few % during the data taking.

One way is to check the widths of the total energy distributions in the beam data. The energy calibration constant for each channel was temporally fixed to the value determined with the cosmic ray events in the last day. Figure 3.18 shows the widths of the energy distributions with and without the gain correction. Most of the widths became narrower with the PMT gain correction.

The other way is to compare the pulse height distributions of cosmic ray events between two separate days, with and without the PMT gain correction. We fitted the distributions of each channel to the Landau function, calculated the difference of the most probable values (MPV) of the function between the two days, and normalized the difference by the statistical error of the difference. Figure 3.19 shows the distribution of this value for each channel with and without the PMT gain correction. Ideally, the mean value should be 0, and the width of the distribution should be 1. Although it is still within the statistical errors, the gain correction moved the mean and width closer to the ideal values.

Based on the above two evaluations, we applied to PMT gain correction with the LED flasher system for the following data analysis. As was shown in Fig. 3.17, we used the correction factors averaged over stable periods.

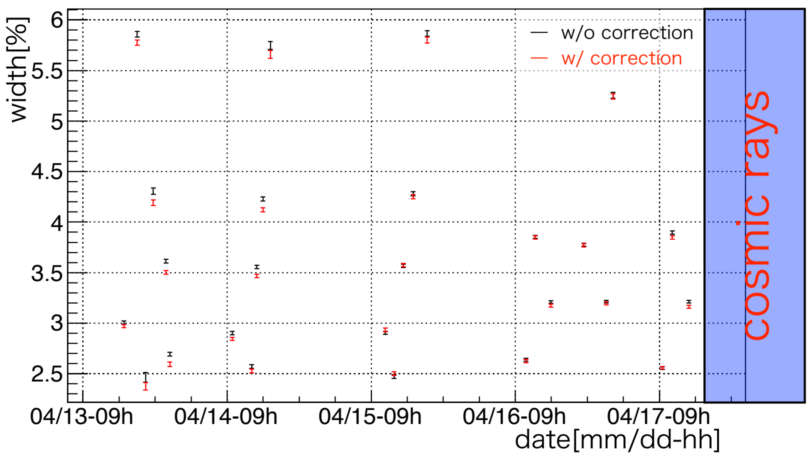

Figure 3.18: The widths of the energy distributions of all the beam data for each day. The black(red) dots correspond to the widths without(with) the gain correction. Energies were calibrated with cosmic ray events taken on the last day, 4/17. Assuming the gain drifts along the time, the gain correction should be more effective for the earlier dates. Most of the widths became narrower with the PMT gain correction.

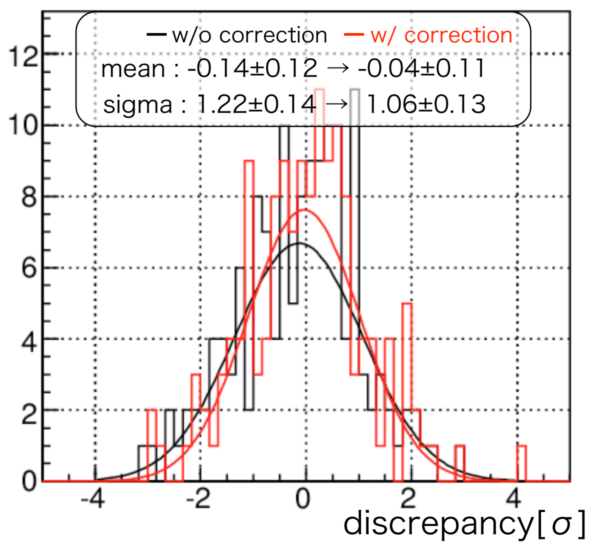

Figure 3.19: The differences of the most probable values of the pulse height distributions of cosmic ray events in separate two days normalized by the statistical error for each channel. The black(red) histogram shows the distribution without(with) the PMT gain correction. Although it is still within the statistical errors, the gain correction moved both the mean and width of the distribution closer to the ideal values, 0 and 1, respectively.

3.3.2 Calibration with cosmic rays

We calibrated energies with cosmic ray events. As was shown in Fig. 3.7, we prepared the trigger counters for cosmic rays. The expected energy distribution for each crystal was estimated with Monte-Carlo simulation. We fitted the Landau function to the distributions both for Monte-Carlo and data. According to the Monte-Carlo simulation, the most probable value of the Landau function was 13.7 MeV. We thus assigned the most probable value of data to be the 13.7 MeV.

3.3.3 Non-linearity

An energy non-linearity was found in data. Figure 3.20 shows the correlation between the maximum pulse height in all the crystals and the total energy for events in the (800 MeV, 0°) data. Figure 3.21 shows the same correlations for various beam energies. These plots indicate that the pulse heights for larger energy deposit are not linear to the energy deposit.

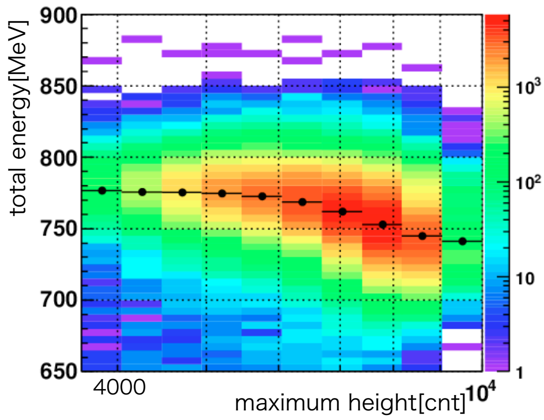

Figure 3.20: Correlation between the maximum pulse height in all the crystals and the total energy for events in the (800 MeV 0°) data. Black dots represent the mean total energies for different pulse height ranges.

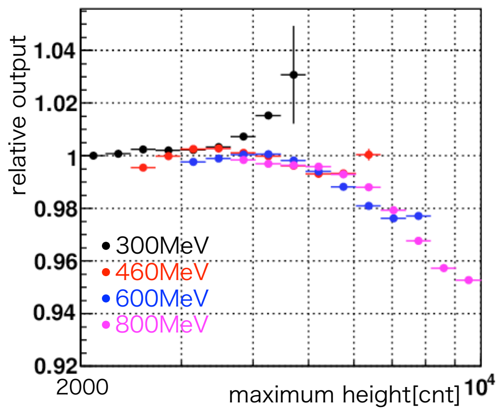

Figure 3.21: The maximum pulse height dependence of the total energy for various beam energies. The vertical scale of the smallest height range for 300 MeV data was adjusted to 1, and the vertical scale for the larger beam energy was adjusted to the smaller beam energy.

To confirm that there is a non-linearity, we did another measurement. Figure 3.22 shows a schematic view of the measurement. In this setup, typical pulse shape from the PMTs was generated by the function generator, and fed into the pre-amplifier in the CW-base. The signal from the pre-amplifier was recorded with the 125MHz FADC. We changed the output pulse height of the function generator, and took data for multiple pulse heights. Figure 3.23 shows the correlation between the observed pulse heights and the relative ratios of the observed charge to the height of the function generator output. This measurement also showed a non-linearity.

There are three amplifiers on the passage of signals before digitization, as was shown in Fig. 3.22. We suspect that some of these amplifiers introduced the non-linearity, but we have not identified which.

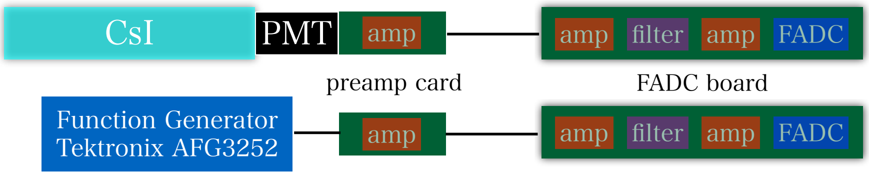

Figure 3.22: The setup to measure the non-linearity with a function generator (bottom). There are three amplifiers on the passage of signals before digitization.

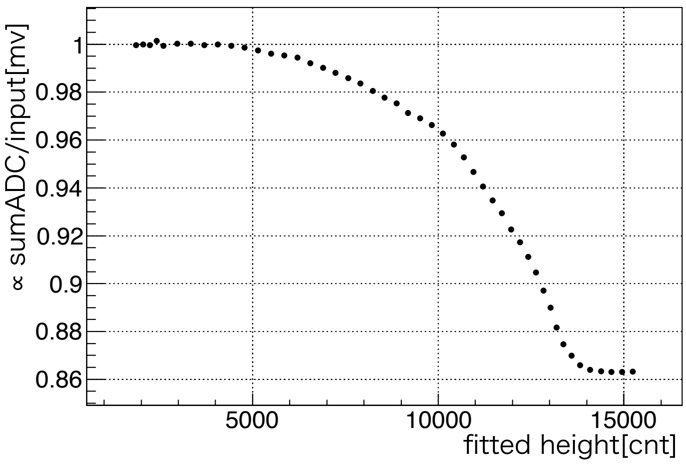

Figure 3.23: Correlation between the observed pulse height and the relative output. The relative output was the ratio of the observed charge to the height of the function generator output. A non-linearity is also observed.

Because the measurement with the function generator showed the non-linearity, we confirmed that the non-linearity exists in the beam test data. The non-linearity observed with the function generator emerges around 4000 FADC counts in pulse height, as shown in Fig. 3.23. The behavior of the reduced χ^2 for the pulse height larger than 4000 counts found in Fig. 3.9 in Section 3.2.1 is explained by the non-linearity. Because we suspect the non-linearity was caused by the saturation of some amplifiers, the output pulse shape from the amplifiers were deformed and expected to be saturated when the non-linearity occurred. This also gives an explanation for the behavior of the reduced χ^2 for the pulse heights larger than 4000 counts shown in Fig. 3.13. Because the templates were made based on the averaged pulse shape in each height range, the pulse shapes for relatively smaller or larger heights in a pulse height range are expected to be different from the template, and the reduced χ^2 for such pulses become larger.

3.4 Calibration with e^+ beam

The energy calibration should be done by taking the non-linearity into account. It means that the calibration constants should be energy dependent. The basic procedure is the following.

1. Determine a calibration constant for each channel with cosmic ray events (pulse height $\sim$ 240 FADC counts).

2. Using the beam data, correct the calibration constant in a larger pulse height region to treat the non-linearity. Correction factors were determined for different pulse height ranges.

3. Fit the correction factors with a proper function to inter-/extra-polate the correction factors.

The new calibration method treating the non-linearity was developed and tested with Monte-Carlo simulation.

In the following subsection, we first explain a χ^2 based energy calibration method for the case if there is no energy non-linearity. Next, we describe a new method to estimate the precision of the obtained calibration constants. We then extend the χ^2 based energy calibration method to take the energy non-linearity into account. Finally, we confirm the methods with the beam test data.

3.4.1 χ^2 based calibration method

First, we describe the calibration method for the case if there is no energy non-linearity. It means there is only one energy calibration constant for each channel to cover the entire energy range. A total deposit energy for an event, E_{tot}, can be represented by the following formula:

$$E_{\text{tot}} = \sum_{i}^{\text{ch}} C_i e_i \tag{3.2}$$

where e_i is the energy deposit calibrated with cosmic rays in the i-th channel, and C_i is a correction factor for the i-th channel. We can define χ^2 as:

$$\chi^2 = \sum_{j}^{\text{evnt}} \left(\frac{E_{\text{beam}} - \sum_i^{\text{ch}} C_i e_{ji}}{\sigma} \right)^2 \tag{3.3}$$

where E_{beam} is the mean beam energy, and e_{ji} is the energy deposit in the i-th channel of the j-th event, calibrated with cosmic rays. Because the error, σ, is independent of events, we set $\sigma = 1$. The correction factor, C_i, was tuned to minimize the χ^2 value. We checked the performance of this method with Monte-Carlo events. We varied the deposit energies in each channel with a fixed ratio within ± 8 %, and corrected those energies to minimize the χ^2. Figure 3.24 shows the distributions of the reconstructed total energy for 600 MeV e^+ samples before and after the calibration. This study shows that the method works.

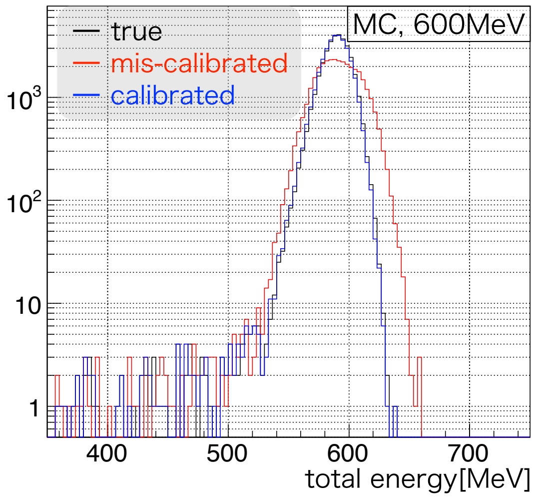

Figure 3.24: Performance check of the χ^2 based calibration method. We varied the deposit energies in each channel with a fixed ratio within ±8 %, and corrected those energies to minimize the χ^2 in Equation 3.3. The black histogram shows Monte-Carlo true distribution of the reconstructed total energy, the red histogram shows the distribution with varied energies, and the blue histogram shows the distribution with energies calibrated by the method.

3.4.2 Method to estimate the precision of the calibration constants

If we use the beam data for energy calibration, the precision of the calibration constant for each channel depends on the crystal, because the beam did not hit the CsI array uniformly, and the mean deposit energy for each crystal was different. The constants for outer crystals obtained with the beam is less precise than the constants obtained with cosmic rays due to poor statistics. The precision depends on the shower shape and the beam shape of e^+s. We chose the calibration constants between the two methods with the following method.

We developed a new method to estimate the precision of the calibration constants based on the beam test data, and tested the method with Monte-Carlo simulation. A calibration constant is represented in Equation 3.2. Summing energies over all the events, the previous formula can be represented by the following formula:

$$\begin{aligned} NE_{\text{beam}} &\equiv \sum_{j}^{N} E_j^{\text{tot}} \\ &= \sum_i C_i \sum_j^N e_{ji} \\ &= N \sum_i C_i \bar{e}_i \ , \end{aligned} \tag{3.4}$$

where N is the number of events, and $\bar{e}_i$ is the mean deposit energy in the i-th channel. If we focus on C_j, Equation 3.4 can be turned into:

$$N\bar{e}_j C_j \;=\; N(E_{\text{beam}} - \sum_{i\neq j} C_i \bar{e}_i) \ . \tag{3.5}$$

If $\bar{e_j} \ll \sum_{i\neq j} \bar{e_i}$, then $\sum_{i\neq j} C_i\bar{e_i} \sim E_{\mathrm{tot}}$, and Equation 3.5 can be turned into:

$$N\bar{e_j}C_j \quad \sim \quad NE_{\mathrm{beam}} - \sum_k^N E_k^{\mathrm{tot}} \ . \tag{3.6}$$

The expected precision of the constant, σ_{C_j}, is then:

$$\begin{aligned} \sigma_{C_j} &\sim \frac{\sigma_{(\sum_k^N E_k^{\mathrm{tot}})}}{N\bar{e_j}} \\ &= \frac{\sqrt{N} \times \sigma_{E_{\mathrm{tot}}}}{N\bar{e_j}} \ , \end{aligned} \tag{3.7}$$

where $\sigma_{E_{\mathrm{tot}}}$ is the width of the total deposit energy distribution. If $\bar{e_j} \gg \sum_{i\neq j} \bar{e_i}$, then $N\bar{e_j} \sim \sum_k^N E_k^{\mathrm{tot}}$ and $\sum_{i\neq j} C_i\bar{e_i} \sim 0$, and Equation 3.5 can be turned into:

$$C_j \sum_k^N E_k^{\mathrm{tot}} \quad \sim \quad NE_{\mathrm{beam}} \ , \tag{3.8}$$

the expected precision of the constant, σ_{C_j}, is then:

$$\begin{aligned} \sigma_{C_j} &\sim NE_{\mathrm{beam}} \times \frac{\sigma_{(\sum_k^N E_k^{\mathrm{tot}})}}{\left(\sum_k^N E_k^{\mathrm{tot}}\right)^2} \\ &= \frac{NE_{\mathrm{beam}}}{\sum_k^N E_k^{\mathrm{tot}}} \times \frac{\sigma_{(\sum_k^N E_k^{\mathrm{tot}})}}{\sum_k^N E_k^{\mathrm{tot}}} \\ &\sim \frac{\sqrt{N} \times \sigma_{E_{\mathrm{tot}}}}{N\bar{e_j}} \ . \end{aligned} \tag{3.9}$$

The precision of the constant, σ_{C_j}, is therefore expected to be represented as:

$$\begin{aligned} \sigma_{C_j} &\sim \frac{\sqrt{N} \times \sigma_{E_{\mathrm{tot}}}}{N\bar{e_j}} \\ &= \sigma_{E_{\mathrm{tot}}} \times \frac{1}{\bar{e_j}\sqrt{N}} \ . \end{aligned} \tag{3.10}$$

We checked the validity of this correlation. Figure 3.25 shows the correlation between the estimated precision by Equation 3.10 and the difference between the calculated and the true energy scales. The estimated precision was proportional to the difference observed. We can thus estimate the precision of calculated correction factors and select which correction factor to apply for each channel. Figure 3.26 shows an example of the selection of the correction factors based on the expected precision. Without any selection, constants for crystals outside the blue box were over-tuned. By using calibration constants based on the beam data only for the crystals whose estimated precision of the constant is less than 2 %, constants for all the crystals were tuned properly.

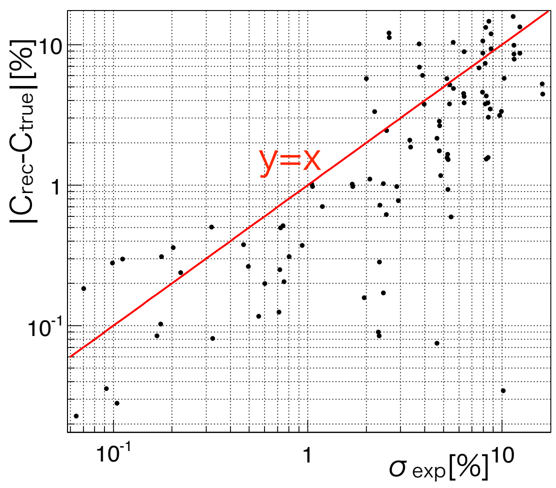

Figure 3.25: Correlation between the estimated precision by Equation 3.10 and the difference between calculated and true energy scales.

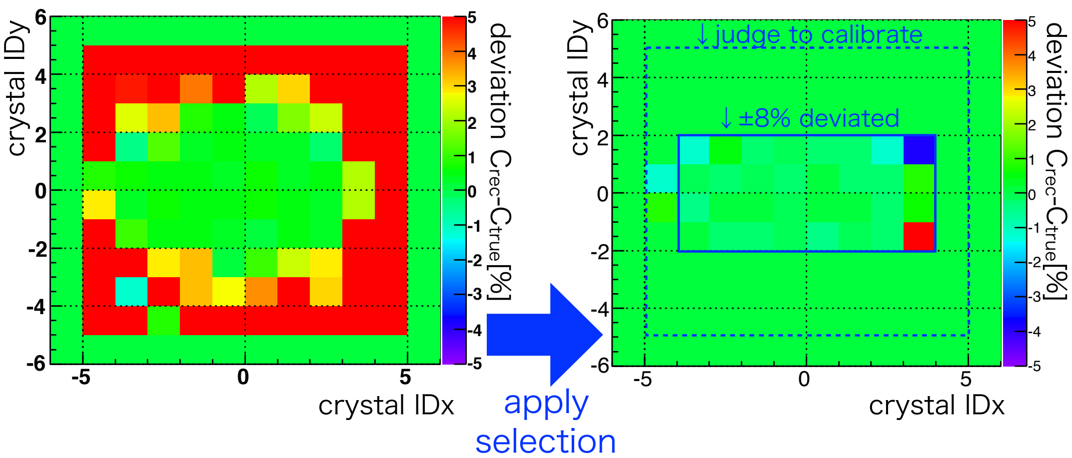

Figure 3.26: An example of applying selection of the correction factors based on the estimated precision by Equation 3.10 on calibration. The vertical(horizontal) axes show the geometrical ID of crystals in $x(y)$, and z-axes show the difference between calculated and true energy scales. Figure on the left(right) shows the obtained result without(with) selection of the correction factors. We applied the correction factors based on the beam data for the crystals whose estimated precision is less than 2 %.

3.4.3 Extension for treating non-linearity

The χ^2 based energy calibration method was extended to take the non-linearity into account. Because the non-linearity emerges if the pulse height is larger than about 4000 FADC counts as shown in Fig. 3.21, we assumed that the pulse heights below 3000 counts were linear to the incident energies. The pulse height region was divided logarithmically into 12 sections between 3000 and 8000 counts. A constant for the pulse heights below 3000 counts was also prepared. We then decided those constants in the following way.

1. Decide constants for the smallest pulse height range with the events whose maximum pulse heights are less than 3000 counts. The χ^2 is represented as:

$$\chi^2 = \sum_j^{\mathrm{evnt}:h_{\mathrm{Max}}\leq h_0} (E_{\mathrm{beam}} - \sum_i^{\mathrm{ch}} C_{0i}e_{ji})^2 \ , \tag{3.11}$$

   where h_{Max} is the maximum pulse height in all the crystals in an event, h_k is the upper boundary of the k-th pulse height range ($h_0 = 3000$), and C_{ki} is a correction factor for the k-th pulse height range of the i-th channel. The correction factors, C_{0i}, were determined to minimize the χ^2 value.

2. Decide constants for the next pulse height range (C_{1i}) with the events whose maximum pulse heights are less than h_1 and larger than h_0 in the same manner. The χ^2 is represented by the following formula:

$$\begin{aligned}\chi^2 &= \sum_j^{\mathrm{evnt}:h_{\mathrm{Max}}\leq h_1} (E_{\mathrm{beam}} - \sum_i^{\mathrm{ch}:h\leq h_0} C_{0i}e_{ji} - \sum_i^{\mathrm{ch}:h_0<h\leq h_1} C_{1i}e_{ji})^2 \\ &= \sum_j^{\mathrm{evnt}:h_{\mathrm{Max}}\leq h_1} (E_j^{\mathrm{else}} - \sum_i^{\mathrm{ch}:h_0<h\leq h_1} C_{1i}e_{ji})^2 \ .\end{aligned} \tag{3.12}$$

   The correction factors, C_{1i}, were determined to minimize the χ^2 value.

3. Update constants for smaller ranges. Iterate this manner down to the smallest range (C_{0i}).

4. Iterate the manner (2 and 3) up to the maximum pulse height range. The correction factors are thus determined or updated in the following order: $C_{0i} \to C_{1i} \to C_{0i} \to C_{2i} \to C_{1i} \to C_{0i} \to \ldots$.

We tested the extended method with Monte-Carlo simulation. Figure 3.27 shows the obtained correction factor for each pulse height range. Basically it worked, but the obtained correction factors for larger pulse height ranges tend to be slightly larger than the true values.

This effect was caused by the finite dependence of the total energy deposit upon the energy deposit in one channel whose ratio to the total energy deposit is large. Let us think about a simple case in which all the deposit energies are contained in only two crystals, c_1 and c_2, and mostly contained in c_1. Even if the energy in c_2 fluctuates (by photon statistics, for example), its effect on the measured total energy deposit is negligible. On the other hand, if the energy in c_1 fluctuates, it directly affects the total energy deposit. This is also the case in which all the deposit energies are contained in multiple crystals. The total energy deposit is generally affected by the energy fluctuation of a crystal whose energy fraction to the total energy deposit is large.

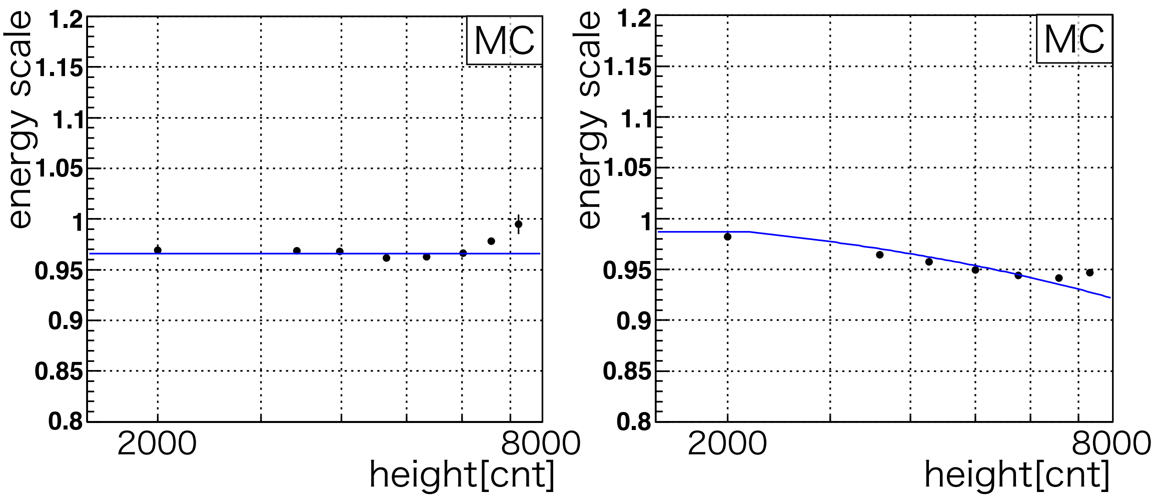

Figure 3.27: Examples of correction factor for each pulse height range obtained with the extended method. The black dots shows calculated correction factors for different pulse height ranges, and the blue line shows the true pulse height dependence. Figure on the left(right) shows the case which the constants are independent(dependent) of the pulse height. The obtained values for larger pulse height ranges tend to be slightly larger than the true values.

Figure 3.28 shows the correlation between a deposit energy for each crystal and the total deposit energy of the event. Total deposit energy has some dependence if a single crystal contains most of the beam energy. According to a Monte-Carlo study, the dependence is almost determined by the energy resolution such as photon statistics. Because we are calibrating energies to obtain the energy resolution itself, the dependence should be thus estimated from data. We also found that the dependence for higher beam energy can be estimated from lower beam energy data. The dependence in 600 MeV data looks similar to the one in 460 MeV data when we normalize the deposit energy of each crystal by the beam energy, as shown in Fig. 3.29. Because we assume that smaller pulse height is linear to its incident energy, the dependence for lower beam energy can be obtained. With the obtained dependence, we corrected E_{beam} in Equation 3.12 as a function of h_{Max} in the calibration. We call it "smearing correction". As shown in Fig. 3.30, the deviation of the energy scale for larger pulse height was resolved with the correction. Figure 3.31 shows the difference between the calculated correction factors, C_i, with the "smearing correction" and Monte-Carlo true values for various pulse heights.

3.4.4 Confirmation with data

We also confirmed these developed calibration methods with data. As described in Section 3.1.5, we took some data dedicated to energy calibration. In addition to the data, 3 runs for each pair of (600 MeV, 30°), (600 MeV, 40°) and (800 MeV, 40°) were used for energy calibration.

Figure 3.32 shows the total energy deposit obtained with calibration constants made with cosmic ray events and with the χ^2-based correction. Figure 3.33 shows the total energy deposit calculated with and without the "smearing correction". The fact that the distributions becomes narrower with the corrections shows that these χ^2-based and smearing corrections work correctly.

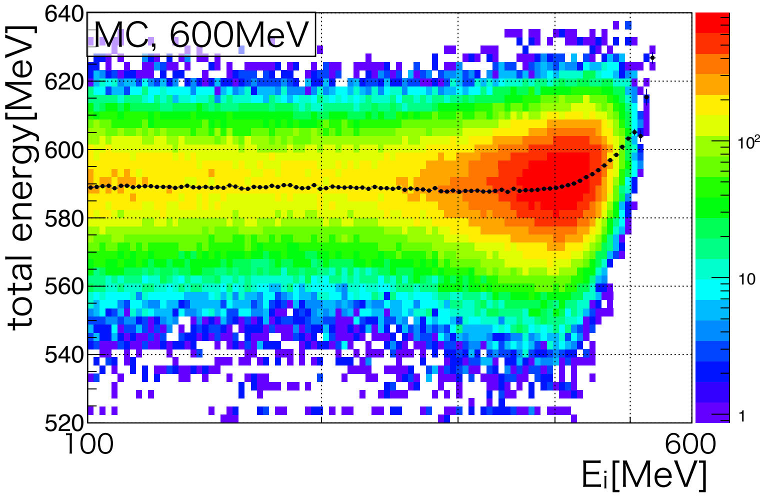

Figure 3.28: Correlation between a deposit energy in each crystal and the total deposit energy of the event. The black dots show the mean total energy for deposit energies in crystals. Total energy has some dependence when a crystal contains most of the beam energy.

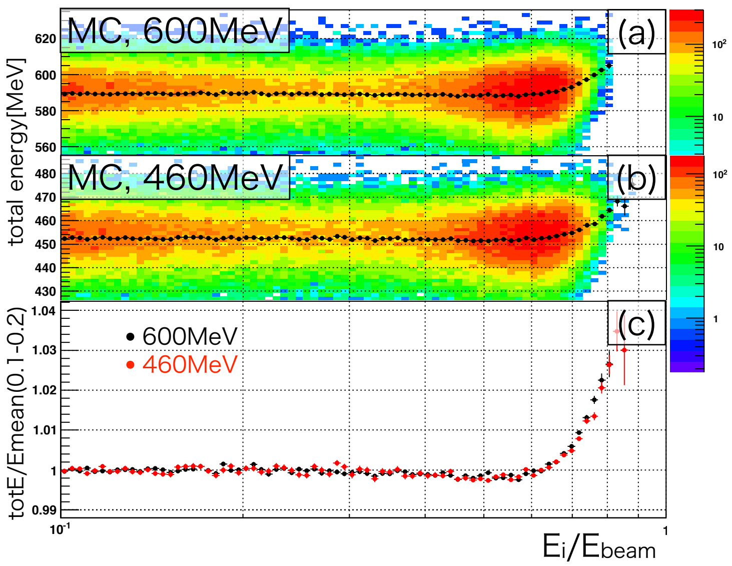

Figure 3.29: Correlation between a deposit energy in each crystal and the total deposit energy of the event for a) 600MeV and b) 460MeV data. c) Those dependences are similar if we normalize the deposit energy of each crystal by the beam energy.

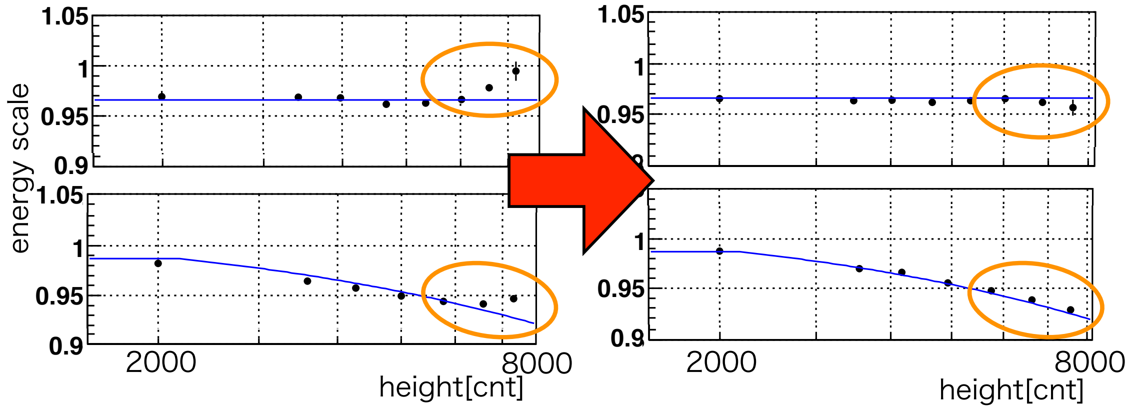

Figure 3.30: Obtained correction factor versus pulse height range, with(right) and without(left) the "smearing correction". The black dots show correction factors for different pulse height ranges and the blue line shows the true pulse height dependence. Figures on the top(bottom) show the case which the constants are independent(dependent) of the pulse height. The smearing correction works in large pulse height ranges.

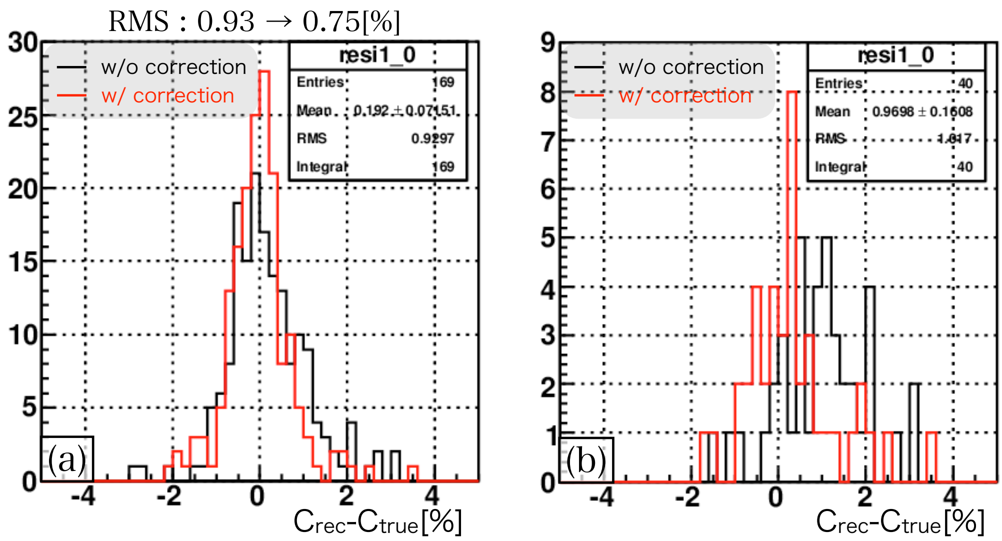

Figure 3.31: The difference between the calculated correction factors and Monte-Carlo true values for various pulse height ranges. The black(red) line shows the difference without(with) the smearing correction for a) all the pulse height ranges, and b) large pulse height ranges (> 6000).

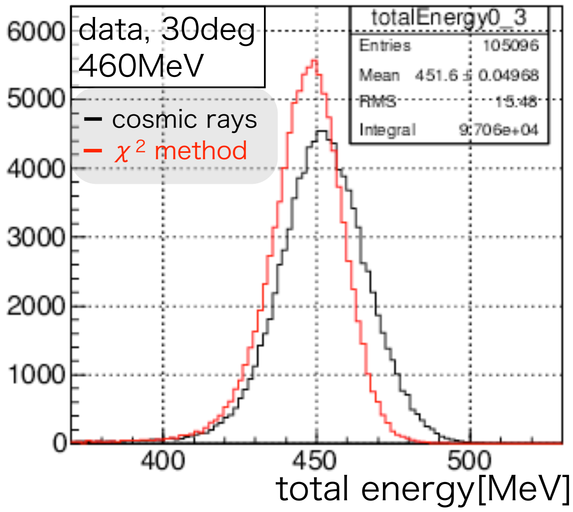

Figure 3.32: The distributions of total energy deposit for (460 MeV, 30°) e^+s. The black histogram was made with constants obtained with cosmic rays, and the red histogram was made with constants obtained with the χ^2-based method.

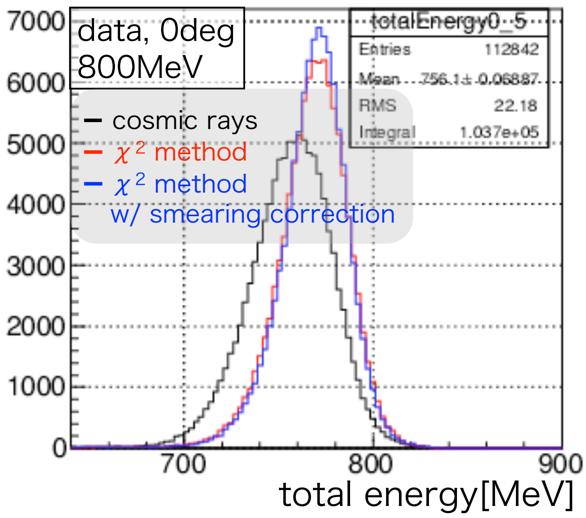

Figure 3.33: The distributions of total energy deposit for (800 MeV, 0°) e^+s. The black histogram was made with constants obtained with cosmic rays, and the red(blue) histogram was made with constants obtained with the χ^2-based method without(with) the smearing correction.

To inter-/extra-polate the obtained constants, the constants were fitted with a proper function:

$$C(h) = \left\{ \begin{array}{ll} C_0 & (h \leqslant h_0) \\ C_0 + a(h - h_0)^b & (h > h_0) \end{array} \right\}, \tag{3.13}$$

where h is the pulse height. The expression of the function was decided using the obtained result of the check measurement. Figure 3.34 shows the total energy deposit for 800 MeV e^+s with 0° incident angle, with and without the inter-/extra-polation function. Although the (800 MeV, 0°) data gives the largest deposit energy in one crystal in this beam test (up to 10000 counts in pulse height), we did not use the dataset for the energy calibration to confirm the validity of the calibration method. Even the correction factors for the largest height ranges were obtained by the extrapolation, the energy resolution for the dataset was improved. It indicates that the correction factors for other smaller pulse height ranges ($< 7000 - 8000$) obtained by these procedures were not over-tuned to the data used in the calibration, and the function is reasonable (Equation 3.13).

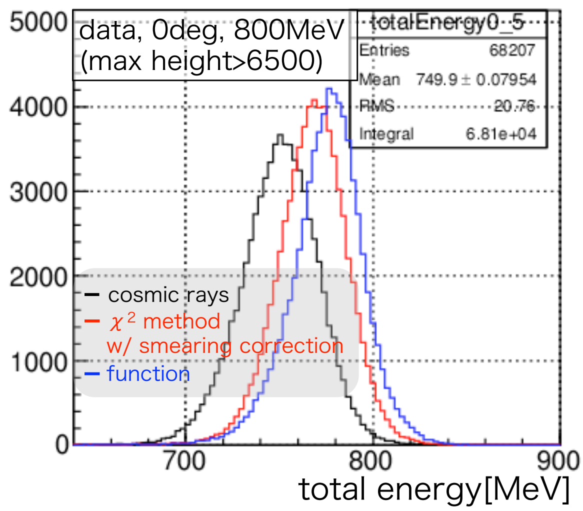

Figure 3.34: The energy distribution for (800 MeV, 0°) e^+s. Correction factors only for the pulse heights $< 7000 - 8000$ were determined by the calibration with beam data, and correction factors for the pulse heights $> 7000 - 8000$ were extrapolated by the function (Equation 3.13). To check the validity of the extrapolation by the function, the events in this plot were required to have the maximum pulse height larger than 6500 counts. The black histogram was made with constants obtained with cosmic rays, the red histogram was made with constants obtained with the χ^2-based method with the smearing correction, and the blue histogram was made with constants obtained with the inter-/extra-polation function made from the constants for the smaller pulse height ranges.

These are the procedures of the energy calibration with beam data. With the new calibration method with corrections, energy non-linearity was almost suppressed. If the e^+s hit the center of a crystal, the crystal contains a large fraction of the incident energy. Its visible energy suffers from the non-linearity, and the measured total energy deposit of those events becomes smaller.

Such effect is smaller for events in which e^+s hit the edge of a crystal. By suppressing the non-linearity, the hit position dependence of mean total energy should become smaller. Figure 3.35 shows the hit position dependences of the mean total energy for (600 MeV, 0 °) data, with and without the correction for the non-linearity. This also shows that the observed non-linearity is suppressed.

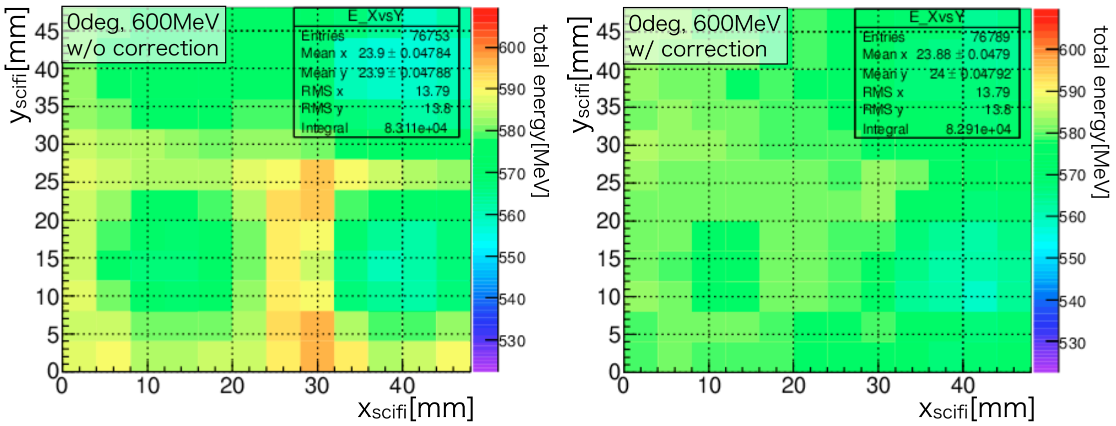

Figure 3.35: The hit position dependences of the mean total energy for (600 MeV, 0 °) data with(right) and without(left) the correction for the non-linearity.

We further checked the result with the temperature dependence of the CsI light yield. We selected a dataset in which the temperature deviation was relatively large. Figure 3.36 shows the temperature dependence of the total energy for (800 MeV, 40°) data. By fitting, we obtained the dependence: -0.93 ± 0.08 %/°C. It is consistent with the value -0.95 ± 0.03 %/°C, which was independently measured after the beam test[15].

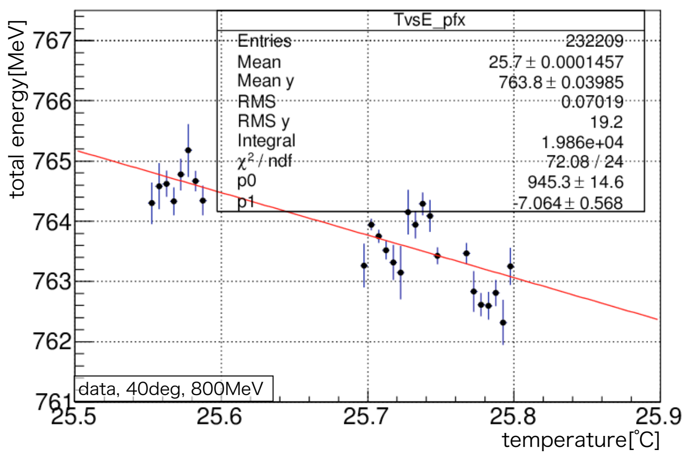

Figure 3.36: The temperature dependence of the total energy for (800 MeV, 40°) data. The fitted slope was -7.1 ± 0.6 MeV/°C, and it corresponds to -0.93 ± 0.08 %/°C.

3.5 Energy resolution

We next evaluated the energy resolution of the calorimeter. The energy in each crystal was calculated base on the pulse height.

There are two ways to calculate energy from the pulse shape recorded by FADC. One way is to calculate energy based on the pulse height, and the other way is to calculate energy based on the sum of the heights over 48 sampling points. We can expect to achieve better precision with the pulse height based method because of the following two reasons. One of them is that energies based on the pulse heights are less sensitive to the ground noise than energies based on the sums of the heights (SOH). The SOH is calculated with:

$$\begin{aligned} \mathrm{SOH} &\equiv \sum_i^N h_i \\ &= \sum_i^N d_i - N \times h_{\mathrm{GND}} \ , \end{aligned} \tag{3.14}$$

where i is an index of sampling point, N is the number of recorded samples (= 48), h_i is the height of the i-th sampling point, d_i is the recorded raw value of the i-th sampling point and h_{GND} is the pedestal constant used for the event. The error of the sum of heights caused by the ground noise is then:

$$\sigma_{\mathrm{SOH}} = N \times \sigma_{h_{\mathrm{GND}}} \ . \tag{3.15}$$

Because the value of the sum of heights is about 10 times of the fitted pulse height (h_{peak}), the ratio of the error to the value of the sum of heights, $\sigma_{\mathrm{SOH}}/\mathrm{SOH}$, is:

$$\frac{\sigma_{\mathrm{SOH}}}{\mathrm{SOH}} \sim \frac{N}{10} \times \frac{\sigma_{h_{\mathrm{GND}}}}{h_{\mathrm{peak}}} \ , \tag{3.16}$$

and it means energies based on the sums of heights are more sensitive to the ground noise than energies based on the pulse heights. The other reason is that energies based on the pulse heights are less sensitive to the peak timing within the 48 recorded samples. If the pulse comes later, some of its tail region can be out of recorded range. Energies based on the sums of heights can thus suffer from the timing.

On the other hand, we believe the mean value of the sums of the heights should represent their mean value of charge correctly. We then found that the pulse shape has a slight charge dependence as shown in Fig. 3.37. Therefore, we decided to use pulse heights to calculate energies with the correction of the charge dependence. Figure 3.38 shows the distributions of deposit energy based on the pulse height with a correction of the charge dependence, and the sum of heights. We can achieve better energy resolution with the pulse height based calculation.

Based on the energy calculation for each channel, we then checked the energy resolution of the calorimeter. We added energy deposits in crystals exceeding 0.6 MeV threshold to make total energy. Because the distributions of total energy are asymmetric, we first fitted the distributions with a lower order Asymmetric Gaussian:

$$\begin{aligned} A(E) &= |A| \ \mathrm{Gaussian}(E, \mu, \sigma) \\ where \quad \sigma(E) &= a\ (E - \mu) + \sigma_0 \ , \end{aligned} \tag{3.17}$$

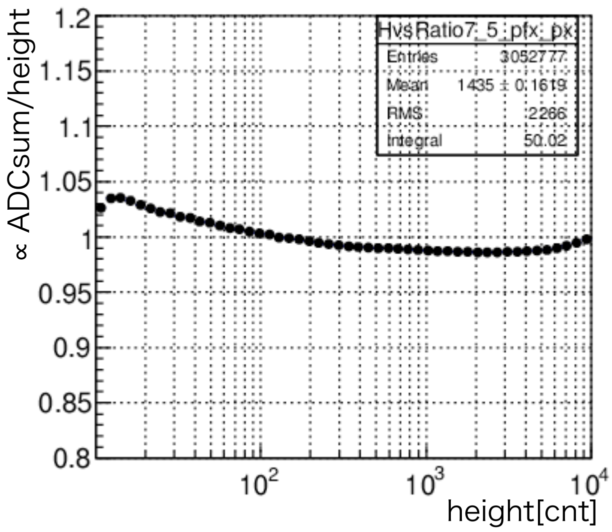

Figure 3.37: The ratio of the pulse height to the sum of heights is shown as a function of the pulse height.

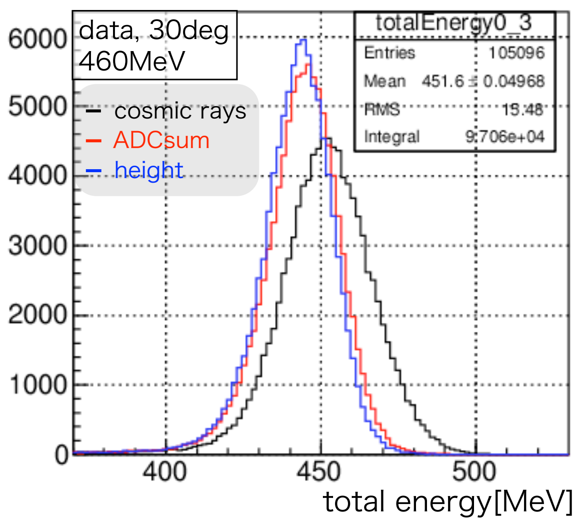

Figure 3.38: The distributions of deposit energy based on the pulse height(blue) and the sum of heights(red) for (460 MeV, 30°) data. The black line shows the distribution obtained with the constants by cosmic rays and the sum of heights based calculation just for the comparison.

a is an asymmetry parameter, and σ_0 is a typical width. We then defined energy resolution, σ_E/E, as σ_0/μ. Figure 3.39 shows the obtained energy resolution for various energies and incident angles. The re-calibration with beam improves the energy resolution. We checked the energy resolutions with and without an incident position cut. The incident position cut required a single hit on each layer of the scintillating fiber position detector, to suppress shower leakage. The energy resolution obtained with the cut, however, can suffer from an error of the calibration constant for a certain channel, because the incident position was limited within 4 crystals by applying the incident position cut. Nevertheless the energy resolution was almost independent of the incident position cut and incident angle. The obtained energy resolution was better than the designed value of the KOTO experiment.

We parametrized the obtained energy resolutions for the incident angle of 0° with the function:

$$\frac{\sigma_E}{E} = \frac{p_0}{\sqrt{E}} \oplus \frac{p_1}{E} \oplus p_2 \quad (E : \mathrm{GeV}). \tag{3.18}$$

To suppress the effect of the non-linearity, the data point for (800 MeV, 0°) was excluded from the fitting. As shown in Fig. 3.40, we obtained $p_0 = 1.26 \pm 0.03$ %, $p_1 = 0.13 \pm 0.03$ % and $p_2 = 0.76 \pm 0.09$ %.

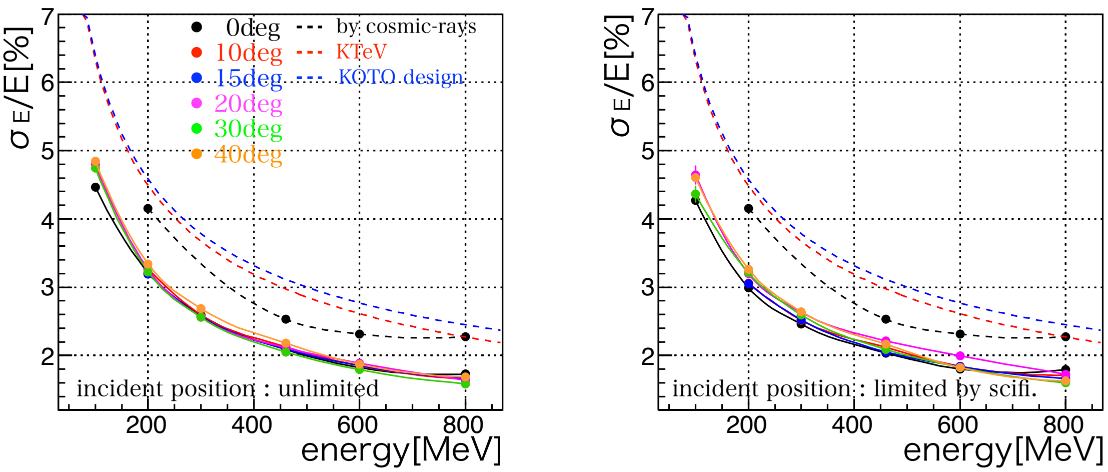

Figure 3.39: The obtained energy resolutions for various energies and incident angles. Incident position was not limited for the figure on the left, and limited by the scintillating fibers for the figure on the right. The black dashed lines are obtained with the calibration with cosmic rays, the red dashed lines are the function at KTeV experiment[16] (though they only used more than 3 GeV photons), the blue dashed lines show the designed value of the KOTO experiment.

3.6 Timing resolution

We also evaluated the timing resolution of each channel. Timing of each crystal was defined by the peak timing of the fitted pulse shape. We used two different methods to evaluate the timing resolution.

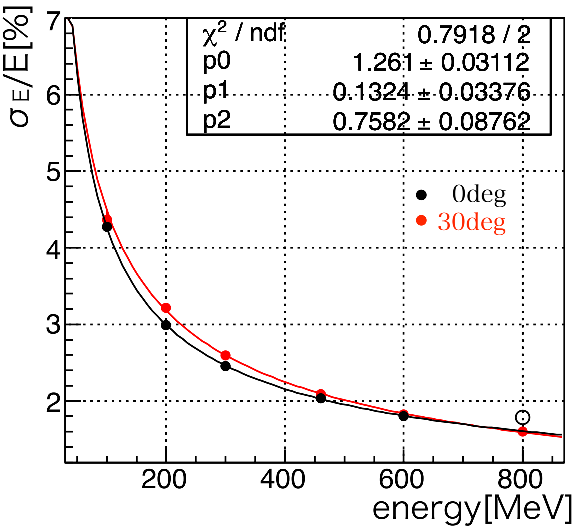

Figure 3.40: The obtained energy resolutions were parameterized with Equation 3.18. The black dots and line show the obtained energy resolutions and the fitting function for the incident angle of 0°, respectively. The data point for (800 MeV, 0°), shown as a black circle, was excluded from the fitting to suppress the effect of the non-linearity. The red dots and line are for the incident angle of 30°, which suffered less from the non-linearity, for comparison. The χ^2 and the fitting parameters in this figure are for the 0° data.

One method was to use an external light-rich scintillator as a reference of timing. As described in Section 3.1.5, we made a special run to measure the timing resolution. We attached two PMTs on both ends of the scintillator. If we use $\frac{1}{2}(t_1+t_2)$ as the reference of timing, where t_i is the timing of each PMT, the timing resolution of a crystal, $\sigma_{t_{\mathrm{CsI}}}$, can be calculated from the width of $t_{\mathrm{CsI}} - \frac{1}{2}(t_1+t_2)$ distribution:

$$\sigma_{t_{\mathrm{CsI}}-\frac{1}{2}(t_1+t_2)} = \sigma_{t_{\mathrm{CsI}}} \oplus \frac{1}{2}\sigma_{(t_1+t_2)} \ . \tag{3.19}$$

The width of sum, $\sigma_{t_1+t_2}$, was estimated by the width of difference, $\sigma_{t_1-t_2}$. The timing, t_1 and t_2, had some incident position dependence. The effect appears in t_1-t_2 but not in t_1+t_2 because they were anti-correlated. We checked the correlation between t_1-t_2 and the hit position in the scintillating fiber position detector, and corrected for the position dependence. As a result, the width $\frac{1}{2}\sigma_{t_1+t_2}$ was estimated to be 100 ps. Because a e^+ shower develops perpendicularly and longitudinally to the incident direction, the time difference between the incident timing and the timing when a PMT detects scintillating light has a dependence of the distance from the incident position. To remove the time spread by the shower development, the width was calculated for each incident position region relative to the evaluating crystal as shown in Fig. 3.41. The expected time difference between regions are about 100 ps. Figure 3.42 shows the obtained timing resolutions for different regions as a function of energy deposit in a crystal.

The other method to evaluate the timing resolution was to use the timing difference between two neighboring crystals. Both of the selected crystals had typical light yields and were viewed by PMTs with typical gains, and thus expected to have the same timing resolution. We can thus simply divide the width of the timing difference between those two crystals by $\sqrt{2}$ to get

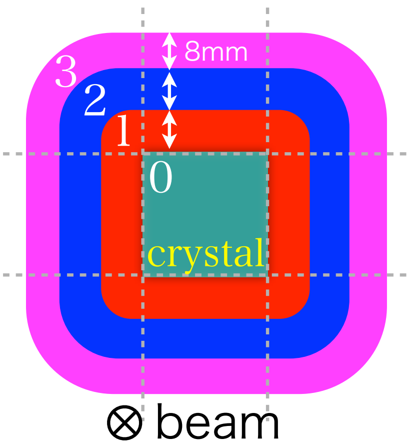

Figure 3.41: The timing resolution was calculated for each incident position region relative to the evaluating crystal, to avoid the time spread by shower development. 0) hit on the crystal, n) distance from the crystal $< 8n$ mm ($n \geq 1$).

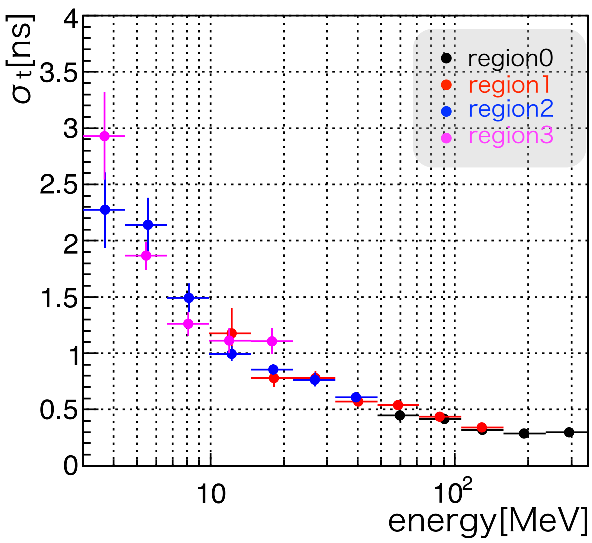

Figure 3.42: The obtained timing resolutions as a function of deposit energy in a crystal. The color of the dots indicate the hit position regions shown in Fig. 3.41.

the timing resolution of each crystal. To remove the time spread by shower development, the distance from the perpendicular bisector of the neighboring crystals to the incident position was required to be less than 2 mm, as shown in Fig. 3.43. Because we want to know the timing resolution for various energies, the deposit energy difference between the two crystals was required to be less than 10 % of itself. Figure 3.44 shows the obtained timing resolution. It was consistent with the result obtained with the previous method.

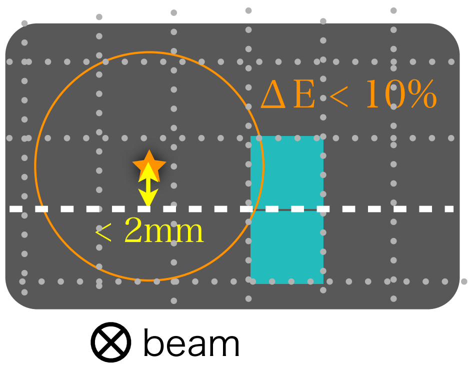

Figure 3.43: The distance from the perpendicular bisector of the neighboring two crystals to the incident position was required to be less than 2 mm, to suppress the time spread caused by shower development.

Because the results obtained with the two methods were consistent with each other, we combined the results and parametrized the combined result with the function:

$$\sigma_t = \frac{p_0}{\sqrt{E}} \oplus p_1 \quad (E : \mathrm{GeV}). \tag{3.20}$$

We obtained $p_0 = 0.121 \pm 0.002$ ns and $p_1 = 0.10 \pm 0.02$ ns for energy deposit more than 6 MeV . We also fitted the result including the energy deposit below 6 MeV with the function:

$$\sigma_t = \frac{p_0}{\sqrt{E}} \oplus \frac{p_1}{E} \oplus p_2 \quad (E : \mathrm{GeV}). \tag{3.21}$$

We obtained $p_0 = 0.115 \pm 0.003$ ns, $p_1 = 0.005 \pm 0.001$ ns and $p_2 = 0.13 \pm 0.02$ ns. The fitted functions are shown in Fig. 3.45.

3.7 Summary of this chapter

We ran a beam test to measure the basic performance of the upgraded calorimeter. We developed the procedure of the pulse shape analysis to reconstruct deposit energy and timing. We found an energy non-linearity, and developed a new calibration method to treat the non-linearity. Based on the studies, we evaluated the energy resolution and the timing resolution of the calorimeter.

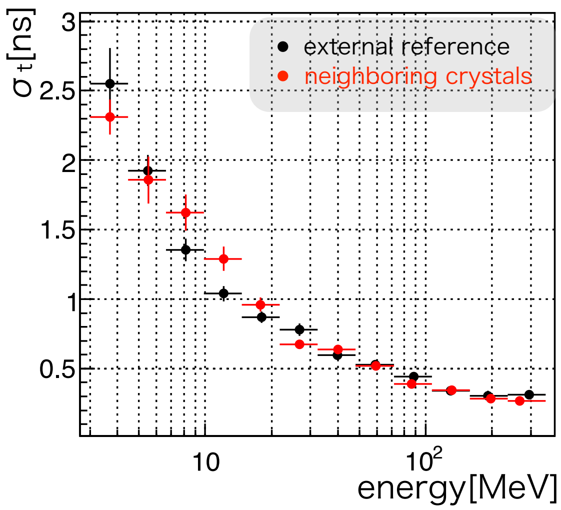

Figure 3.44: The obtained timing resolutions as a function of deposit energy in a crystal. The black dots show the results obtained with using the external scintillator, and the red dots show the results obtained with the neighboring two crystals. The position dependent values of the former result were combined into one for each energy range.

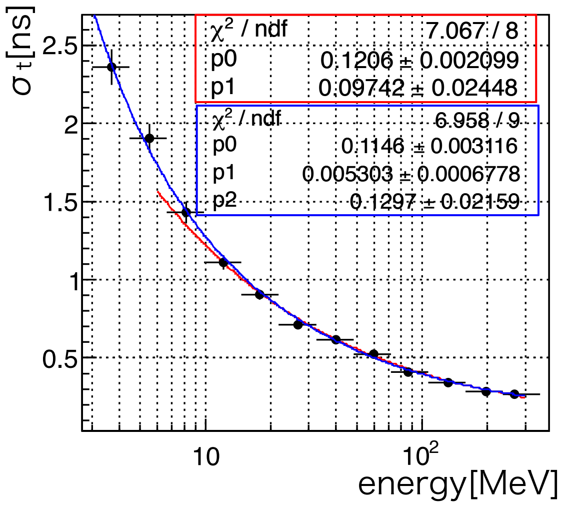

Figure 3.45: The obtained timing resolutions were parameterized with Equation 3.20(red line) and 3.21(blue line). The black dots show the result of data combined with using the external scintillator and the neighboring crystal method, as a function of the deposit energy.

Chapter 4

Performance of the waveform readout

In this chapter, we will describe a study on the performance of the waveform readout.

4.1 Outline of this chapter

If we know the mechanism of the pulse shape generation with the Bessel filter and FADC, we can port the mechanism to Monte-Carlo calculation, and fully simulate detector responses. By simulating full detector responses including pulse shapes, we can search for a possible problem with the waveform readout or estimate the performance of detectors in a certain condition which is difficult to measure directly.

We developed a new method to generate pulse shapes which are expected to be recorded with a combination of the Bessel filter and FADC. With the new method, we can generate pulse shapes using fundamental properties of single photoelectrons: "typical waveform", and the probability density function in timing (timing PDF). Basic idea of the new method is to distribute single photoelectrons according to the timing PDF, and overlay the typical waveform of each single photoelectron.

We used the timing resolution as a reference to evaluate the new method. We measured the timing resolution for various numbers of photoelectrons. The timing resolution is affected by multiple sources, such as photon statistics, ground noise and geometrical size of scintillators. Among them, the effect of photo statistics is relatively large and depends on the energy.

We first describe the measurement of the timing resolution and properties of single photoelectrons in Section 4.2. We used a plastic scintillator to check the validity of our new method to generate pulses. In Section 4.3, we describe the procedure of the new method in detail. Next, we describe the property measurement for CsI crystals in Section 4.4. At the end, we evaluate the new method by comparing the estimated performance of the CsI calorimeter with the obtained results described in the previous chapter.

4.2 Measurement

We first measured the timing resolution of a plastic scintillator as a function of the number of photoelectrons in an ordinal method as a reference. For our new method, we also measured typical waveform and timing PDF of single photoelectrons.

4.2.1 Timing resolution

Figure 4.1 shows an overview of the setup used to measure the timing resolution. S1 and S2 were plastic scintillation counters to trigger cosmic rays, and also to measure their timings. S3 was a lead/scintillator sandwich counter of interest. The gain of the PMT (Hamamatsu H7195) for S3 was calculated by measuring the charge of a single photoelectron signal (Fig. 4.2). The number of photons from S3 was reduced by a variable neutral density filter placed in front of the PMT. Waveforms of S1, S2 and S3 were recorded with a 125MHz FADC board. The timing and charge of the pulse from S3 were also measured with a usual TDC and ADC.

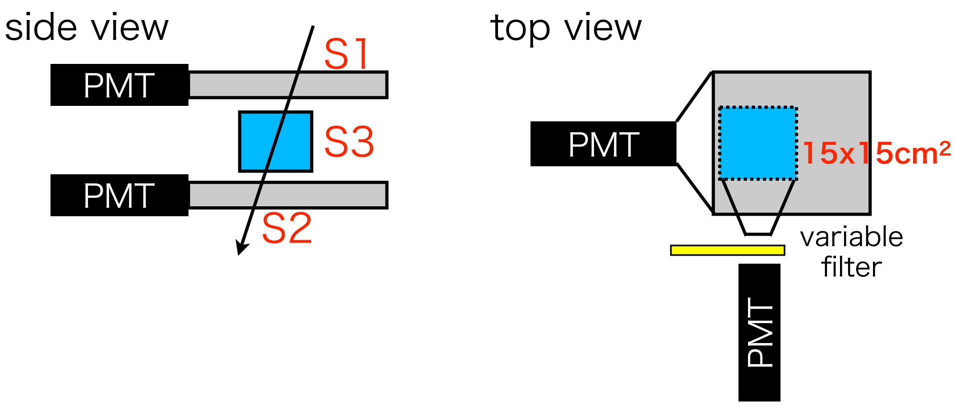

Figure 4.1: A setup used to measure the timing resolution for different numbers of photoelectrons. S1 and S2 were plastic scintillators to trigger cosmic rays. S3 was a lead/scintillator sandwich counter of interest. A variable neutral density filter was placed between S3 and a PMT for S3 to reduce the number of photons from S3.

The timing resolution of the scintillator was calculated in the following way. First, we measured the width of the timing difference, $t_3 - \frac{1}{2}(t_1 + t_2)$, where t_i is the timing of Si. Because the timings of all the counters are independent, the width, $\sigma_{t_3-\frac{1}{2}(t_1+t_2)}$, can be represented as

$$\begin{aligned} \sigma_{t_3-\frac{1}{2}(t_1+t_2)} &= \sigma_{t_3} \oplus \frac{1}{2}\sigma_{t_1+t_2} \\ &= \sigma_{t_3} \oplus \frac{1}{2}\sigma_{t_2-t_1} \ . \end{aligned} \tag{4.1}$$

The $\sigma_{t_2-t_1}$ can be calculated by making a histogram for $t_2 - t_1$. The σ_{t_3} can thus be calculated by:

$$\sigma_{t_3} = \sqrt{\sigma^2_{t_3-\frac{1}{2}(t_1+t_2)} - (\frac{1}{2}\sigma_{t_2-t_1})^2} \ . \tag{4.2}$$

Figure 4.3 shows the histograms of $t_2 - t_1$ and $t_3 - \frac{1}{2}(t_1 + t_2)$ for ~ 40 photoelectrons from S3. The width, $\sigma_{t_2-t_1}$, was 1.05 ± 0.02 ns, and it was consistent with other measurements for various number of photoelectrons in S3. By calculating σ_{t_3} for various numbers of photoelectrons, the timing resolution was measured as shown in Fig. 4.4. This result will be used as a reference to evaluate the new method to generate pulses described next.

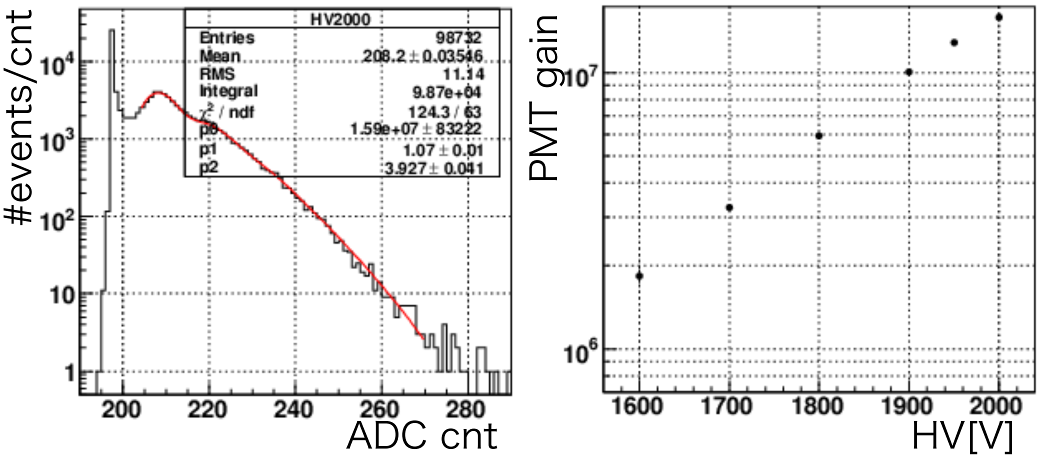

Figure 4.2: The PMT gain was measured by counting the number of photoelectrons. Figure on the left shows the ADC distribution of the well-reduced LED signal with the applied voltage of 2000 V to the PMT. By calculating the charge of a single photoelectron, we can determine the PMT gain. Figure on the right shows the measured gain for different applied voltages. The measured typical gain was 1.6×10^7 at 2000 V.

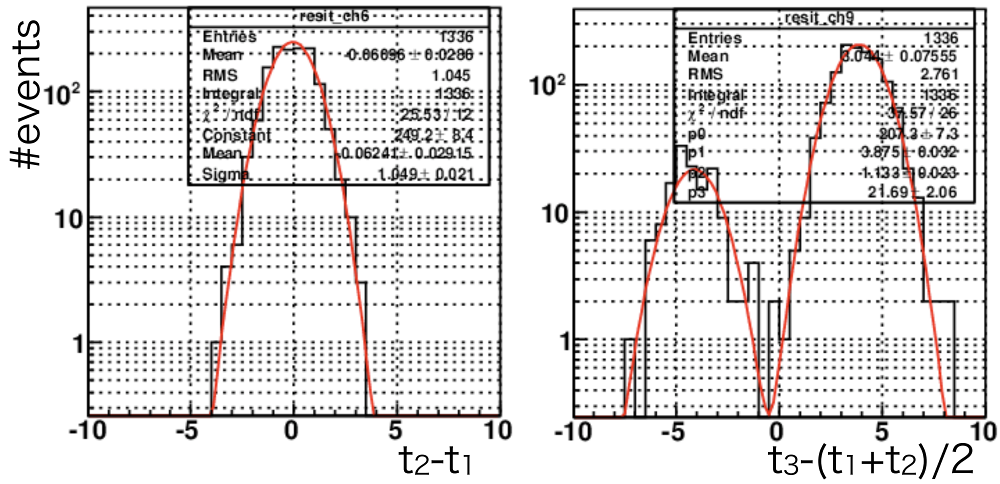

Figure 4.3: The distributions of timing differences: $t_2 - t_1$(left) and $t_3 - \frac{1}{2}(t_1 + t_2)$(right). On the right plots, the distance between the 2 peaks is 8 ns. This was caused by 1 clock time shift between the three channels, S3 and S1/S2, in the 125MHz FADC.

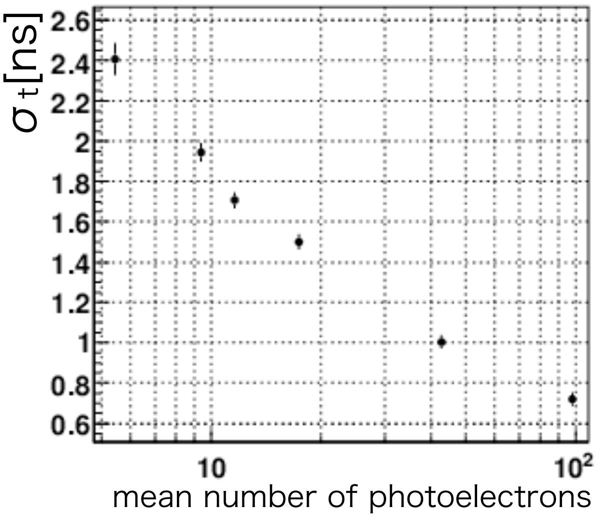

Figure 4.4: The measured timing resolution of a plastic scintillator as a function of the number of photoelectrons. This result will be compared to the values obtained by the new method to generate pulses described in the coming subsection.

4.2.2 Typical waveform

One of the fundamental properties of single photoelectrons, typical waveform, was also measured with the same setup.

The typical waveform of single photoelectrons is an averaged pulse shape for single photoelectrons passing through the Bessel filter. For this measurement, we further reduced the number of photoelectrons from S3 by the variable neutral density filter, and made "single photoelectron dominant samples". The mean number of single photoelectrons in the Poisson distribution was about 5×10^{-3}. Figure 4.5 shows the ADC distribution of the measurement. A single photoelectron peak can be seen clearly in region (2). Figure 4.6 shows the waveform of a single photoelectron recorded with the 125 MHz FADC. The typical waveform was parameterized with Asymmetric Gaussian with a lower older (Equation 3.17). Figure 4.7 shows the distribution of a and σ_0 for single photoelectron pulses coming through the Bessel filter. We obtained $a = 0.0626$, and $\sigma_0 = 17.95$ ns.

4.2.3 Timing PDF

Another fundamental property of single photoelectrons, timing PDF, was also measured with the same setup.

The timing PDF of single photoelectrons depends on type of scintillators. To measure the PDF of single photoelectrons, we changed the variable neutral density filter setting to increase the rate of single photoelectrons, and suppressed the effect of thermal electrons. The mean number of single photoelectrons in the Poisson distribution was 0.3. Figure 4.8 shows the ADC and TDC distributions of the data with a higher rate. By applying an energy cut to select single photoelectrons as shown in Fig. 4.8, the number of two photoelectron events became negligible.

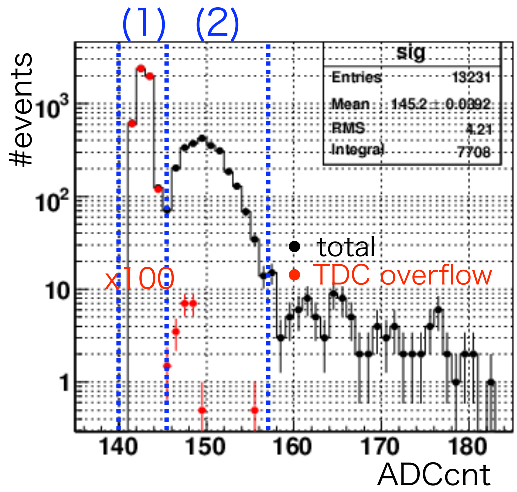

Figure 4.5: The S3 ADC distribution of the "single photoelectron dominant samples". The red dots show the TDC overflow data in which no photoelectrons were observed, and the black histogram shows whole data. The zero photoelectron data was recorded once every 100 events. The single photoelectrons clearly show up in region (2).

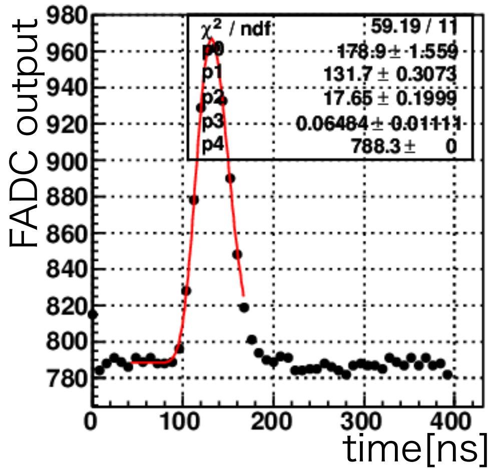

Figure 4.6: A waveform of the single photoelectron recorded with the 125 MHz FADC. The typical waveform of single photoelectron was parameterized with lower order Asymmetric Gaussian (Equation 3.17). The red line shows the fitted function.

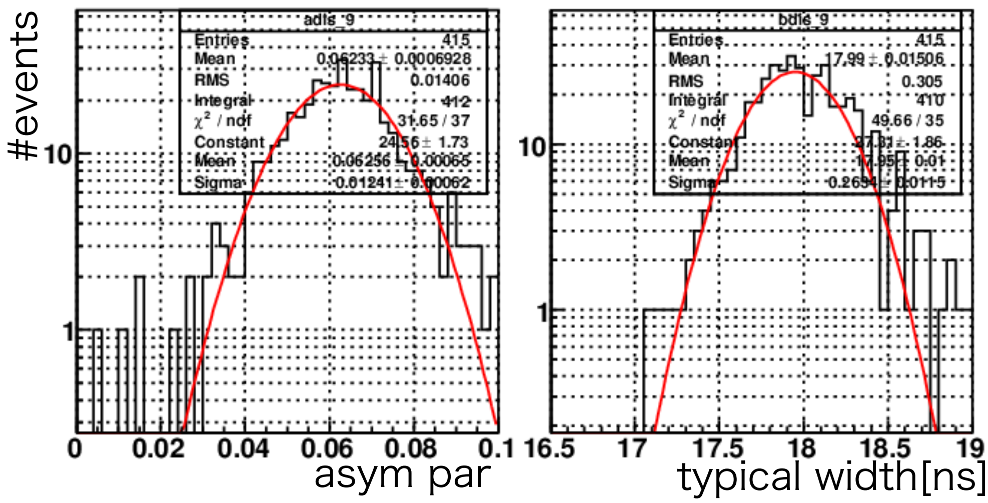

Figure 4.7: The distribution of a(left) and σ_0(right) in Equation 3.17 for single photoelectron pulses through the Bessel filter.

This timing distribution was also parameterized with Asymmetric Gaussian with a lower order (Equation 3.17). The asymmetry parameter, a, was 0.244, and the typical width, σ_0, was 3.02 ns.

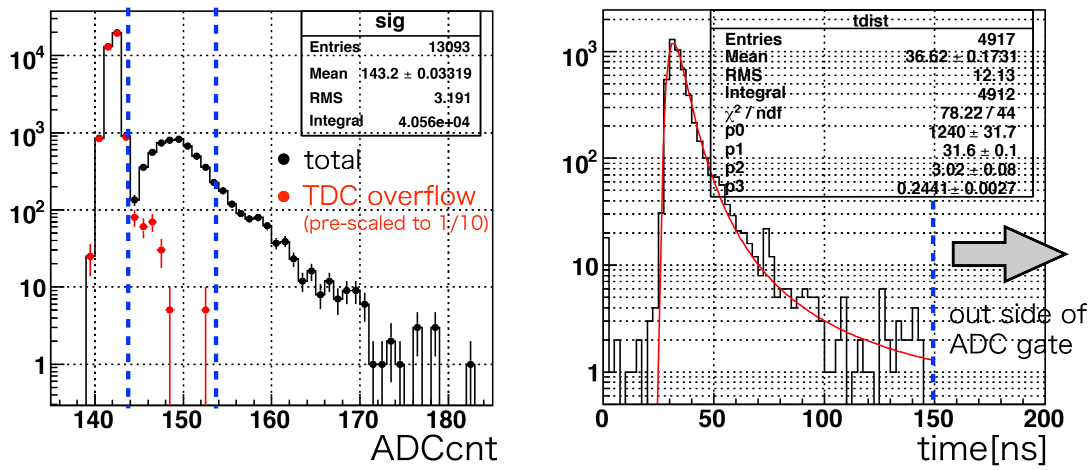

Figure 4.8: Figure on the left(right) shows the ADC(TDC) distribution of the data with a higher rate. Left) The black histogram shows all the recorded events and the red dots show events with no photoelectrons observed (TDC overflow). The zero photoelectron data was pre-scaled to 1/10 during data taking. Events between the blue broken lines were used as single photoelectron samples. Right) The timing distribution was also parameterized with lower order Asymmetric Gaussian (Equation 3.17). The red line shows the fitted function. The events later than 150 ns were outside of the ADC gate.

The observed timing distribution is not the true PDF itself. It is also deformed by the timing resolution of the trigger counters, $\sigma_t \sim 0.7$ ns. We made a toy Monte-Carlo simulation to estimate the shift of each parameter caused by the deformation. Figure 4.9 shows an example of the effect. We determined the true timing according to the PDF, smeared the timing with a timing resolution ($\sigma_t = 2$ ns in this figure), and fitted the Asymmetric Gaussian (Equation 3.17) to the smeared timing distribution. The fitted function is slightly wider than the original PDF. We first used the measured parameters as inputs and checked how the shape parameters, a and σ_0, were shifted by the amount of the smearing resolution. According to the toy Monte-Carlo simulation, the parameter shifts were relatively small (-3 % for a and +6 % for σ_0) for the smearing resolution, $\sigma_t = 0.7$ ns. We assumed the parameter shifts for the measured parameters are the same as the parameter shifts for the true parameters, and adopted a 3 % larger asymmetry parameter and 6 % smaller typical width as the true PDF parameters. Figure 4.10 shows the parameter shifts of the timing PDF by the timing resolution estimated with the toy Monte-Carlo simulation. The measured parameters were obtained when the smearing resolution is around 0.7 ns. This value is consistent with the timing resolution of the trigger counters, $\sigma_t \sim 0.7$ ns.

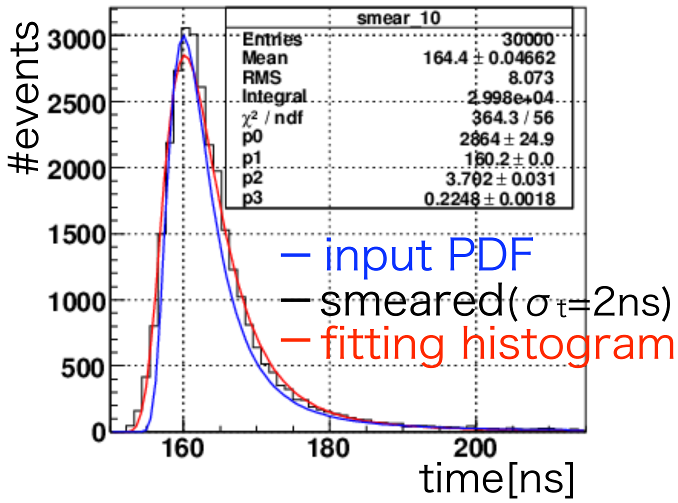

Figure 4.9: An example of deformation by timing resolution. Blue line shows the input PDF, black histogram shows the PDF smeared by a 2 ns timing resolution, red line shows the fitting result of the histogram. The fitted function was slightly wider than the input PDF.

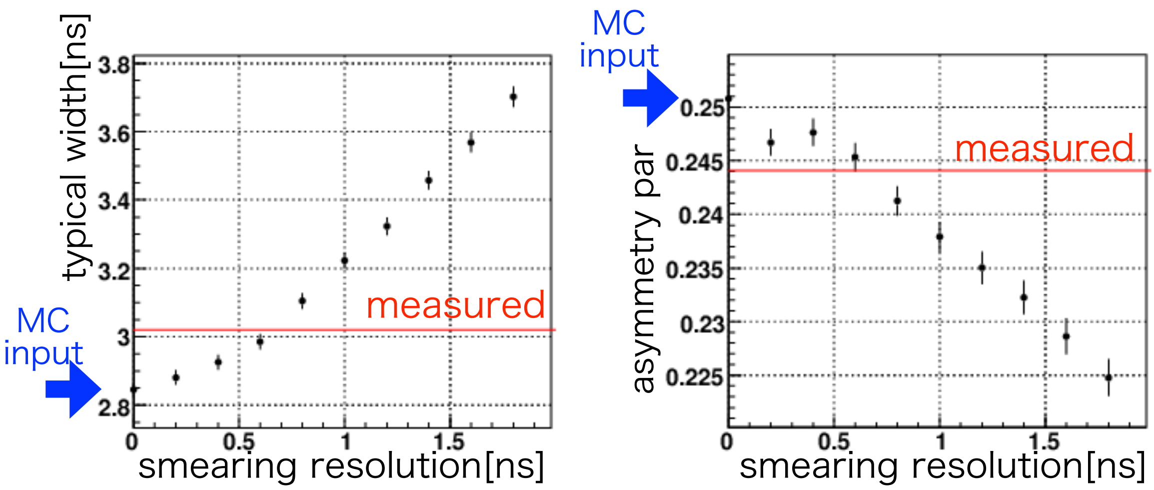

Figure 4.10: The parameter shifts by timing resolution estimated by a toy Monte-Carlo simulation for typical width, σ_0(left), and asymmetry parameter, a(right). Horizontal axes show the smearing resolution and vertical axes show the fitted parameters. Blue arrows show the MC input parameters, red lines show the measured parameters.

4.3 Performance estimation

Based on the measured properties of single photoelectrons, recorded pulse shapes were simulated and the timing resolution was estimated.

In the following subsections, we first describe the pulse shape simulation procedure, and then compare the estimated performance with the measured results.

4.3.1 Pulse shape simulation procedure

We will describe our procedure to simulate the pulse shape. The data was taken for various "mean" numbers of photoelectrons. In the simulation, we first chose the number of photoelectrons following a Poisson distribution for every event[1], and distributed the photoelectrons according to the timing PDF decided earlier. Each waveform was generated by overlaying the typical waveform for each photoelectron. A ground noise of 3.7 counts in σ, equivalent to 0.014 times of the pulse height of a single photoelectron, was also added every 8 ns. The leading timing was shifted every event by the time offset caused by the deviation of hit position within the 15×15 cm^2 lead/scintillator sandwich. Assuming that the light velocity in the scintillator was 15 cm/ns, the time deviation by the geometrical size was 0.28 ns in RMS. The height of the generated waveforms were picked every 8 ns, assuming the 125 MHz FADC, and analyzed in the same way as data. This simulation procedure is summarized in Fig. 4.11, and Fig. 4.12 shows a generated waveform.

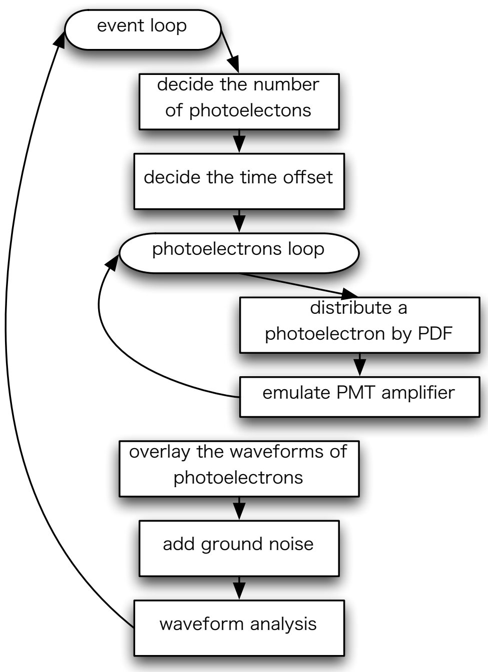

Figure 4.11: The simulation procedure of the pulse shape generation.

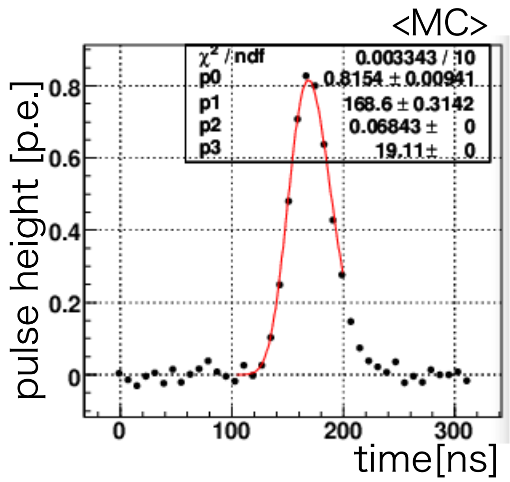

Figure 4.12: A waveform generated by the simulation procedure described in the text.

[1] Because we cannot observe 0 photoelectron event, we just made events containing one or more photoelectrons.

4.3.2 Data comparison

Figure 4.13 shows data and Monte-Carlo energy distributions for 17.4 photoelectrons on average. The Monte-Carlo reproduced the distribution of data around the peak, but not in lower energy region. Because the data was taken by the external trigger counters, the measured data contained thermal electrons and electric noise. The measured data also contained cosmic ray hits near the edge of the scintillator. To compare the timing resolutions, events were required to have more than half of the mean number of photoelectrons. Figure 4.14 shows the timing resolutions for various numbers of photoelectrons for data and Monte-Carlo. The Monte-Carlo simulation based on the generated pulse shapes reproduced the measured timing resolution.

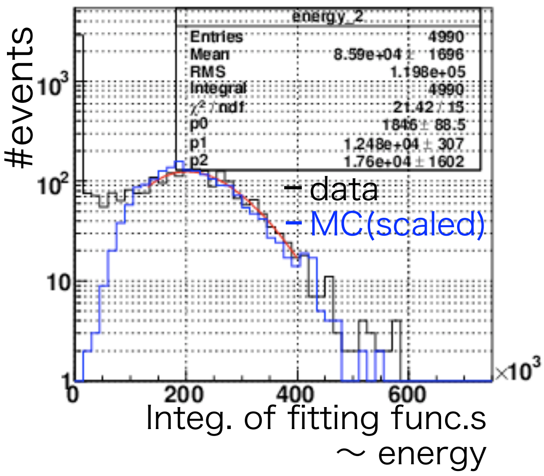

Figure 4.13: The energy distribution for data and Monte-Carlo. The black histogram shows data, and the blue histogram shows Monte-Carlo. The distribution of Monte-Carlo was horizontally scaled to adjust the peak position to data, and the red line is a fitted function used to adjust the horizontal scale.

4.4 Parameters for CsI crystals

In order to estimate the performance of our CsI calorimeter, the timing PDF and typical waveform of the CsI crystals are necessary. To measure the properties of single photoelectrons from the CsI crystals, we prepared a type of phototube, Hamamatsu R4125, instead of the PMT for the KOTO experiment (R5364). This is because the gain of R5364 is too low to observe single photoelectrons. The PMTs for the KOTO experiment were originally made for the KTeV experiment, by reducing the number of dynodes of R4125 from 10 to 5 in order to achieve a better energy linearity. Typical gains of R4125 and R5364 are 8.7×10^5 and 4800, respectively. To keep the properties of single photoelectrons of the R4125 similar to R5364, the HV divider ratios were set to K-3-2-2-2-2-1-1-1-1-1-1-A; the first six ratios are the same as for R5364. In the following measurement, we used the same technique as described in the previous sections, except that the CsI crystal with a custom-made PMT was used.

We describe the measurement of properties of single photoelectrons and absolute light yields of CsI crystals in the following subsections.

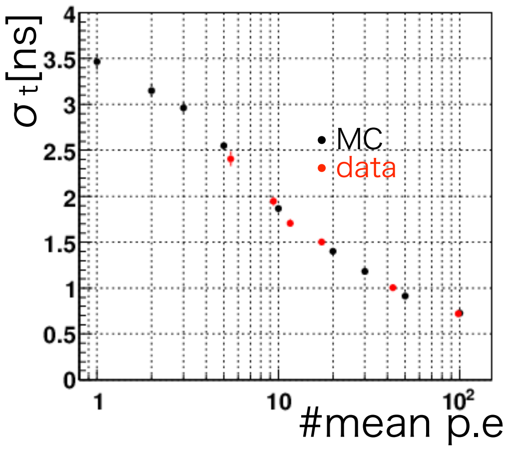

Figure 4.14: The measured timing resolution (black dots) and the estimated timing resolution (red dots) of the plastic scintillator for various numbers of photoelectrons.

4.4.1 Properties of single photoelectrons

The typical waveform and timing PDF of single photoelectrons were measured for CsI crystals. Figure 4.15 shows a waveform of a single photoelectron recorded with the 125 MHz FADC. The typical waveform was also parameterized with Asymmetric Gaussian (Equation 3.17), and the distributions of the fitted parameters are shown in Fig. 4.16. We obtained $a = 0.0443$, and $\sigma_0 = 23.71$ ns.

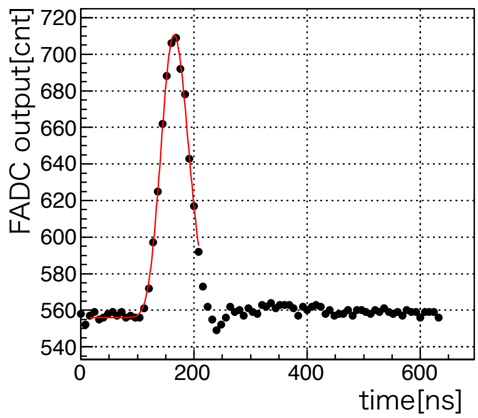

Figure 4.15: A waveform of a single photoelectron. The typical waveform of single photoelectron was also parameterized with Asymmetric Gaussian with a lower order (Equation 3.17). The red line shows the fitted function.

Figure 4.17 shows the timing distribution of single photoelectrons obtained with a CsI crystal. The shape of the timing distribution is slightly different from the shape for plastic scintillator, and the distribution was parameterized with Asymmetric Gaussian with a higher order (Equation 3.1). The fitted parameters are $a = -1.2 \times 10^{-7}$ ns^{-3}, $b = 4.5 \times 10^{-5}$ ns^{-2}, $c = -5.8 \times 10^{-3}$ ns^{-1}, $d = 0.54$ and $\sigma_0 = 3.3$ ns.

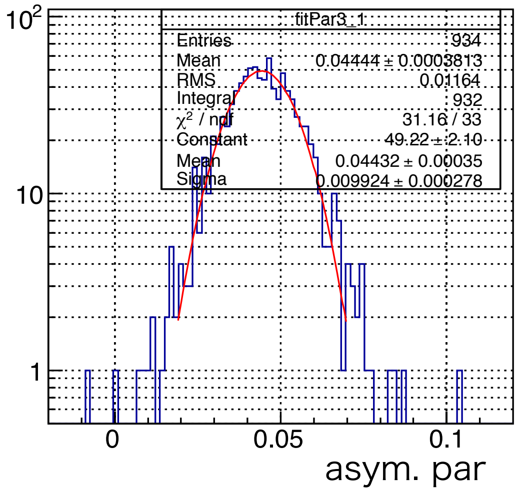

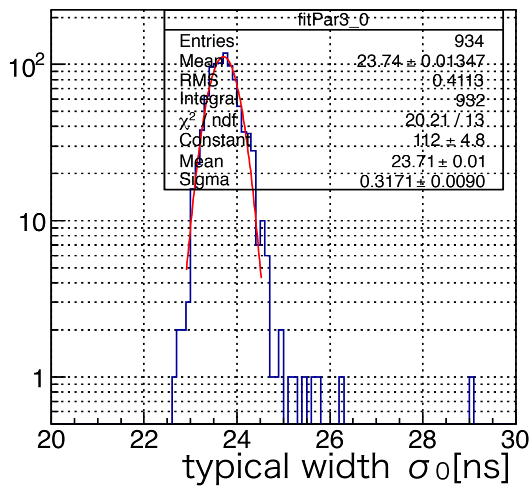

Figure 4.16: The distribution of a(left) and σ_0(right) in Equation 3.17 for single photoelectron pulses after the Bessel filter tuned for the CsI crystals.

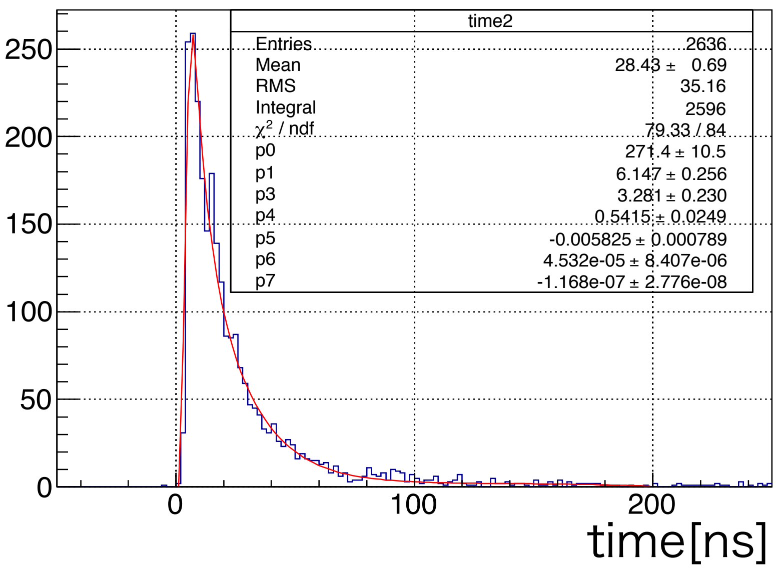

Figure 4.17: The timing distribution of single photoelectrons from a CsI crystal. The timing distribution was parameterized with Asymmetric Gaussian with a higher order (Equation 3.1). The red line shows the fitted function.

4.4.2 Absolute light yield

Absolute light yields for some crystals were also measured. Though relative light yields of all the CsI crystals had been already measured with radio active source, absolute light yields are necessary to estimate the performance of the CsI calorimeter. Absolute light yields were measured with cosmic ray data. Figure 4.18 shows the observed charge distributions of cosmic rays passing through 25 mm of the crystal. According to the Monte-Carlo simulation, the most probable value is 14 MeV.

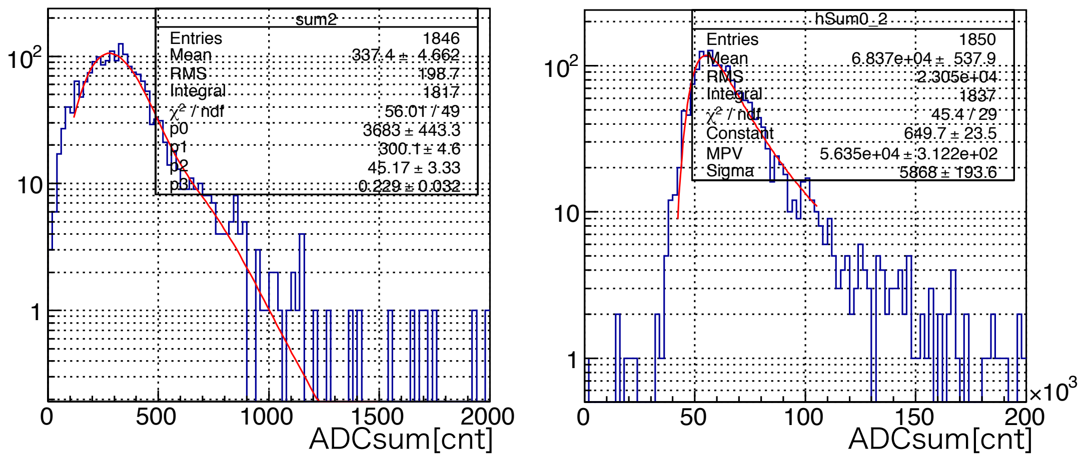

Figure 4.18: The observed charge distribution of a CsI crystal obtained with cosmic rays with(left) and without(right) the variable neutral density filter. The filter was set to generate single photoelectron dominant samples and measure the charge of single photoelectron pulses.

We measured the absolute light yields for 34 crystals. Figure 4.19 shows the correlation between the relative light yields and the measured absolute light yields. By fitting the correlation to a line, the mean absolute light yields of all the CsI crystals for the the KOTO experiment was estimated to be 12.7 p.e./MeV.

4.5 Comparison and Evaluation

We compared the results obtained with the beam test data and the estimation based on the timing PDF of CsI crystals described in this chapter. We first compared the timing resolution. Figure 4.20 shows the timing resolution as a function of energy deposit in a CsI crystal. The estimation based on the timing PDF agrees with the result obtained with beam test data.

We next compared the pulse shape generated based on the timing PDF with the pulse shapes recorded in the beam test data. We fitted the generated pulse shapes with lower order Asymmetric Gaussian (Equation 3.17), and compared the shape parameters, σ_0 and a, with the parameters for all the crystals in data. Figure 4.21 compares the distributions of the shape parameters for all the crystals to the parameters for the generated pulses. The pulse shapes differ between channels depending on the individual difference of the Bessel Filter on the FADC board. Because the generated pulses are based on the data for a certain channel, the parameters for the generated pulse shapes were consistent with the parameters for crystals in data.

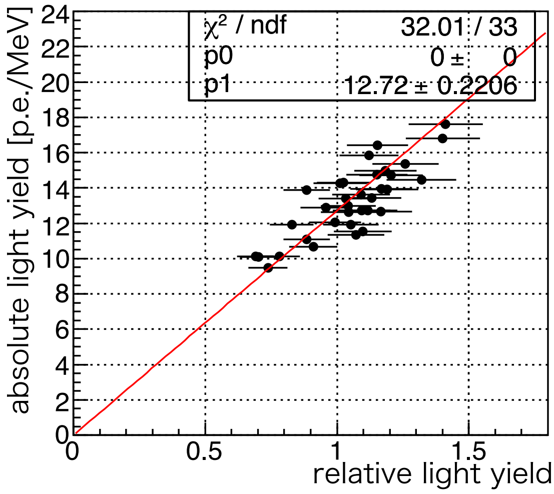

Figure 4.19: The correlation between the relative light yields and the measured absolute light yields of CsI crystals.

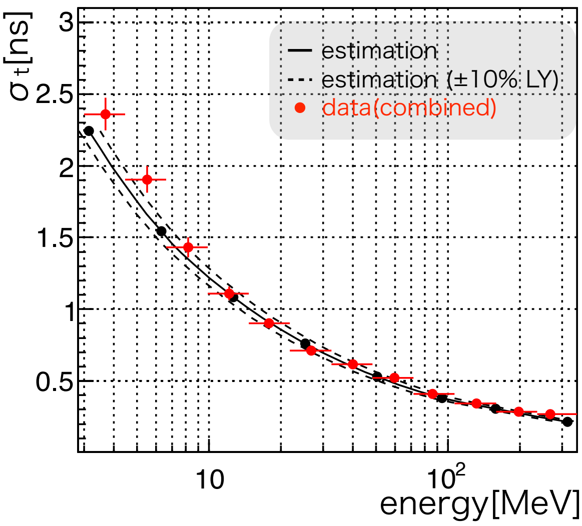

Figure 4.20: The timing resolution as a function of the deposit energy in a CsI crystal. The black solid line with dots shows the estimated timing resolution, the black dashed lines show the ones with 10 % smaller/larger light yield corresponding to the error of the measured relative light yields. The red dots show the result of data combined with using the external scintillator and the neighboring crystal method in Fig. 3.45.

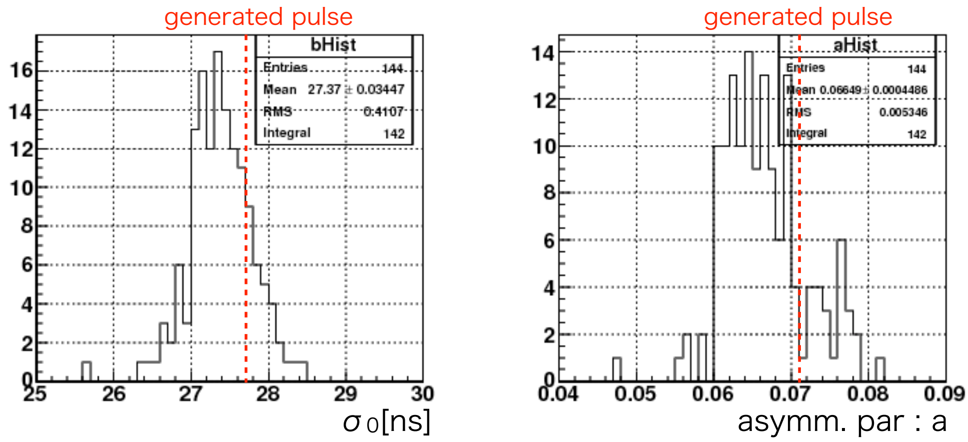

Figure 4.21: The distributions of the shape parameters in Equation 3.17, σ_0(left) and a(right), for all the crystals. The red dashed lines show the value observed with the generated pulses.

We also compared the energy resolutions in the following two ways. We first compared the total energy distributions between data and Monte-Carlo with pulse shapes based on the timing PDF. We used (600 MeV, 40°) dataset because it suffered less from the non-linearity, and the expected energy resolution thus was better due to larger beam energy. Figure 4.22 shows the total energy distribution for data and Monte-Carlo. The estimated beam energy spread, $\sigma_E/E \sim 0.6$ %, was taken into account for the Monte-Carlo. The Monte-Carlo with generated pulse shapes reproduced the energy resolution of the calorimeter.

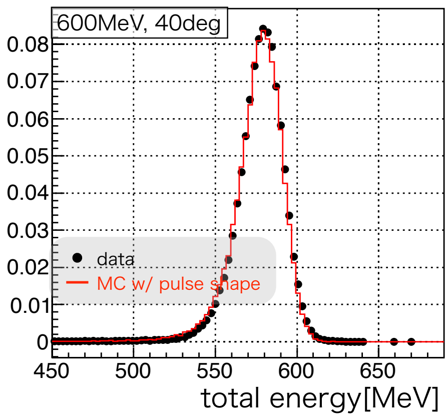

Figure 4.22: The total energy distributions of data and Monte-Carlo with the generated pulse shapes. The integrals of both histograms were normalized to 1.

We also checked the energy resolution with the cosmic ray data. We fitted the energy distribution with the Landau function, and took the ratio of width, σ, to the most probable value (MPV). Figure 4.23 shows the distributions of the ratio for data and Monte-Carlo with and without the generated pulses. The central value of the ratio of Monte-Carlo with generated pulses agreed better with data.

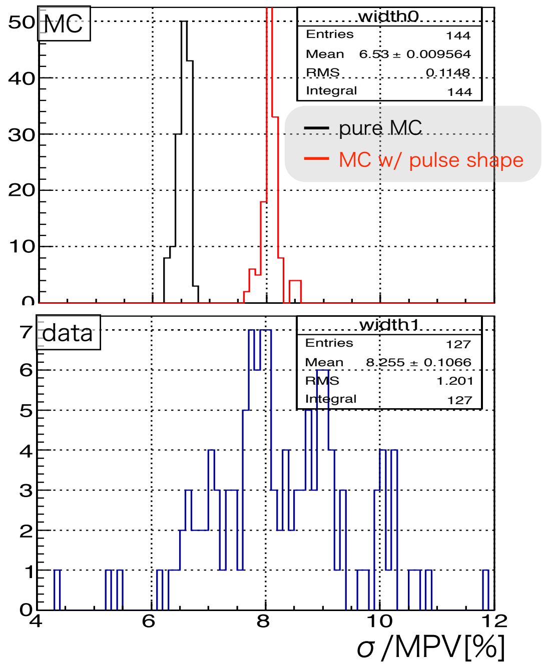

Figure 4.23: The distributions of the ratio of σ to the most probable value of the deposit energy distribution with cosmic ray events for Monte-Carlo(top) and data(bottom). The red(black) lines show the distribution obtained with the Monte-Carlo with(without) generated pulses, and the blue lines show the distribution obtained with data. The difference of widths between data and Monte-Carlo is caused by the difference of statistics between them.

We confirmed that the estimation method described in this chapter can reproduce the pulse shapes and resolutions obtained with data. According to the pulse shape simulation, we found that the energy resolution of each channel was mostly determined only with photo statistics all over the energy range. It means that we achieved to fully utilize the attribute of the CsI crystals with the waveform readout.

In the following chapters, the Monte-Carlo takes into account the energy resolution for each crystal, which is confirmed with data and understood.

4.6 Summary of this chapter

We developed a new method to generate pulse shapes to be recorded with a combination of the Bessel filter and FADC, based on the fundamental properties of single photoelectrons: "typical waveform", and the timing PDF. By comparing the estimated performance with the beam test results, we showed that we can reproduce the obtained performance with the method, and that we understand the performance of the upgraded calorimeter from the first principle.

Chapter 5

New analysis method for the upgraded calorimeter

We developed new analysis methods that fully utilize the finer granularity and waveform readout capability of the upgraded calorimeter. KOTO is an upgraded experiment of the KEK-PS E391a. We already have some analysis methods to reconstruct photons and the $K_L \to \pi^0\nu\bar{\nu}$ decay. The existing methods, however, are not the best for the upgraded experiment. As described in Section 2.2.1, the crystals for the CsI calorimeter were changed from large 7 cm square crystals to small 2.5 cm square crystals. We need optimized analysis methods for the upgraded calorimeter. We developed new methods to reconstruct the incident positions of photons, discriminate their incident angles and directions, and separate overlapped double pulses from the phototubes. We will describe these new methods in detail.

At the KOTO experiment, multiple photons can hit the CsI calorimeter at the same time. For analyzing such data, we first find clusters to reconstruct photons, which are contiguous groups of the CsI crystals with energy deposit exceeding a threshold. We set 1.5 MeV as the energy threshold on crystal in the following analysis.

Section 5.1 describes a method to reconstruct incident positions by fitting the shower shapes. Section 5.2 describes a method to discriminate incident angles by comparing likelihoods based on the shower shapes. Section 5.3 describes a method to discriminate incident directions by using the difference of the recorded pulse shapes of photons between coming from upstream and downstream. Finally, Section 5.4 describes a possible inefficiency due to the overlapped pulses.

5.1 Incident position reconstruction

At the E391a experiment, the incident positions of photons were defined by the energy-weighted mean:

$$\boldsymbol{x}_{\text{rec}} = \frac{\sum_i e_i \boldsymbol{x}_i}{\sum_i e_i} \tag{5.1}$$

where e_i and $\boldsymbol{x}_i$ are the deposit energy and position of the i-th crystal in a cluster, respectively. Figure 5.1 shows the correlation between the incident position and the energy-weighted mean position obtained with Monte-Carlo simulation. The position obtained with the energy-weighted mean deviates from the incident position within a size of the crystal. Moreover, the calculation of the energy-weighted mean does not use shower shape information, though we have finer granularity with the upgraded calorimeter.

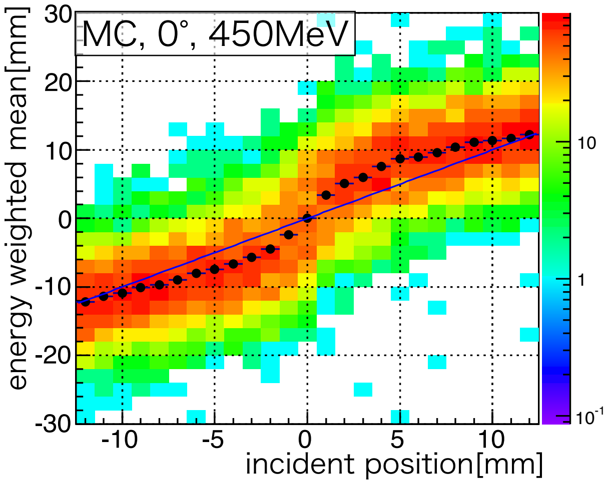

Figure 5.1: The correlation between the incident position and the reconstructed position obtained with the energy-weighted mean (Equation 5.1), obtained with Monte-Carlo simulation. Each black dot shows the mean value of the reconstructed position for each incident position range. The blue line shows the case where the both positions match. The figure was obtained with 25 mm square crystals.

We developed a new method to reconstruct incident positions by fitting the shower shape. Because we will use 2.5 cm square crystals, which are smaller than the Moriere radius of CsI, 3.8 cm, we will be able to see the electromagnetic shower shape more clearly. Basic idea of the method is to project the energy deposits in crystals in x and y directions, and fit the shape with a template. The shower shape templates were generated by Monte-Carlo simulation.

Figure 5.2 shows the correlation between the fractions of energy deposit in 0.25 mm-wide slices and their distances from the incident positions. The 0.25 mm pitch is smaller than the expected position resolution. By summing energies in 100 slices, we obtained the mean fraction of energy deposit for a 25 mm-wide band. Figure 5.3 shows the mean energy fraction in a 25 mm-wide band for various incident angles as a function of the distance between the center of the band and the incident position. Based on the typical shower shapes for various energies and angles, the shower shape template was dynamically generated for a given incident position as shown in Fig. 5.4. Figure 5.5 shows an example of the shower shape fitting. Error for each bin was set at a value proportional to the square-root of the energy in the column/row, because the energy fluctuation is dominated by photon statistics.

We evaluated the new method with e^+s with Monte-Carlo simulation. Because e^+s generate electromagnetic showers immediately on hitting the calorimeter, but photons do not, the difference between the new and previous methods is expected to be seen more clearly with e^+s. Figure 5.6 shows the position resolutions obtained with the new fitting-based method and the previous energy-weighted mean method for different incident angles with Monte-Carlo simulation. We achieved a better position resolution with this new method for various incident angles.

The new method to reconstruct the incident position was also evaluated with the data collected at the beam test (e^+s). Figure 5.7 shows the distribution of the distance between the reconstructed position and the hit position measured with the scintillating fiber detector. The tail region of the distribution was widened by accidental activities in the scintillating fiber de-

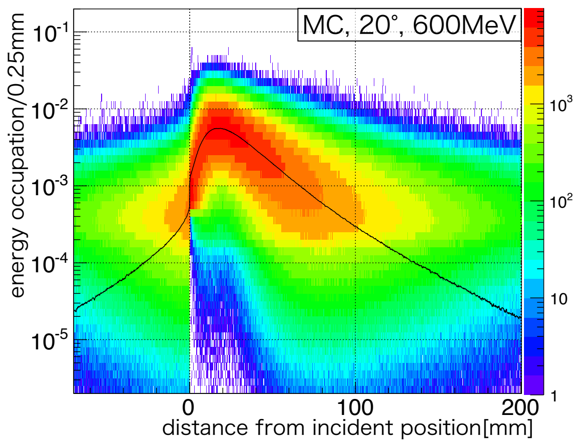

Figure 5.2: The correlation between the fractions of energy deposit in 0.25 mm-wide slices and their distances from the incident positions. The black line shows the mean energy fraction.

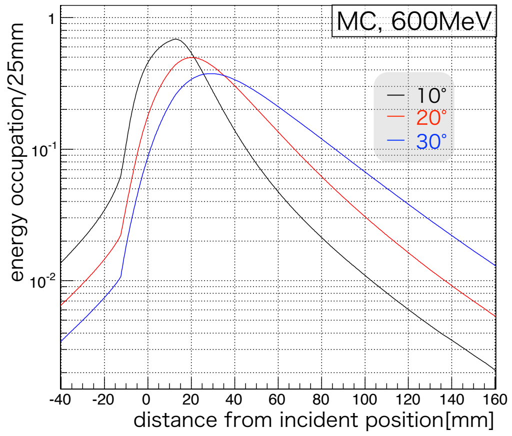

Figure 5.3: The mean fraction of energy in a 25 mm-wide band is shown as a function of the distance between the center of the band and the incident position. The black, red and blue lines show the fraction for the incident angle of 10°, 20°, and 30°, respectively.

tector, and interactions between the beam and materials in the beam line. We fitted the central part ($\pm 2\sigma$) of the distribution with Asymmetric Gaussian (Equation 3.17) and used the typical width, σ_0, to compare the position resolutions. Figure 5.8 shows the obtained position resolutions for various incident angles for data and Monte-Carlo simulations. The position resolutions obtained with the new method are consistent between the beam test data and Monte-Carlo simulation.

5.2 Incident angle discrimination

As described in Section 1.3.1, if we can discriminate the incident angles of photons, we can suppress backgrounds caused by halo kaons and neutrons.

The incident angles can be discriminated with a likelihood ratio method. The basic idea of this method is the following. We first reconstruct the $K_L \to \pi^0 \nu \bar{\nu}$ decay from two photons with the assumption that the two photons came from a π^0 decay on the z-axis, and calculate the incident angle of each photon. We next reconstruct the incident angle again assuming a certain background. For each photon, we then have two incident angles for the two assumptions, signal and background. We can then calculate the likelihood of the observed shower shape in the calorimeter for each assumption. By comparing the likelihoods for the two assumptions, we can distinguish signal from backgrounds.

The likelihood was calculated for the projection of the energy deposits on the x and y axes. The likelihood of the i-th assumption is:

$$L_i = \prod_{j;\gamma} \prod_{x,y} \prod_{k;\mathrm{row}} P(e_k | E_j, d_k, \theta_{ij}, \phi_{ij}) \ , \tag{5.2}$$

where j is an index of the reconstructed two photons, k is an index of CsI crystal column, e_k is the energy deposit in the k-th column, d_k is the distance between the center of the column and

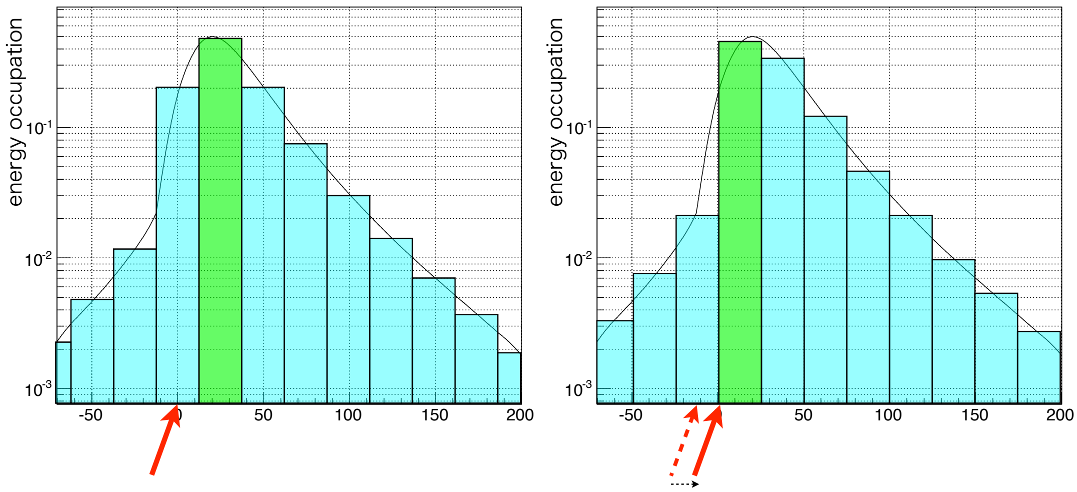

Figure 5.4: A schematic view of the dynamical generation of templates as a function of the distance between the center of the band and the incident position. The black line shows the mean energy fraction in a 25 mm-wide band as a function of the distance. A 25mm-wide bar shows the mean energy fraction of the column/row at each position. The green bar is the row of interest. Figure on the left shows a template generated for the case where the distance from the center of the row to the incident position was 25 mm. Figure on the right shows another template generated for the distance of 12.5 mm.

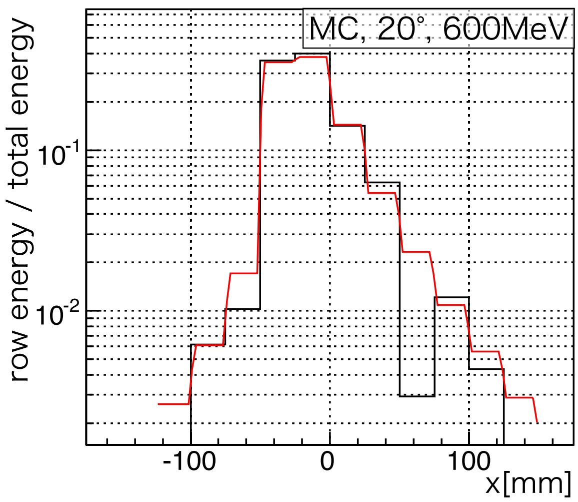

Figure 5.5: An example of shower shape fitting. The bin width corresponds to the width of a crystal. The black histogram shows the energy fraction of a single photon in each row. The red line shows the fitted template.

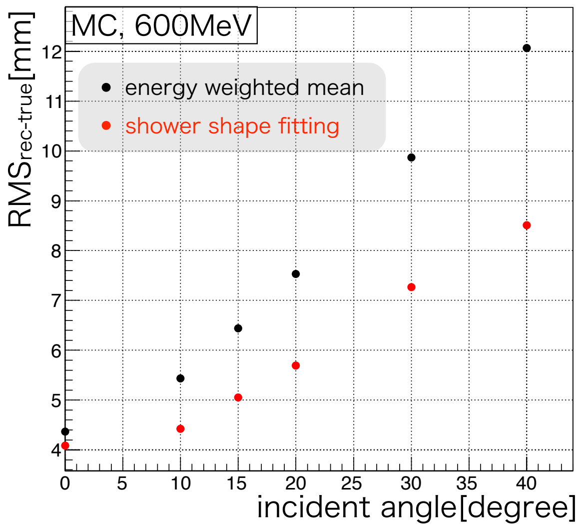

Figure 5.6: The comparison of the position resolution between the energy-weighted mean method (black) and the new fitting-based method (red) for e^+s with Monte-Carlo simulation. The RMS value of the distribution of distance between the reconstructed position and Monte-Carlo true value, was used as a position resolution in this plot.

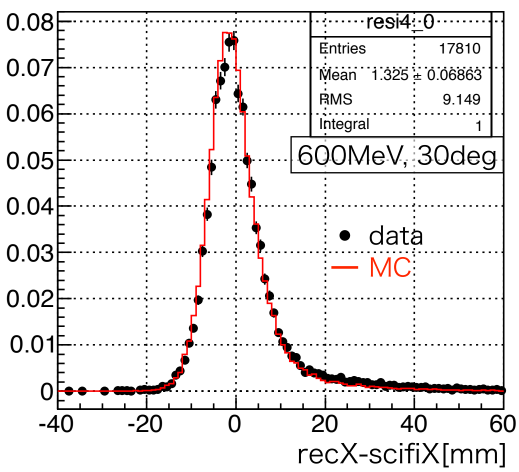

Figure 5.7: The distribution of the distance between the reconstructed position, and the hit position measured with scintillating fibers. The black dots show data and the red histogram shows Monte-Carlo simulation.

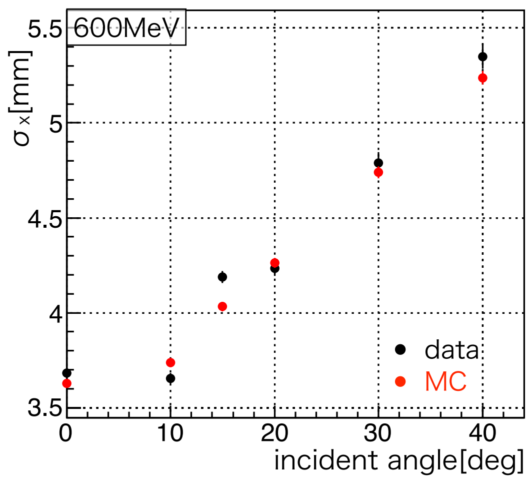

Figure 5.8: The position resolutions for various incident angles. The black (red) dots show data (Monte-Carlo). The distribution of the distance between the reconstructed position and the hit position measured with scintillating fibers was fitted with Asymmetric Gaussian (Equation 3.17), and its σ_0 was used as the position resolution.

the energy-weighted mean position, θ_{ij} and ϕ_{ij} are the polar and azimuthal angles of the j-th photon for the i-th assumption, respectively, and P is the probability density function (PDF) made via Monte-Carlo study. The PDF was prepared based on the distribution of the fraction of energy deposit for various incident energies, angels and distances from the energy-weighted mean position. Figure 5.9 shows examples of the PDFs. The likelihood ratio is then calculated by:

$$\text{Likelihood Ratio} \quad = \quad \frac{L_{\text{signal}}}{L_{\text{signal}} + L_{\text{background}}} \ . \tag{5.3}$$

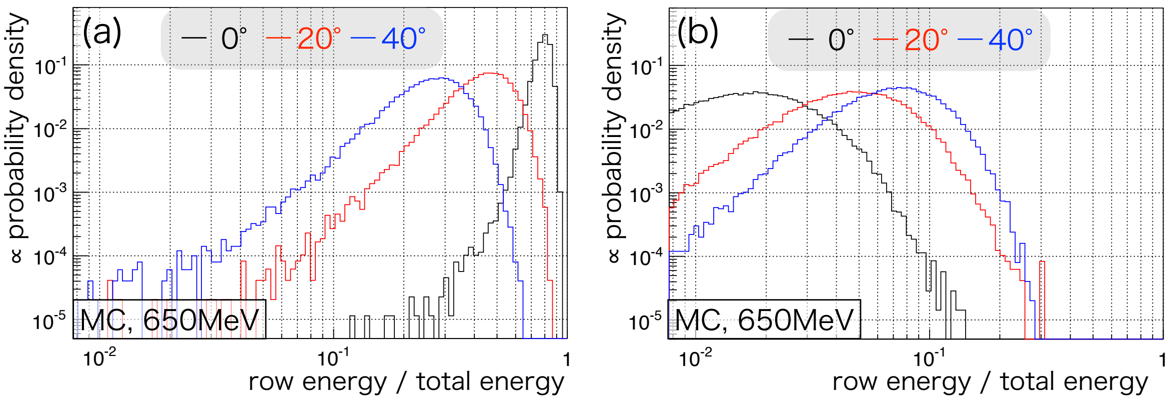

Figure 5.9: Examples of PDFs of energy fraction for 650 MeV photons at (a) 0 mm, and (b) 50 mm from the energy-weighted mean position. The black/red/blue lines show the PDFs for the incident angles of 0°/20°/40°, respectively.

The performance of the incident angle discrimination was checked with a Monte-Carlo simulation. Figure 5.10 shows the likelihood ratio distributions for Monte-Carlo samples of photons with the incident angles of 10° and 30°. It also shows the ratio of the survival probabilities that events pass a cut on the Likelihood ratio, as a function of the survival probability of the 10° samples. We can discriminate between two assumed incident angles with the likelihood ratio method.

We could not, however, check the power of the incident angle discrimination with the beam test data. Figure 5.11 shows the likelihood ratio distributions for the incident angle of 0° obtained with data, and Monte-Carlo with and without material in the beam line (the collimator and air). The data has different distribution from Monte-Carlo without the materials, and agrees better with Monte-Carlo with the materials. It means the likelihood ratio distribution was contaminated with e^+s interacting with the materials.

The background rejection power of this incident angle discrimination will be discussed in the next chapter.

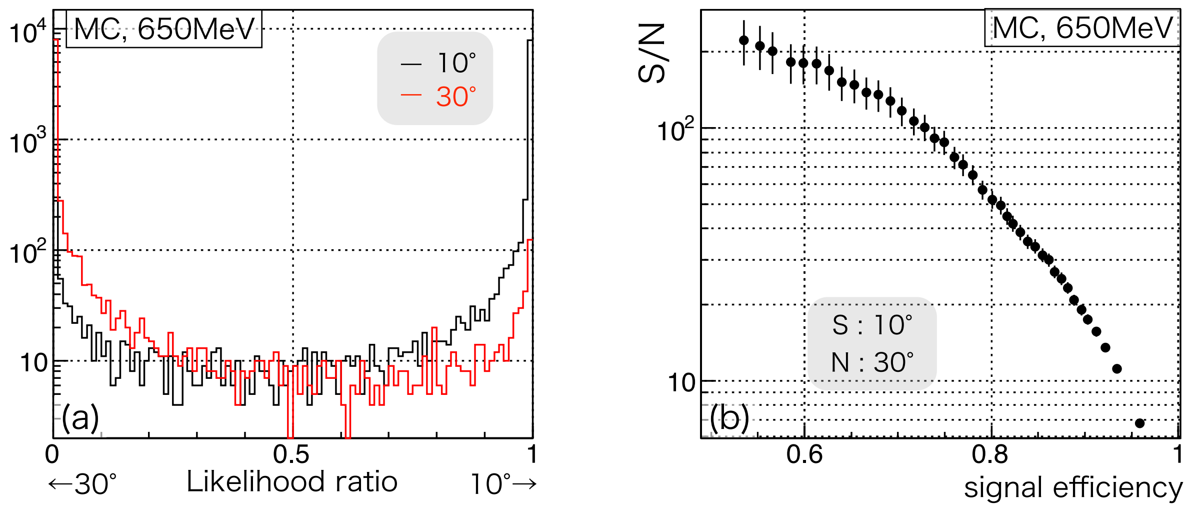

Figure 5.10: (a) The likelihood ratio distribution for Monte-Carlo samples of photons with the incident angle of 10°(black) and 30°(red). (b) The ratio of the survival probabilities between 10° to 30° samples that events pass a cut on the Likelihood ratio, as a function of the survival probability of the 10° samples.

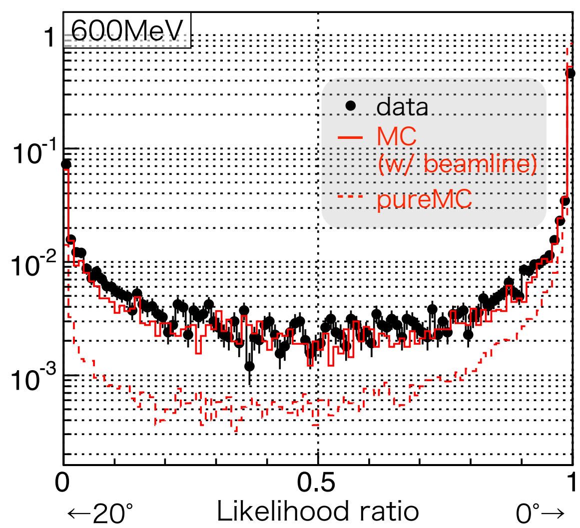

Figure 5.11: The likelihood ratio distributions for the incident angle of 0° samples. The likelihoods for the assumptions of 0° and 20° incident angles were compared. The black dots show data and the red histogram shows Monte-Carlo with materials along the beam line including a collimator and air. The red dashed histogram shows the distribution obtained with Monte-Carlo without materials in the beam line. The likelihood ratio distribution was deformed by the interactions between beam and materials in the beam line.

5.3 Incident direction discrimination

If we can identify whether the photon that generated a cluster, comes from upstream or downstream, it may help to reject backgrounds. There is a possible background source called "backward π^0". It is a π^0 generated by the interaction between a neutron and the material placed downstream of the calorimeter. Even if the photons from the π^0 hit the calorimeter from the downstream side, we cannot distinguish them from photons from the upstream side. We will then mis-reconstruct the π^0 decay vertex in the upstream side of the calorimeter, and that will become a background. If we can tell the direction of those photons, such background events can be rejected.

We found that the pulse shape depends on the position along the z-axis where the scintillation light was emitted. Figure 5.12 shows the pulse shape parameters as a function of the cosmic ray hit position within the crystals. Because the longitudinal length of the CsI crystal is enough long, the effective position where the scintillation light was emitted is close to the upstream(downstream) surface when photons comes from upstream(downstream). If we know well about the position dependence for all the crystals, we can thus identify the incoming directions of photons.

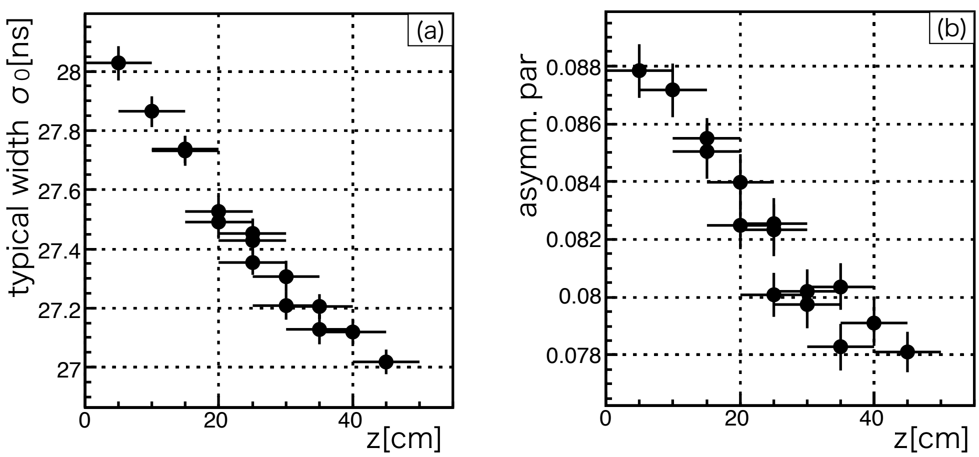

Figure 5.12: The position dependence of pulse shapes obtained with cosmic rays. The horizontal axes show the distance from the upstream surface of a CsI crystal. The shape parameters (a) typical width, σ_0, and (b) asymmetry parameter, a, depend on the muon hit position.

We will next estimate how much we can suppress the "backward π^0" background with this photon direction discrimination. We will not, however, estimate the number of the backward π^0 background events. This is because the background will be suppressed by CC04 veto counter currently being designed to be placed downstream of the CsI calorimeter.

We estimated the background rejection power with the following assumptions.

1. The position dependence of pulse shapes is independent of the energy deposit. We thus applied the position dependence obtained with cosmic ray data for all the energy ranges.

2. The pulse shape for each event depends on the depth of electromagnetic "shower maximum" of the event. The "shower maximum" is the energy-weighted mean position along

the direction of incident photons. Figure 5.13 shows a schematic view of the "shower maximum".

3. The two photons of the π^0 background events after applying all the cuts have the same properties as photons from the $K_L \to \pi^0\nu\bar{\nu}$ decay. We thus used the $K_L \to \pi^0\nu\bar{\nu}$ Monte-Carlo to estimate the rejection power for the backward π^0 background.

The estimation procedure is the following.

1. Determine the true depth of the shower maximum for each event. The mean depth of the shower maximum, L, is represented by:

$$L(\mathrm{cm}/X_0) \quad = \quad (p_0 + p_1 \times \ln(E(\mathrm{GeV}))) \times \cos\theta \ , \tag{5.4}$$

where X_0 is the radiation length of the CsI (1.85 cm), E is the incident energy of photons, θ is its incident angle, $p_0 = 6.49$ and $p_1 = 0.99$. This formula was used to correct incident positions of photons based on the energy-weighted mean. The mean free path of photons, $\frac{9}{7}X_0$, was also taking into account.

2. Decide the true shape parameters based on the depth.

3. Smear the determined parameters with an expected precision for the energy deposit in each crystal. The precisions of the obtained shape parameters, σ_0 and a, for various energy ranges were estimated from the beam test data. Figure 5.14 shows the correlation between the energy deposit and the relative value of the shape parameter, σ_0, in one crystal. The width of the obtained distribution of the shape parameter for each energy range was used as the expected precision. Figure 5.15 shows the estimated precision for each shape parameter as a function of energy.

4. For the backward π^0 background, do the same as signal except for replacing the depth, d cm, with $50 - d$ cm.

5. Calculate the mean depth of the shower maximum with Equation 5.4, and estimate the shape parameters assuming that the two photons came from upstream.

6. Compare the estimated parameters with the smeared parameters.

We used the mean dependence of the shape parameters of about 1000 crystals. They were 2.2 % and 10 % per 50 cm for σ_0 and a, respectively.

We first checked the χ^2 method to discriminate the incident direction of photons. The χ^2 is defined as:

$$\chi^2 \quad = \quad \sum_{i=0,1}^{\gamma} \sum_{j}^{\mathrm{ch.}} \sum_{k=0,1}^{\mathrm{par.}} \left(\frac{s_{ijk}^{\mathrm{obs.}} - s_{ijk}^{\mathrm{exp.}}}{\sigma_k(e_{ij})} \right)^2 \ , \tag{5.5}$$

where i is an index of two photons, k is an index of shape parameters, e_{ij} is the energy deposit of the i-th photon in the j-th channel, $s_{ijk}^{\mathrm{obs.(exp.)}}$ is the observed(expected) shape parameter of the j-th channel, and σ_k is the estimated precision of the shape parameter, s_{ijk}. Figure 5.16 shows the reduced χ^2 distributions of the signal and background events. The signal to background ratio, S/N, was improved by a factor of 2.3 with a 90 % efficiency for signal.

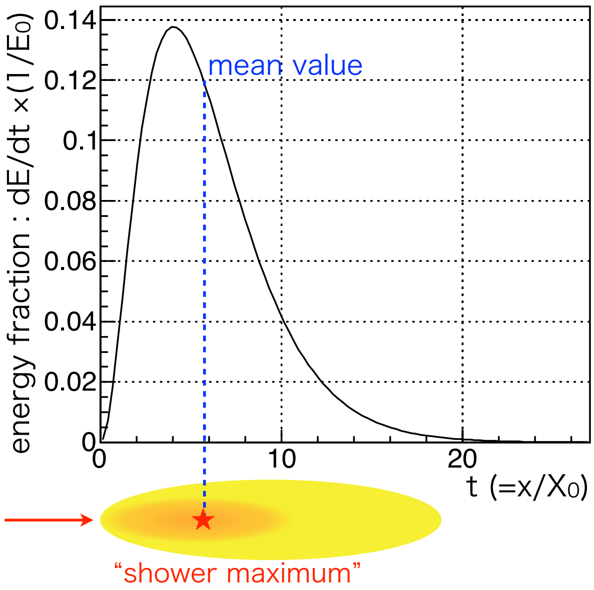

Figure 5.13: A schematic view of the "shower maximum". The black line shows the fraction of energy deposit along the direction of photons as a function of the distance from the incident position. The "shower maximum" is defined as the energy-weighted mean position along the direction of the incident photons.

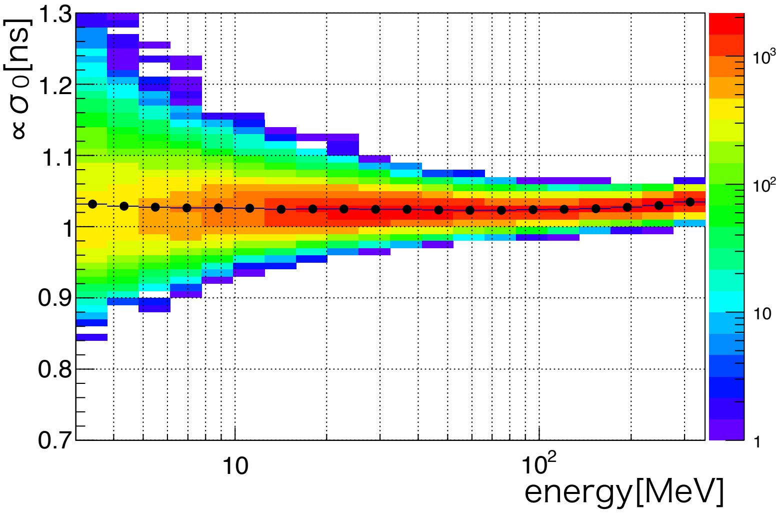

Figure 5.14: The correlation between the energy deposit and the relative value of the shape parameter, σ_0, in one crystal from the beam test data. The black dot shows the mean value of each energy range. The expected precision for different energy ranges was estimated by the width of the distribution of the shape parameter for each energy range.

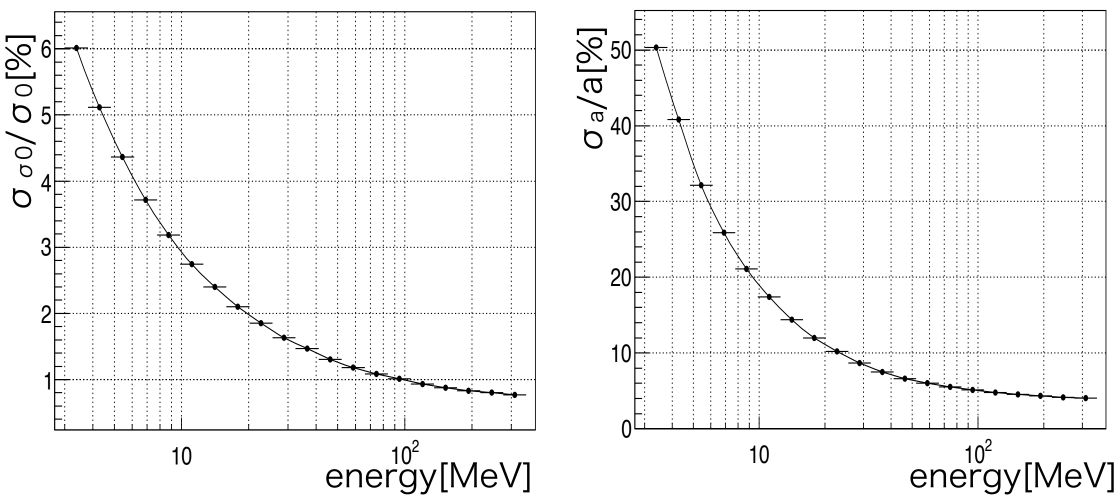

Figure 5.15: The estimated precision of the obtained shape parameters as a function of energy: Left) typical width and Right) asymmetry parameter.

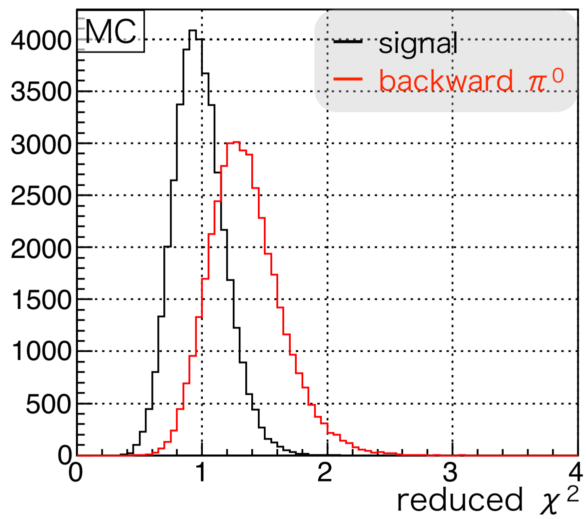

Figure 5.16: The distributions of the reduced χ^2 of the shape parameters. The black(red) histogram shows the signal(backward π^0 background).

We also checked the likelihood ratio method to discriminate the incident direction. If we know well about the pulse shape of photons that came from downstream, we can compare the likelihoods for the assumptions that the photon came from upstream and downstream. The likelihood of the n-th assumption is:

$$L_n = \prod_{i=0,1}^{\gamma} \prod_{j}^{\text{ch.}} \prod_{k=0,1}^{\text{par.}} \text{Gaussian}(s_{ijk}^{\text{obs.}} | s_{ijkn}^{\text{exp.}}, \ \sigma_k(e_{ij})) \ , \tag{5.6}$$

where $s_{ijkn}^{\text{exp.}}$ is the estimated shape parameter with the n-th assumption. Figure 5.17 shows the likelihood ratio distributions of the signal and background events. The signal to background ratio, S/N, was improved by a factor of 660 with a 90 % efficiency for signal. This rejection power is still underestimated. Although we used the mean values of the position dependence of the shape parameters, actually the position dependence of the shape parameters are different between the crystals. If there is one crystal in all the activities which can tell the direction clearly, we can distinguish background events even if all other crystals have no position dependence. We checked the rejection power also with the dependences shown in Fig. 5.12. The dependences were about two times larger than the mean values. The improvement factors of the signal to background ratio, S/N, became 1700 with the χ^2 method with a 90 % efficiency for signal, and >14000 with the likelihood ratio method with a >99 % efficiency.

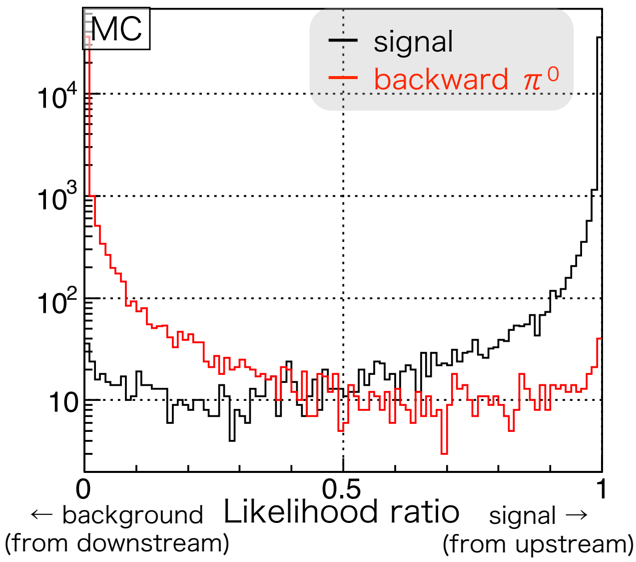

Figure 5.17: The distributions of the likelihood ratio of the shape parameters. The black(red) histogram shows the signal(backward π^0 background).

We confirmed a potential to discriminate the incident direction of photons by the pulse shapes to suppress the background events.

5.4 Double pulse separation

We also checked the case that two pulses come close in timing. We use the Bessel filter to achieve better timing and energy resolution with 125 MHz FADCs. However, the filter widens the pulse width, and it makes pulses overlap more often. If a small pulse is overlapped by a large pulse, it can be a source of inefficiency.

We evaluated this effect with waveform samples generated from the beam test data. We picked two pulses in a channel in different events and merged them into one event. The timing of one pulse was randomly shifted within 250 ns (about twice wider than a full width of a pulse). Figure 5.18 shows an example of such a merged pulse.

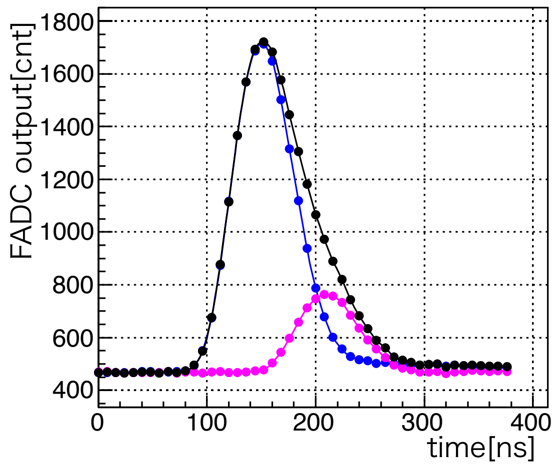

Figure 5.18: An example of merged pulses made from the beam test data. The blue and pink waveforms are from different events in a FADC channel. The black waveform shows the merged pulse.

We fitted all the sampling points of the generated pulse shapes with the templates described in Section 3.2.2, and used the χ^2 values of the fitting to identify the overlapped pulses. Figure 5.19 shows the correlation between the fitted pulse height and the reduced χ^2 of the fitting when we fit the pulse shapes of single pulses as a single pulse. If the χ^2 value of the pulse fitting is larger than a proper value, the pulse was considered as an overlapped pulse. Figure 5.20 shows an example of samples rejected by the χ^2 cut.

The inefficiency due to the overlapped pulse was estimated. Figure 5.21 shows the estimated energy distribution of a single central small crystal at the KOTO experiment. The estimated single counting rate ($E > 2$ MeV) is 20 kHz with the full intensity beam (2×10^{14} proton on target per spill). The probability of the two activities coming within 250 ns is then 5×10^{-3}. Figure 5.22 shows the estimated inefficiency[1] due to the overlapped pulse. The inefficiency due to the overlapped pulse is more than 10 times smaller than the inefficiency by other factors.

[1] We did not consider the events in which two particles come within $\pm$ 10 ns, and one pulse overlaps the other as an inefficient event. When two particles come at the same time, we cannot identify it. That is, however, not a source of inefficiency, because we can see the activity and kill the event. It corresponds to set 20 ns length timing window.

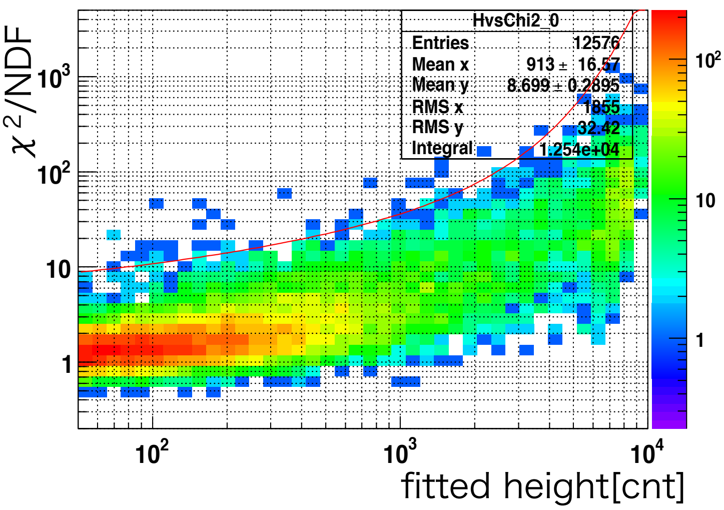

Figure 5.19: The correlation between the fitted pulse height and the reduced χ^2 of the fitting when we fit the pulse shapes of single pulses as a single pulse. The red line shows the energy dependent cut on the χ^2 value.

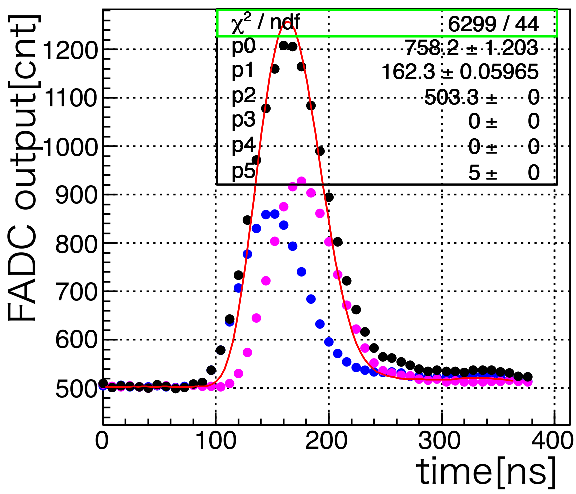

Figure 5.20: An example of the pulse shape rejected as multiple pulses. The reduced χ^2 value was 143.2 and it was much larger than the cut value, 29.2. The time difference of the original two pulses was 26 ns.

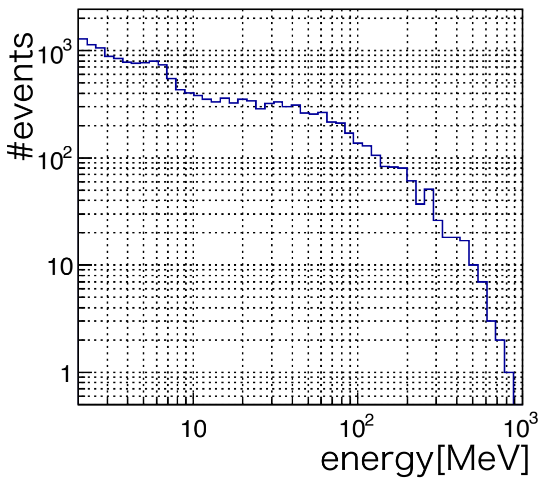

Figure 5.21: The estimated deposit energy distribution in a single channel during a spill based on a Monte-Carlo simulation.

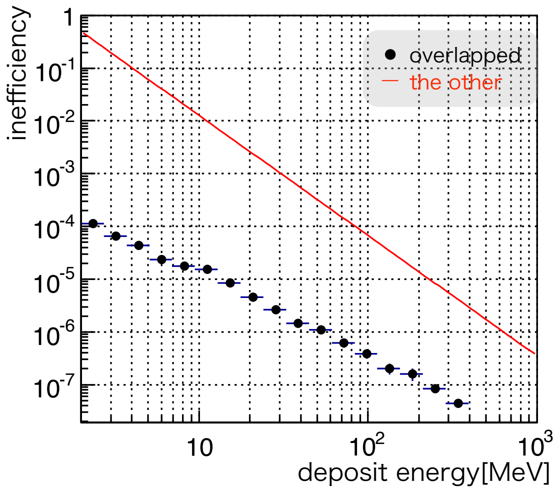

Figure 5.22: The estimated inefficiency of the calorimeter due to the overlapped pulse (black dots) and other factors (red line).

5.5 Summary of this chapter

We developed new analysis methods to fully utilize the upgraded calorimeter. One of them is to reconstruct incident positions by fitting the shower shape, and another one is to discriminate incident angles by comparing the likelihoods of the shower shapes. We also showed the potential to discriminate photons coming from downstream from photons coming from upstream by using the difference of the recorded pulse shapes. We showed that the inefficiency due to overlapped pulses was more than 10 times less than the inefficiency by other factors.

Chapter 6

Sensitivity of the KOTO experiment

Based on the performance studies of the CsI calorimeter described earlier, we will estimate the expected number of $K_L \to \pi^0 \nu \bar{\nu}$ signal and other background events, and the sensitivity of the KOTO experiment.

Section 6.1 first describes possible background sources, and Section 6.2 describes backgrounds suppressed by the incident angle discrimination explained in Section 5.2. Section 6.3 describes estimation methods for other background sources, and the estimated number of signal and background events. Section 6.4 describes the accidental loss. Finally, Section 6.5 presents the estimated experimental sensitivity of the KOTO experiment.

6.1 Background sources

We already described the background sources in Section 1.2.2. Through those mechanisms, the following processes become background sources for $K_L \to \pi^0 \nu \bar{\nu}$ decays: $K_L \to \pi^0 \pi^0$, $K_L \to \gamma\gamma$, $K_L \to \pi^- e^+ \nu$, $K_L \to \pi^+ \pi^- \pi^0$, η production at CV, and π^0 production at CV and CC02. Here, CV is the charged veto placed in front of the calorimeter, and CC02 is the photon veto counter placed at the entrance of the decay volume, as shown in Fig. 2.4. We will first describe how the new method to discriminate the incident angle can suppress some of these backgrounds.

6.2 Possible backgrounds eliminated by incident angle discrimination

As described in Section 1.3.1, backgrounds caused by halo kaons and neutrons can be suppressed by the incident angle cut. Of those backgrounds, we describe $K_L \to \gamma\gamma$ and $\eta \to \gamma\gamma$ backgrounds in the following subsections.

6.2.1 $K_L \to \gamma\gamma$ backgrounds

The $K_L \to \gamma\gamma$ decays are rejected by requiring finite transverse momentum of the two photon system. The requirement is valid for the decays of kaons in the beam core, but not for kaons in the beam halo. Because the $K_L \to \gamma\gamma$ decay has no extra photons in the final state, the decay can be a serious background source.

The momentum spectrum, the profile, and the nunber of kaons in the beam halo are not well understood, because the rate of the production of halo kaons is too small to measure or generate with Monte-Carlo simulation. We thus made the following assumptions to estimate the number of $K_L \to \gamma\gamma$ background events.

1. The momentum spectrum of kaons in the beam halo is the same as the kaons in the beam core. The halo kaons are generated by the elastic scattering of core kaons with collimators according to a Monte-Carlo study[17].

2. The profile of the kaons in the beam halo is the same as the neutrons in the beam halo.

3. The ratio of the number of kaons in the beam halo to the beam core is the same as the ratio of neutrons.

To apply the new incident angle cut on the $K_L \to \gamma\gamma$ background, the incident angle of the two photons were calculated by assuming that they came from a $K_L \to \gamma\gamma$ decay, instead of $\pi^0 \to \gamma\gamma$ decay. We can calculate the vertex position Z_{vtx} of the $K_L \to \gamma\gamma$ decay by replacing the π^0 mass with the K_L mass, and $\boldsymbol{r}_0 = (0, 0, Z_{\mathrm{vtx}})$ with $(x_{\mathrm{COE}}, y_{\mathrm{COE}}, Z_{\mathrm{vtx}})$ in Equation 1.9, where "COE" denotes the center of energy of the two photon system in the calorimeter. Figure 6.1 shows a schematic view of the reconstruction of the $K_L \to \gamma\gamma$ decay. Because the obtained value, Z_{vtx}, is a good approximated value, we corrected x_{COE} and y_{COE} to make $P_T = 0$, and calculated Z_{vtx} again with the corrected vertex position. Figure 6.2 shows the distributions of the differences between the reconstructed decay vertex position and the Monte-Carlo true value. The vertex position reconstructed with the $P_T = 0$ correction became closer to the true vertex position.

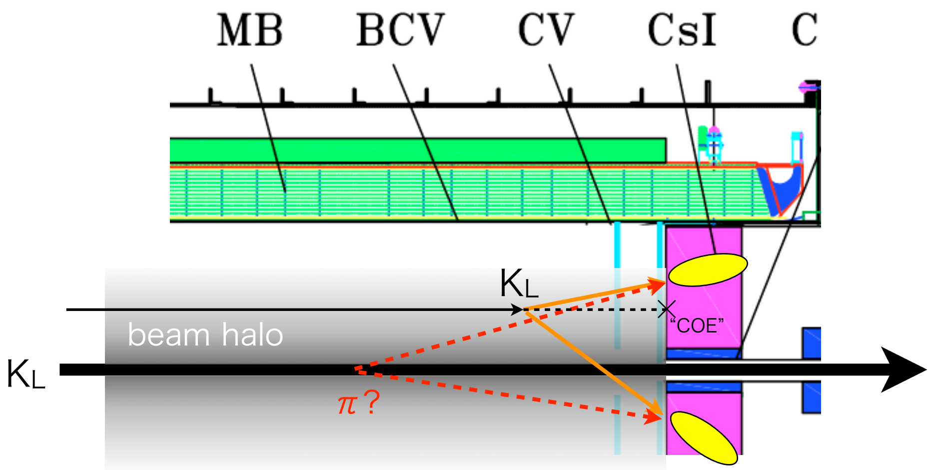

Figure 6.1: A schematic view of the $K_L \to \gamma\gamma$ decay reconstruction from two photons.

The new fitting-based position reconstruction method needs the incident angle as an input to select a proper template. Because we are now reconstructing two photons by assuming a $K_L \to \gamma\gamma$ decay, the incident angle obtained with this assumption is different from the angle for a $K_L \to \pi^0\nu\bar{\nu}$ decay. Figure 6.3 shows the distributions of the difference between the reconstructed hit position and the Monte-Carlo true value for $K_L \to \gamma\gamma$ decay in the beam halo. We updated the reconstructed vertex with the corrected hit positions to get better incident angles. We used the updated hit positions and vertexes to calculate the likelihood $L_{K_L\to\gamma\gamma}$.

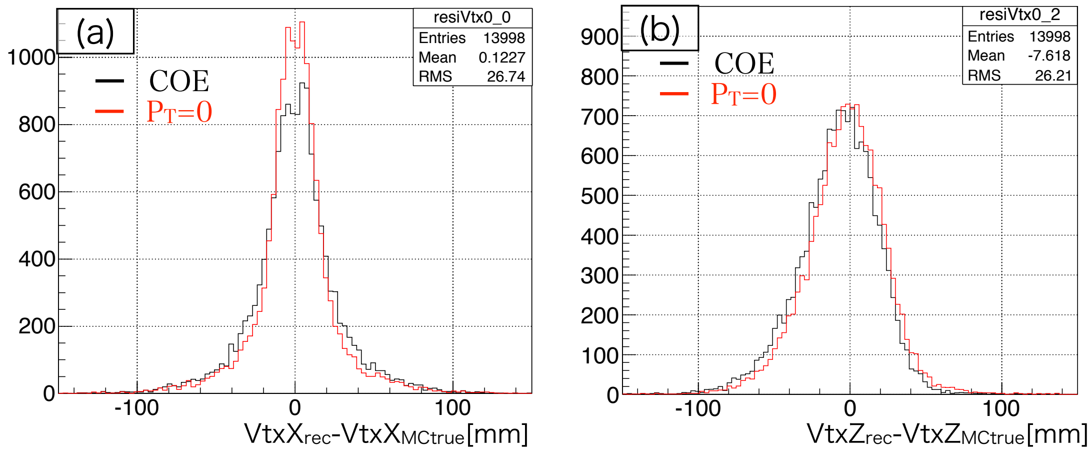

Figure 6.2: The distributions of the differences between the reconstructed decay x-vertex(a)/z-vertex(b) and the Monte-Carlo true values of the $K_L \to \gamma\gamma$ decay. The black histogram shows the distribution with the assumption that the two photons come from the center of energy of the two photon system in xy-plane. The red histogram shows the distribution with the correction that the transverse momentum of the two photon system becomes zero.

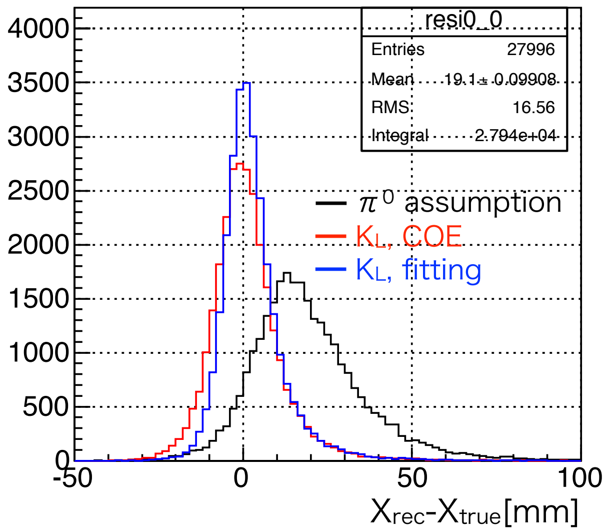

Figure 6.3: The distributions of the differences between the reconstructed incident x-position and the Monte-Carlo true value for $K_L \to \gamma\gamma$ decay in the beam halo. The black histogram was obtained with the $K_L \to \pi^0\nu\bar{\nu}$ decay assumption. The red(blue) histogram was obtained with the $K_L \to \gamma\gamma$ decay assumption with COE(fitting) based method to reconstruct incident position. The positive sign was chosen to be in the direction of photons.

Figure 6.4 shows the correlation between the reconstructed z-vertex and the transverse momentum, P_T, of the assumed π^0 for both $K_L \to \pi^0\nu\bar{\nu}$ and $K_L \to \gamma\gamma$ events after applying all the cuts except the new likelihood ratio cut. Figure 6.5 shows the likelihood ratio distribution of these events. By applying the new incident angle cut, the number of halo $K_L \to \gamma\gamma$ background events was reduced by a factor of 53 with an 83 % efficiency for the $K_L \to \pi^0\nu\bar{\nu}$ decay.

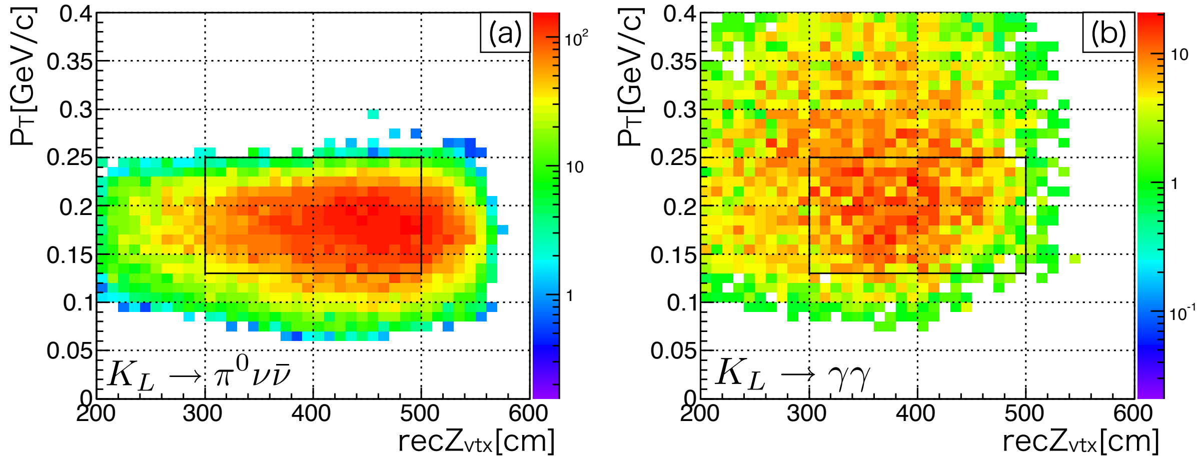

Figure 6.4: The correlation between the reconstructed z-vertex and the transverse momentum, P_T, of the assumed π^0 for $K_L \to \pi^0\nu\bar{\nu}$ (a) and $K_L \to \gamma\gamma$ (b). All the cuts except the new incident angle cut were applied. The black square in each plot shows a signal box.

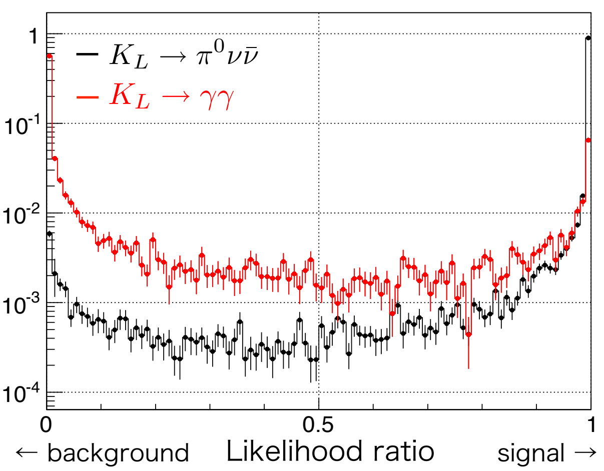

Figure 6.5: The likelihood ratio distribution for $K_L \to \pi^0\nu\bar{\nu}$ (black) and $K_L \to \gamma\gamma$ (red). The areas of the histograms were normalized to 1.

6.2.2 $\eta \to \gamma\gamma$ at CV backgrounds

The $\eta \to \gamma\gamma$ background has a similar event topology with the $K_L \to \gamma\gamma$ background. The η is produced by the interaction between the neutrons in the beam halo and the Charged Veto (CV) placed 25 cm upstream of the surface of the calorimeter. Because the decay vertex is not on the z-axis and the mass is not the π^0 mass, the incident angles of photons are different from the reconstructed incident angles with the signal assumption. The incident angle cut is thus effective for the $\eta \to \gamma\gamma$ background.

However, sometimes neutrons also produce extra π^0s or protons together with the η. When those additional activities hit near the photons from the η and generate fused clusters, the fused cluster shapes become different from a single photon cluster. Because the PDF of energy fraction was prepared for single photons, the likelihood of the fused cluster shape is extremely small, sometimes zero. If the cluster shape is different from both the signal and the background ($L_{\text{signal}} \sim L_{\text{background}} \sim 0$), we cannot calculate the likelihood ratio with Equation 5.3. The signal likelihood (Equation 5.2) can be turned into:

$$\begin{aligned} L_{\text{signal}} &= \prod_{i;\gamma} \prod_{j;x,y} \prod_{k;\text{row}} P(e_k|E_i, d_k, \theta_i^{\text{signal}}, \phi_i^{\text{signal}}) \\ &= \prod_{i;\gamma} \prod_{j;x,y} L_{ij}^{\text{signal}} \, , \end{aligned} \tag{6.1}$$

where i is an index of the reconstructed two photons, j is an index of the dimensions, x/y, and L_{ij}^{signal} is the partial signal likelihood of the i-th photon in the j-th plane. We then applied a threshold on the partial signal likelihoods, L_{ij}^{signal}, for each photon on each x/y axis. Figure 6.6 shows the correlation between photon energy and the partial signal likelihood of the photons on the x/y axis for $K_L \to \pi^0\nu\bar{\nu}$ signal and $\eta \to \gamma\gamma$ background events. We applied the threshold as a function of the photon energy for the partial signal likelihood values.

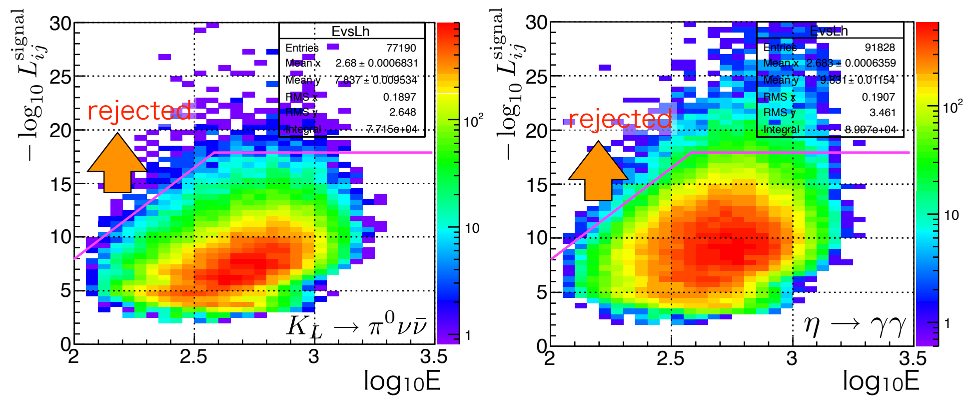

Figure 6.6: The correlation between energy and the partial signal likelihood, L_{ij}^{signal} in Equation 6.1, of photons on the x/y axis for $K_L \to \pi^0\nu\bar{\nu}$ signal and $\eta \to \gamma\gamma$ background events.

Now we can define the likelihood ratio for $\eta \to \gamma\gamma$ events. Because the K_L mass is close to the η mass and the transverse momentum of η is small but not zero, the cut to suppress the $K_L \to \gamma\gamma$ background is also effective for the $\eta \to \gamma\gamma$ background. We thus decided to apply only the cut with $K_L \to \gamma\gamma$ assumption. The rejection power of the cut was 8.7 for the $\eta \to \gamma\gamma$ background.

6.3 Other backgrounds

We also estimated the number of background events for other sources in three ways. Due to the limitation of the Monte-Carlo statistics, some backgrounds were estimated (partially) using a so-called fast simulation. (In contrast, we call the ordinal detector simulation with full shower generation as a full simulation.)

The fast simulation uses the detector response function for each detector. Each response function has been studied for individual detector. For example, in the case of veto counters, the inefficiency for various particles, energies and angles has been evaluated in advance as shown in Fig. 6.7. In the fast simulation, we use the inefficiency values as weights for events. For the calorimeter, we updated its response functions based on the performance studied in this thesis. Figure 6.8 shows the comparison between the full and fast simulations for energy and position on the calorimeter.

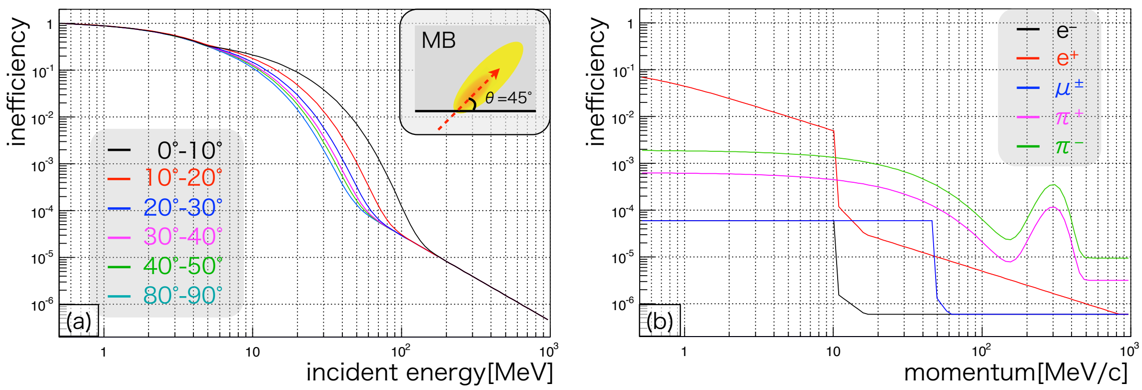

Figure 6.7: Examples of the response functions of veto detectors, commonly used in the KOTO collaboration: a) The detection inefficiency of MB for photons for various incident angles as a function of the incident energy, and b) The detection inefficiency of CV for charged particles as a function of the incident momentum.

The backgrounds sensitive to the shower shape in the calorimeter but have some extra activities in the veto counters were estimated with a full shower simulation for calorimeter and a fast simulation for the veto counters. The backgrounds not sensitive to the shower shape, but required to have large statistics were estimated with a fast simulation for all the detectors. For such backgrounds, we assumed the same efficiency, 83 %, for the new incident angle cut. The other backgrounds were estimated with a full simulation. Table 6.1 shows the summary of the background estimation methods.

The $K_L \to \pi^+\pi^-\pi^0$ decay becomes a background when two photons from the π^0 are detected by the calorimeter and the remaining two charged pions are not detected. Because the observed two photons in the calorimeter are truly from a single π^0 decayed in the beam core, the observed shower shape with the calorimeter is consistent with our assumption as a signal. This kind of events thus are not sensitive to the new incident angle cut. We estimated the number of the background events with a fast simulation for all the detectors (method 3 in Table 6.1).

The $K_L \to \pi^- e^+ \nu$ decay becomes a background when the charge exchange ($\pi^- p \to \pi^0 n$) and the annihilation of the positron ($e^+e^- \to \gamma\gamma$) occur in CV at the same time. There are four

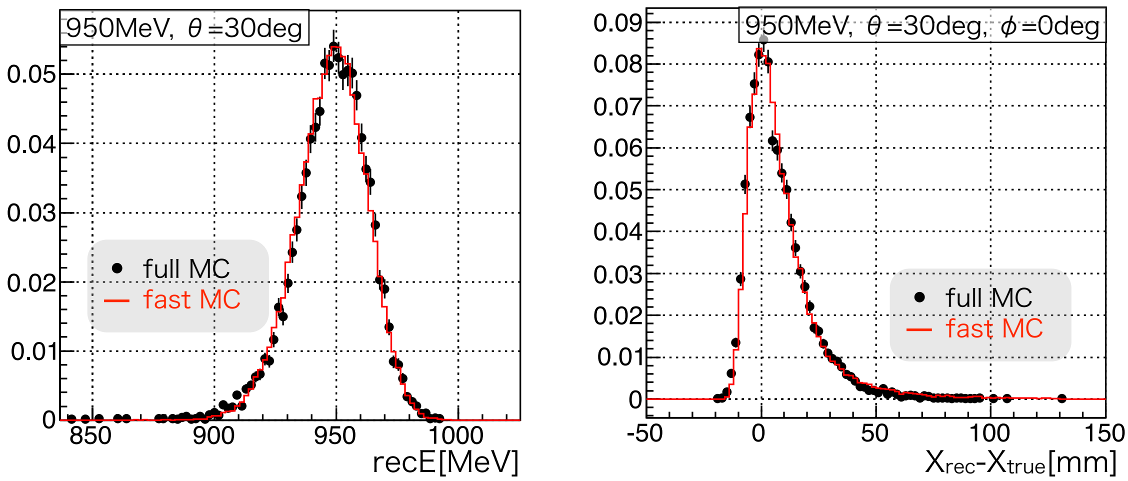

Figure 6.8: The distributions of reconstructed energy (left) and difference between the reconstructed/smeared position and Monte-Carlo true value (right). The black dots show the result obtained with the full simulation, and the red histogram shows the result obtained with the response function of the calorimeter in the fast simulation.

Table 6.1: The background estimation methods. Due to the limitation of the Monte-Carlo statistics, the number of background events were estimated in the following three ways. A full simulation means the ordinal detector simulation with full shower generation, and a fast simulation is based on the detector response function evaluated in advance.

#	calorimeter	veto counters	backgrounds
1	full	full	not so rare
2	full	fast	rare, sensitive to the shower shape cut
3	fast	fast	very rare, not sensitive to the shower shape cut

Table 6.2: The expected number of signal and background events in the KOTO experiment. The numbers in the table are normalized to 1.85×10^{14} K_Ls at the exit of beam line assuming 2×10^{14} protons on target per spill and 12 month long beam time. The method column indicates the Monte-Carlo simulation procedure shown in Table 6.1 : 1=full , 2=calorimeter:full+veto:fast, and 3=fast. The numbers with parentheses were obtained by assuming the same efficiency as signal for the incident angle cut.

sources	method	w/o new cut	w/ new cut
$K_L \to \pi^0\nu\bar{\nu}$	1	7.85 ± 0.06	6.50 ± 0.05
$K_L \to \pi^0\pi^0$(except fusion)	3	3.40 ± 0.09	(2.81 ± 0.08)
$K_L \to \pi^0\pi^0$(fusion)	2	2.15 ± 0.15	0.75 ± 0.09
$K_L \to \gamma\gamma$(halo)	1	101 ± 2	1.90 ± 0.28
$K_L \to \pi^+\pi^-\pi^0$	3	0.54 ± 0.18	(0.45 ± 0.15)
$K_L \to \pi^-e^+\nu$	2	0.86 ± 0.08	0.22 ± 0.04
$\eta \to \gamma\gamma$(@CV)	1	0.37 ± 0.02	0.04 ± 0.01
$\pi^0 \to \gamma\gamma$(@CV)	1	0.36 ± 0.15	0.06 ± 0.06
$\pi^0 \to \gamma\gamma$(@CC02)	1	0.13 ± 0.04	0.08 ± 0.03
BG total	-	109 ± 2	6.32 ± 0.35

photons in the final state. Some of them hit on MB, or hit close to each other in the calorimeter and make a fused cluster, because of the short distance between CV and the calorimeter. The background is thus sensitive to the shower shape, and has some activity in the veto counters. We estimated the number of the background events with the combined method (method 2 in Table 6.1),

The $K_L \to \pi^0\pi^0$ decay becomes a background when two extra photons are not detected. This background can be classified into two groups. The first one is to miss both two photons by detection inefficiency, and the other is related to the fused cluster. In the first group, the events remaining after applying the kinematic cuts, are the events in which two photons from a π^0 detected in the calorimeter and two photons from the other π^0 are missed, according to a Monte-Carlo study. Because the shower shape observed in the calorimeter is consistent with our assumption as a signal, we estimated the number of the background events with a fast simulation for all the detectors (method 3 in Table 6.1). For the second group, they were estimated by the combined method (method 2 in Table 6.1), because they make a fused cluster and are sensitive to the shower shape cut.

In addition to the $K_L \to \gamma\gamma$ and $\eta \to \gamma\gamma$ at CV backgrounds, the number of background events for π^0 production at CC02 and CV were estimated by a full simulation (method 1 in Table 6.1).

Table 6.2 shows the summary of the expected number of signal and background events in the KOTO experiment. By applying the incident angle cut, the $K_L \to \gamma\gamma$ background is suppressed in particular. The signal to background ratio, S/N, then increased from 0.07 to 1.03, and improved by a factor of 14.

6.4 Accidental loss

We also estimated the accidental loss due to the particles in the beam and daughter particles from another K_L decays inside the veto time window. The accidental loss was estimated based on the expected single counting rate for each detector. The estimated loss probability due to the accidental activities was 0.34, and the expected number of signal and background events became 4.29 ± 0.04 and 4.17 ± 0.23, respectively.

6.5 Expected sensitivity

In rare decay experiments, we often use a parameter called "Single Event Sensitivity (SES)" as a reference of the experimental sensitivity. The expected number of the observed events, N_{obs}, is represented with the SES as:

$$N_{\mathrm{obs}} = \frac{Br(K_L \to \pi^0 \nu\bar{\nu})}{\mathrm{SES}} . \tag{6.2}$$

Here, SES is expressed as:

$$\begin{aligned} \mathrm{SES} &= \frac{1}{N_{\mathrm{decay}} \times A_{\mathrm{signal}}} \\ &= \frac{1}{N_{K_L} \times P_{\mathrm{decay}} \times A_{\mathrm{signal}}} , \end{aligned} \tag{6.3}$$

where N_{decay} is the number of K_L decays, A_{signal} is the acceptance of the $K_L \to \pi^0 \nu\bar{\nu}$ signal, N_{K_L} is the number of K_L, and P_{decay} is the decay probability in the fiducial region ($3000 < Z_{\mathrm{VTX}}(\mathrm{mm}) < 5000$, where the upstream surface of the CsI calorimeter is at $Z = 6148$ mm). The number of K_L is expected to be 1.85×10^{14} by assuming 2×10^{14} protons on target per spill and 12 months of beam time, the decay probability in the fiducial region is estimated to be 3.47×10^{-2}, and the number of K_L decays is thus 6.42×10^{12}. The acceptance of the $K_L \to \pi^0 \nu\bar{\nu}$ signal is 2.78×10^{-2} in this analysis. Substituting these numbers in Equation 6.3, we obtained

$$\mathrm{SES} = 5.59 \times 10^{-12} . \tag{6.4}$$

We estimated the number of observed events to be 8.46 consisting of 4.29 signal and 4.17 background events. There are several scenarios depending on the result of the KOTO experiment. In the following calculations, we assumed the background estimation is correct, and systematic errors and Monte-Carlo statistics are not taken into account.

- When we observe more than 11 events, we can say that we observed at least one $K_L \to \pi^0 \nu\bar{\nu}$ decay with a 3σ evidence, because the probability of the observation of 12 or more background events with the expectation of 4.17 background events is 0.13 % by Poisson distribution, and smaller than 0.27 %.

- When we observe more than 18 events, we can say that we found a New Physics which enhances the $K_L \to \pi^0 \nu\bar{\nu}$ decay with a 3σ evidence, because the probability of the observation of 19 or more events with the expectation of 8.46 events in total is 0.12 %.

- When we observe only 4 events, we can set an upper limit on the branching ratio: $Br(K_L \to \pi^0 \nu\bar{\nu}) < 4.47 \times 10^{-11}$ (90 % C.L.), assuming that all the 4 events are $K_L \to \pi^0 \nu\bar{\nu}$ decays.

If we take the expected number of background events into account by the Feldman-Cousins method[18], the upper limit becomes 2.48×10^{-11}(90 % C.L.). The upper limit is almost the same as the Standard Model prediction. We can thus exclude most of the allowed region in theories which give the branching ratio above the Standard Model prediction.

- When we observe less than 2 events, we can say that we find a New Physics which suppresses the $K_L \to \pi^0 \nu \bar{\nu}$ decay with a 3σ evidence, because the probability of the observation of 1 or less events with the expectation of 8.46 events in total is 0.20 %.

In these ways, the result of the KOTO experiment has a potential to test the Standard Model, and acts an important role to search for a New Physics.

Chapter 7

Discussion

We will discuss the possible improvements on the timing resolution and the experimental sensitivity, and the uncertainty on evaluating the number of $K_L \to \gamma\gamma$ background events in the following sections.

7.1 Further improvement of the timing resolution

We defined the timing of each crystal by the peak timing of the fitted pulse shape. We tested another way, "Constant fraction method"(CFM), to define the timing. Figure 7.1 shows a schematic view of this method. The timing was defined by the constant fraction (0.5) of the peak pulse height on the rising edge of the pulse shape. The concrete procedure is the following. First, fit the pulse shape and obtain the peak timing. Next, fit a linear function to the pulse shape in the range : $t_{\text{peak}} - 42$ ns $< t < t_{\text{peak}} - 18$ ns. Evaluate the timing with the linear function that has a half of the peak pulse height.

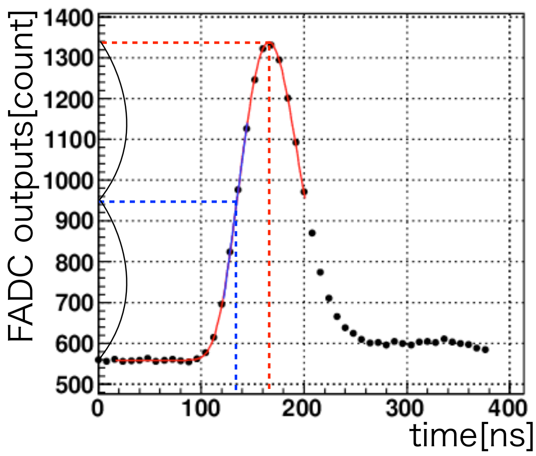

Figure 7.1: A schematic view of the constant fraction method. The black dots show the recorded pulse shape, the red line shows the template based fitted function, and the blue line shows the linear function to define the timing based on the constant fraction method. The red(blue) dashed lines show the pulse height and the timing at the peak(constant fraction).

We evaluated the timing resolution obtained with CFM with data from the beam test, and also with the pulse shape simulation described in Chapter 4. Figure 7.2 shows the timing resolution obtained with CFM for various energy ranges. For energies more than a few MeV, the CFM gives a better timing resolution than pulse peak timing method, both in data and the pulse shape simulation.

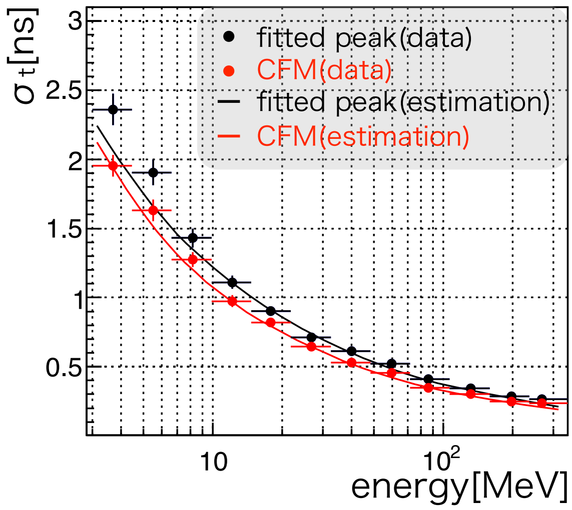

Figure 7.2: The timing resolution of various methods as a function of deposit energy. The black(red) dots show the timing resolution obtained with data with fitted peak timing(CFM). The black(red) line shows the timing resolution obtained with the pulse shape simulation with fitted peak timing(CFM).

The CFM, however, has a problem with smaller pulses below a few MeV; the timing resolution becomes larger, and moreover sometimes the timing cannot be defined because of the ground noise, as shown in Fig. 7.3.

The calorimeter works not only as a calorimeter but also as a veto counter, and the threshold will be a few MeV. If the timing for such a few MeV photons are not reconstructed within a reasonable timing range, that may be a possible source of inefficiency. Because of this reason, we used the timing based on the fitted peak timing in this thesis.

7.2 Further improvement on the sensitivity

According to the background estimation summarized in Table 6.2 , $K_L \to \pi^0\pi^0$ decay and $K_L \to \gamma\gamma$ decay are the two largest background sources for the KOTO experiment. The $K_L \to \pi^0\pi^0$ background events are caused by the detection inefficiency, mostly in Main Barrel (MB). As described in Section 2.2.3, we plan to add 5 X_0 thick modules inside the existing MB. The upgrade design is now being optimized. Because of the optimization, the number of $K_L \to \pi^0\pi^0$ background is estimated to be a half of the current estimation. If the $K_L \to \pi^0\pi^0$ background is suppressed by a factor of 2, the $K_L \to \gamma\gamma$ background then becomes the largest. Though the $K_L \to \pi^0\pi^0$ background is suppressed by a factor of 2, the signal to background ratio, S/N, will only improve from 1.04 to 1.39 because of the amount of the $K_L \to \gamma\gamma$ background.

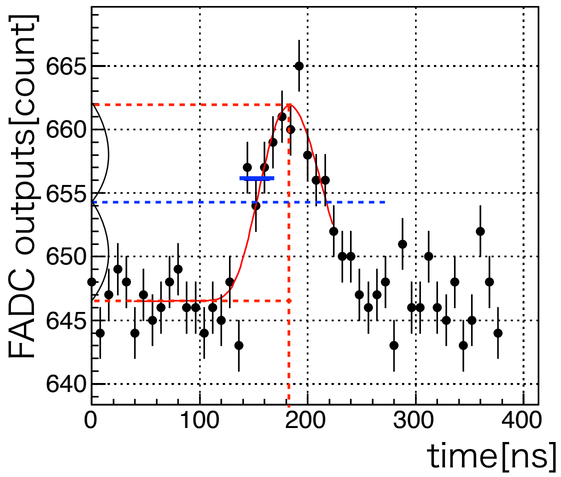

Figure 7.3: An example of the pulse shapes for which we failed to define the timing with CFM. The black dots show the recorded pulse shape, the red line shows the template based fitted function, and the blue line shows the linear function for CFM. The red dashed line shows the fitted pulse height and the fitted timing. The blue dashed line shows a half of the pulse peak height. The peak pulse height corresponds to about 1 MeV.

Figure 7.4 shows the rejection power of the new incident angle cut against the $K_L \to \gamma\gamma$ background as a function of the efficiency of the cut for the $K_L \to \pi^0\nu\bar{\nu}$ signal. By tightening the cut, we can further reduce the $K_L \to \gamma\gamma$ background. Figure 7.5 shows the estimated signal to background ratio, S/N, as a function of the efficiency of the cut for the $K_L \to \pi^0\nu\bar{\nu}$ decay. If we tighten the threshold of the cut from 83 to 75 % efficiency for the $K_L \to \pi^0\nu\bar{\nu}$ decay, the S/N ratio will be improved from 1.39 to 1.86, and the expected number of signal events is reduced from 4.29 to 3.89.

7.3 Uncertainty on evaluating the number of $K_L \to \gamma\gamma$ background events

As discussed in Chapter 6, the $K_L \to \gamma\gamma$ decay in the beam halo can be a serious background source, and it is strongly suppressed by the incident angle discrimination. We will discuss the uncertainties on the number of the background events due to the understanding of the shower shape PDF, and the rate of K_Ls in the beam halo.

7.3.1 Uncertainty of the shower shape PDF

The incident angle discrimination is based on the likelihoods of the shower shapes, and the likelihood is calculated by using the shower shape PDF. We generated the shower shape PDF with the Monte-Carlo simulation. If the Monte-Carlo based shower shape PDF does not represent the true shower shape in data, the estimated number of the halo $K_L \to \gamma\gamma$ background events is wrong. Understanding the uncertainty of the shower shape PDF is crucial to evaluate the sensitivity of the KOTO experiment. We evaluated the uncertainty by using the position resolution as a reference.

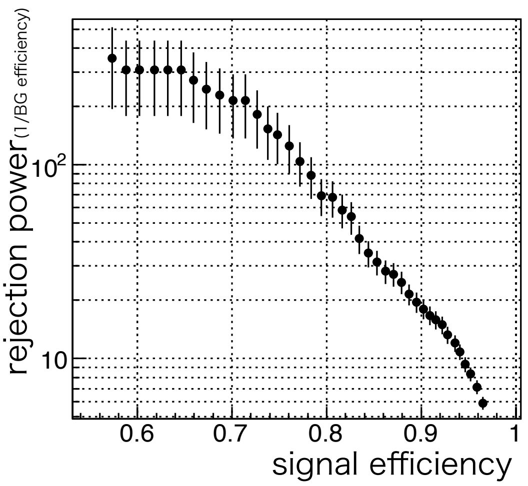

Figure 7.4: The rejection power of the new incident angle cut against the $K_L \to \gamma\gamma$ background as a function of the efficiency of the cut for the $K_L \to \pi^0\nu\bar{\nu}$ decay.

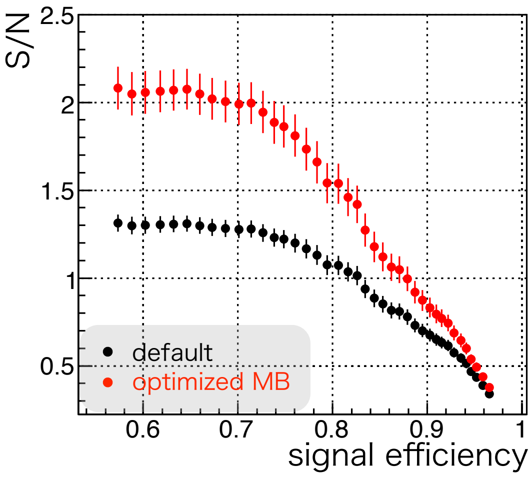

Figure 7.5: The estimated signal to background ratio, S/N, as a function of the efficiency of the cut for the $K_L \to \pi^0\nu\bar{\nu}$ decay. The black(red) dots show the result with the upgraded MB before(after) the optimization.

The Monte-Carlo based shower shapes are also used to reconstruct incident positions. We first checked whether the fitting based position reconstruction method really uses the shower shape information. We changed the crystal size and evaluated the position resolution with the fitting based method and the previous energy-weighted mean method. Figure 7.6 shows the position resolution as a function of the incident angle for different crystal sizes. With the energy-weighted mean method, the position resolutions for the incident angle of 40°[1] are almost the same and independent of the crystal sizes. With the fitting based method, the estimated position resolution is better than the energy-weighted mean method, and it becomes better with smaller size crystals. This means that the fitting based method uses the shower shape information, and the position resolution with the fitting method can reflect the difference of shower shapes. This is why we used the position resolution with the fitting based method, as a reference to evaluate the shower shape in the Monte-Carlo simulation.

Basic idea of this evaluation is the following.

1. Estimate the position resolution with Monte-Carlo simulation with the fitting based method by using templates for (A) true incident angles, and (B) wrong incident angles. We can evaluate how sensitive the obtained position resolution is to the shower shapes for different incident angles.

2. Estimate the position resolution with (C) the beam test data with the fitting based method by using templates for the true incident angle.

3. Compare the difference between (A) and (C) with the difference between (A) and (B).

[1]The position resolutions with energy-weighted mean method for smaller incident angles become larger because the crystal size becomes larger than the transverse shower shape spread.

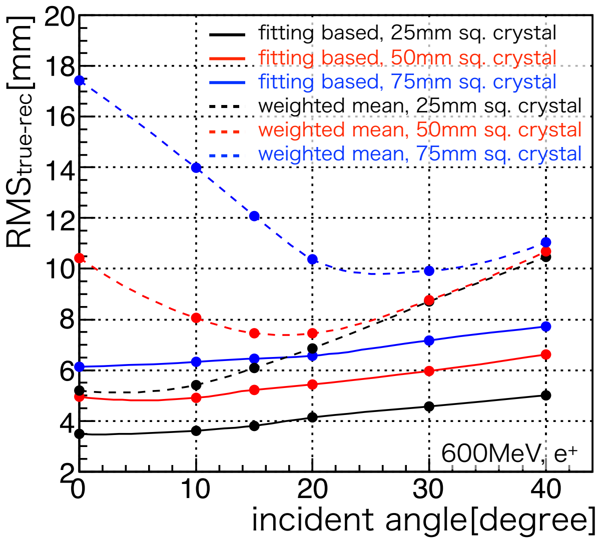

Figure 7.6: The position resolution as a function of the incident angle with the fitting method (solid lines) and the energy-weighted mean method (dashed line) for crystal sizes: 25mm(black), 50mm(red) and 75mm(blue). The RMS value of the distribution of distance between the reconstructed position and Monte-Carlo true value, was used as a position resolution in this plot.

Figure 7.7 shows the obtained position resolutions as a function of the true incident angle. The position resolution is sensitive to the shower shape templates to be used on fitting shower shape, and most of the position resolutions[2] obtained with the beam test data (C) were more consistent with the values with the templates for the true incident angles (A) than the values with the templates for the true $+2.5°$ incident angles (B). This showed that we know the true shower shapes to the precision that corresponds to $2.5°$ difference in the incident polar angle.

Figure 7.8 shows the difference of the calculated polar angles of photons between with the $K_L \to \pi^0\nu\bar{\nu}$ assumption and with the $K_L \to \gamma\gamma$ assumption. All the differences of the calculated polar angles of photons between the two assumptions are larger than $5°$ both for the $K_L \to \pi^0\nu\bar{\nu}$ signal and halo $K_L \to \gamma\gamma$ background. Though the incident angle discrimination uses not only the difference in polar angles but also uses the difference in azimuthal angles, understanding the shower shapes to the precision that corresponds to $2.5°$ difference in the incident polar angles, is good enough to discriminate the $K_L \to \pi^0\nu\bar{\nu}$ events from the $K_L \to \gamma\gamma$ events.

7.3.2 Uncertainty of the rate of halo K_Ls

We also evaluated the uncertainty of the rate of K_Ls in the beam halo. Both the $K_L \to \pi^0\nu\bar{\nu}$ signal and the halo $K_L \to \gamma\gamma$ background are coming from K_L decay, and only the ratio of the beam halo to the beam core is effective. Because we have no data to evaluate the halo/core ratio of K_Ls, we adopted the difference of the halo/core ratio of neutrons between Monte-Carlo

[2]The turntable we used at the beam test has stoppers just every $10°$. We thus excluded the position resolution for the incident angle of $15°$ on evaluation.

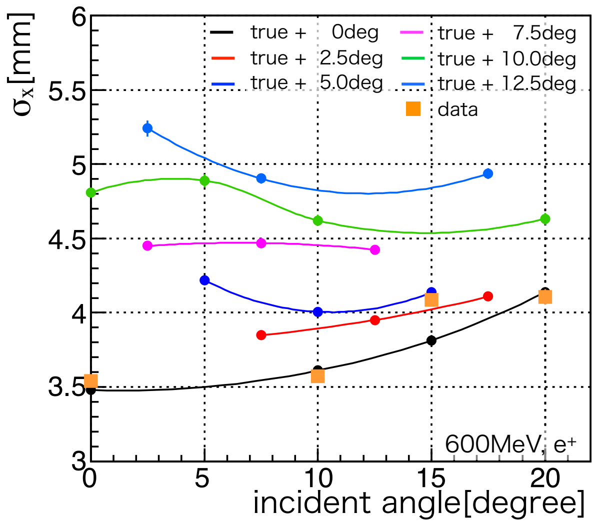

Figure 7.7: The position resolution with the fitting based method as a function of the true incident angle. The round dots show the results obtained with the templates for the true incident angles plus 0°(black), 2.5°(red), 5°(blue), 7.5°(magenta), 10°(green) and 12.5°(light-blue). The orange squares show the position resolution obtained with beam test data. The distribution of the distance between the reconstructed position and the hit position measured with scintillating fibers was fitted with Asymmetric Gaussian (Equation 3.17), and its σ_0 was used as the position resolution in this plot.

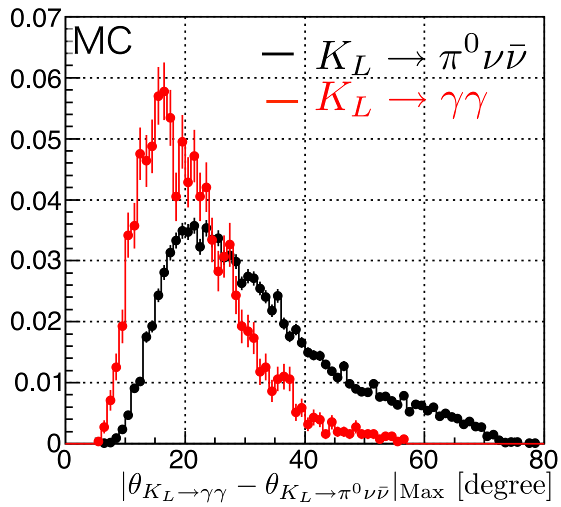

Figure 7.8: The difference of the calculated polar angles of photons between with the $K_L \to \pi^0\nu\bar{\nu}$ assumption and with the $K_L \to \gamma\gamma$ assumption, obtained with the Monte-Carlo simulation with all the cuts except for the incident angle discrimination applied. The black(red) line shows the result for the $K_L \to \pi^0\nu\bar{\nu}(K_L \to \gamma\gamma)$ decay. Of the two photons, the larger difference was filled in this plot.

packages as the uncertainty of the halo/core ratio of K_Ls. Figure 7.9 shows the neutron profiles[3] estimated with Geant3 and FLUKA[17]. If we define "halo" as the particles in $|x| > 60$ mm, the ratio of the "halo" were $(5.27 \pm 0.05) \times 10^{-4}$ for Geant3, and $(4.91 \pm 0.13) \times 10^{-4}$ for FLUKA. The difference of the "halo" ratio was 6.8 ± 2.7 % between the Monte-Carlo packages. The 7% difference of the rejection power of the incident angle discrimination toward the halo $K_L \to \gamma\gamma$ background corresponds to 0.5% difference of the signal efficiency around the cut point as was shown in Fig. 7.4, and it is negligible on calculating the sensitivity.

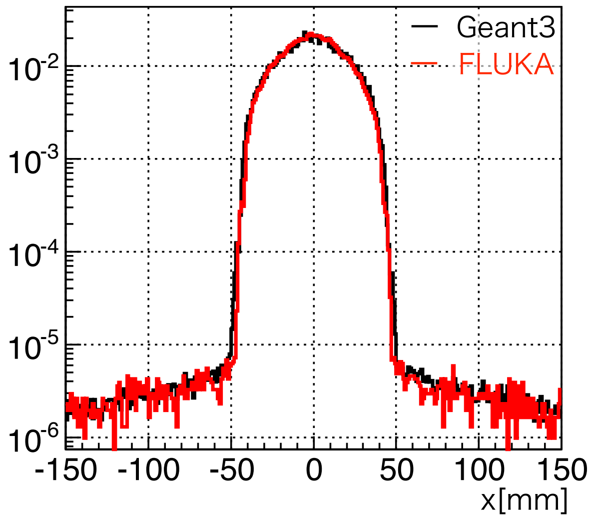

Figure 7.9: The neutron profiles in x-plane estimated with Geant3(black) and FLUKA(red)[17]. The integrals of both histograms were normalized to 1.

[3]Unlike the beam line condition for physics runs, a vacuum window was placed at 20.5 m from the target and the region downstream of the vacuum window was filled with air. The vacuum window was made of 100 μm thick SUS.

Chapter 8

Conclusion

The KOTO experiment at J-PARC is a dedicated experiment aiming to observe the $K_L \to \pi^0 \nu\bar{\nu}$ decay. We upgraded our experimental apparatus to achieve the Standard Model sensitivity. In those upgrades, we mainly described a study about the upgrades of the CsI calorimeter. The major upgrades of the calorimeter are improvement of granularity, and waveform readout.

We did a beam test to evaluate the basic performance of the upgraded calorimeter, and studied the origin of the energy and timing resolutions obtained with waveform readout. We developed new analysis methods to fully utilize the fine granularity. One of them is to reconstruct incident positions by fitting the shower shape, and another one is to discriminate incident angles by comparing the likelihoods of the shower shape to suppress halo $K_L \to \gamma\gamma$ background. Because the $K_L \to \gamma\gamma$ decay has no extra photons in the final state, the decay in the beam halo can be a serious background source and only rejected by the calorimeter. With the incident angle discrimination, the halo $K_L \to \gamma\gamma$ background was suppressed by a factor of 53 with an 83 % efficiency for the $K_L \to \pi^0 \nu\bar{\nu}$ decay. We also showed a potential to discriminate the incident direction of photons by using the recorded waveform.

Based on the performance studies of the CsI calorimeter, we estimated the number of signal and background events, and evaluated the sensitivity of the KOTO experiment. The single event sensitivity was estimated at 5.6×10^{-12}. With the upgraded calorimeter, we can suppress backgrounds and achieve the sensitivity of the Standard Model prediction.

Appendix A

Functions for pulse shape fitting

We decided to use templates to fit pulse shapes at the end, but we have tested several functions to fit pulse shapes. One of the functions was Asymmetric Gaussian with a higher order (Equation 3.1). We also fitted the pulse shapes with Crystal Ball function. Because pulse shapes have longer tail in positive direction in timing, we modified the function to:

$$\frac{A(t)}{|A|} = \left\{ \begin{array}{ll} \mathrm{Gaussian}(t, \mu, \sigma) & (\frac{t-\mu}{\sigma} \leqslant \alpha) \\ \left(\frac{n}{|\alpha|}\right)^n \exp\left(-\frac{\alpha^2}{2}\right)\left(\frac{n}{|\alpha|} - |\alpha| + \frac{t-\mu}{\sigma}\right)^{-n} & (\frac{t-\mu}{\sigma} > \alpha) \end{array} \right\} . \tag{A.1}$$

We also tested a function which is sometimes used to fit pulse shapes of plastic scintillators:

$$A(t) = 2|A| \times \mathrm{Freq}\left(\frac{t-\mu}{\tau_L}\right) \exp\left(-\frac{t-\mu}{\tau_R}\right) , \tag{A.2}$$

where $\mathrm{Freq}(x)$ is the normal frequency function:

$$\mathrm{Freq}(x) = \frac{1}{\sqrt{2\pi}} \int_{-\infty}^{x} \exp\left(-\frac{t^2}{2}\right) dt . \tag{A.3}$$

Another kind of asymmetric gaussian was also tested to fit pulse shapes:

$$\frac{A(t)}{|A|} = \left\{ \begin{array}{ll} \mathrm{Gaussian}(t, \mu, \sigma_L) & (t \leqslant \mu) \\ \mathrm{Gaussian}(t, \mu, \sigma_R) & (t > \mu) \end{array} \right\} . \tag{A.4}$$

Figure A.1 shows the mean value of the reduced χ^2 of the fitting with these functions as a function of the fitted pulse height. Asymmetric Gaussian well reproduces the pulse shapes[1] except for pulse heights larger than 4000 FADC counts because of the pulse shape deformation by the non-linearity.

The fitted pulse height dependence of the reduced χ^2 is explained as following. The definition of the χ^2 of the fitting is:

$$\chi^2 = \sum_{n}^{\mathrm{smpl}} \left(\frac{h(t_n) - h_n}{\sigma_n}\right)^2 , \tag{A.5}$$

[1] We did not include the tail part of pulse shapes on fitting. We just fitted pulse shapes between -150 ns and 45 ns relative to the roughly decided peak timing as described in Section 3.2.2.

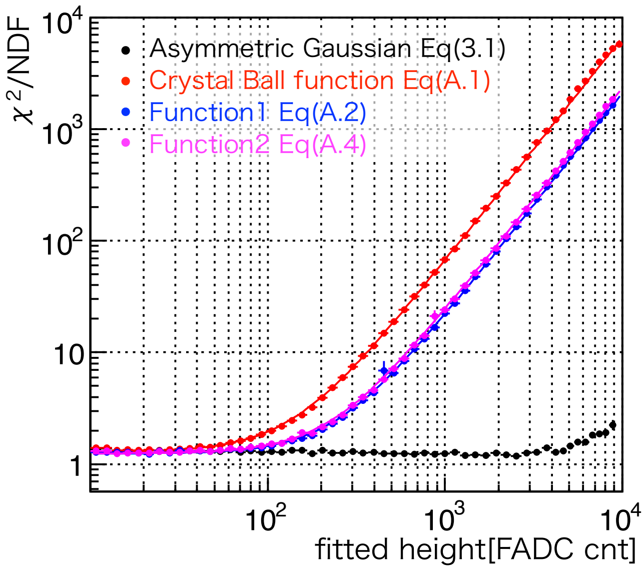

Figure A.1: The reduced χ^2 of the fitting is shown as a function of the fitted pulse height. The dots show the result obtained with Asymmetric Gaussian (black), Crystal Ball function (red), Equation A.2 (blue) and Equation A.4 (magenta), respectively. The height dependences obtained with those functions except Asymmetric Gaussian were parameterized with the function (Equation A.6), and the solid lines show the fitted functions.

where n is an index of sampling point, $h(t)$ is the function to fit the pulse shape, and t_n, h_n and σ_n are the timing, height and error of the n-th sampling point, respectively. If the function cannot represent recorded pulse shapes correctly, the difference, $h(t_n) - h_n$, for each sampling point is proportional to the pulse height because we set an error of each sampling point at the independent value of the pulse height, the amount of ground noise. We can thus parameterize the dependence with the function:

$$\chi^2 = (ah)^2 + b^2 \ . \tag{A.6}$$

The fitted height dependences of the reduced χ^2 except for Asymmetric Gaussian were fitted with Equation A.6 as is shown in Fig. A.1.

On fitting pulse shapes, we required that the shape to be used for fitting should be fixed, as described in Section 3.2.2. Figure A.2 shows the mean value of the reduced χ^2 of the fitting with Asymmetric Gaussian and templates as a function of the fitted pulse height. Parameters of Asymmetric Gaussian except for the pulse height and peak timing were fixed on fitting. Even with Asymmetric Gaussian, the reduced χ^2 became larger than the one obtained with templates, when we fixed shape parameters on fitting. We thus decided to use the templates to fit pulse shapes at the end.

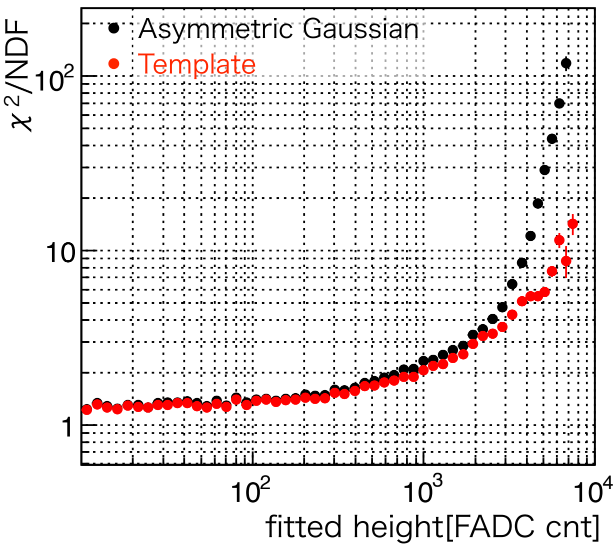

Figure A.2: The reduced χ^2 of the fitting is shown as a function of the fitted pulse height. The black(red) dots show the reduced χ^2 obtained with Asymmetric Gaussian (templates). Parameters of the Asymmetric Gaussian except for the pulse height and timing were fixed on fitting.

Bibliography

[1] S. M. Barr, G. Segre and H. A. Weldon, Phys. Rev. D **20**, 2494 (1979).

[2] L. Wolfenstein, Phys. Rev. Lett. **51**, 1945 (1983).

[3] A. J. Buras, F. Schwab and S. Uhlig, hep-ph/0405132.

[4] T. Inami and C. S. Lim, Prog. Theor. Phys. **65**, 297 (1981).

[5] A. J. Buras, F. Schwab, and S. Uhlig, (2004), hep-ph/0405132.

[6] J. Brod, M. Gorbahn, and E. Stamou, Phys. Rev. D **83**, 034030 (2011).

[7] A. J. Buras, T. Ewerth, S. Jager, and J. Rosiek, Nucl. Phys. B **714**, 103 (2005), hep-ph/0408142.

[8] G. D'Ambrosio, G. F. Giudice, G. Isidori, and A. Strumia, Nucl. Phys. B **645**, 155 (2002), hep-ph/0207036.

[9] U. Haisch, A. Weiler, Phys. Rev. D **76**, 074027 (2007), hep-ph/0706.2054.

[10] E391a, J. K. Ahn *et al.*, Phys. Rev. D **81**, 072004 (2010).

[11] H. Morii, *Experimental Study of the Decay* $K_L^0 \to \pi^0 \nu\bar{\nu}$, PhD thesis, Kyoto University, (2010).

[12] J-PARC E14 Collaboration, *Technical Design Report of KL Beamline at the J-PARC Hadron Hall*, (2009).

[13] K. Shiomi *et al.*, Nucl. Instrum. Meth. A **664**, 264 (2012).

[14] T. Ishikawa, Informal meeting "Hadron Physics", (2007).

[15] A private communication with M. Togawa (Osaka University, Department of Physics, 2011).

[16] KTeV, A. Alavi-Harati *et al*, Phys. Rev. D **67**, 012005 (2003).

[17] A private communication with T. Shimogawa (Saga University, Department of Physics, 2011) and K. Shiomi (Kyoto University, Department of Physics, 2011).

[18] G. J. Feldman and R. D. Cousins, Phys. Rev. D **57**, 3873 (1998).